# Investigation of fluorescence fluctuation microscopy methods to measure molecular density on substrates and characterize processes in optogenetics

Dwiria Wahyuni

# THÈSE

Pour obtenir le grade de

## DOCTEUR DE L'UNIVERSITE GRENOBLE ALPES

Spécialité : **Physique pour les sciences du vivant**

Arrêté ministériel : 25 mai 2016

Présentée par


## Dwiria Wahyuni

Thèse dirigée par **Antoine DELON, Professeur, Université Grenoble Alpes**, et
codirigée par **Irène WANG, Ingénieur de recherche, Université Grenoble Alpes**

préparée au sein du **Laboratoire Interdisciplinaire de Physique**
dans **l'École Doctorale de Physique**


# Développements de méthodes de microscopie de fluctuations de fluorescence : application aux mesures de densité de protéines sur substrats et à la caractérisation de processus d'optogénétique

# Investigation of fluorescence fluctuation microscopy methods to measure molecular density on substrates and characterize processes in optogenetics

Thèse soutenue publiquement le **9 octobre 2020**,
devant le jury composé de :

**Mme. Irina MIHALCESCU**
Professeur, Université Grenoble Alpes, Présidente du jury
**M. Cyril FAVARD**
Ingénieur de recherche, CNRS Délégation Occitanie Est, Rapporteur
**M. Rodolphe JAFFIOL**
Maitre de conférences, Université de technologie de Troyes, Rapporteur
**M. Didier Albert MARGUET**
Directeur de recherche, CNRS Délégation Provence et Corse, Examinateur
**M. Warsito**
Professeur, Universitas Lampung, Invité

# ABSTRACT

Quantitative analysis in microscopy imaging has always been a challenge. One noticeable quantitative technique is Fluorescence Fluctuation Microscopy, which is a family of analytical tools generally developed for confocal microscopes that takes advantage of the temporal and/or spatial fluctuations of the fluorescence signal emitted by molecules. Firstly, we developed an approach that combines Image Correlation Spectroscopy with photobleaching to better estimate the surface density of immobilized molecules. The model is useful to overcome the limitation of the standard Image Correlation Spectroscopy when applied to systems of molecules with multi-labeling or aggregates. It has been successfully tested on fluorescence beads that exhibit a wide distribution of brightness. The model was then applied to proteins of the extracellular matrix deposited on the substrate and oligomerization of protein in the cell cytoplasm. Secondly, we performed Raster Image Correlation Spectroscopy on CRY2/CIBN optogenetics cells. Since the technique covers a wide range au diffusional time scales, it is useful to measure the diffusion constant of the cytoplasmic CRY2 proteins and membranous CIBN proteins. We also managed to characterize the dissociation process of CRY2/CIBN.

***Keywords:*** *fluorescence fluctuations, spatial correlations, surface density, optogenetics, diffusion.*

# RÉSUMÉ

En microscopie optique, l'analyse quantitative des processus biologiques est toujours un défi. La Microscopie de Fluctuations de Fluorescence, qui est une famille d'outils d'analyses généralement développés pour les microscopes confocaux, tire partie des fluctuations temporelles et/ou spatiales du signal de fluorescence émis par les molécules. Dans une première partie, nous avons développé une approche qui combine la spectroscopie de corrélation d'images (ICS pour *Image Correlation Spectroscopy*) au photoblanchiment pour mieux estimer la densité de molécules immobilisées sur une surface. Cette méthode étend l'approche ICS standard dans le cas de systèmes de molécules portant de multiples marqueurs ou d'agrégats. Elle a été testée avec succès sur des billes fluorescentes qui présentent une large distribution de brillance. Cette méthode a également été appliquée à des protéines de la matrice extracellulaire déposées sur un substrat et proposé pour étudier l'oligomérisation de protéines dans des cellules fixées. Dans une seconde partie, nous avons appliqué la méthode RICS (pour *Raster Image Correlation Spectroscopy*) sur des cellules optogénétiques CRY2/CIBN afin d'étudier la dynamique de la protéine cytoplasmique CRY2 et de la protéine membranaires CIBN. Cette technique permet de couvrir une large gamme de processus de diffusion ; elle est donc utile pour mesurer la constante de diffusion de ces deux protéines. Nous avons également réussi à caractériser le processus de dissociation de CRY2/CIBN.

***Mots-clés*** *: fluctuations de fluorescence, corrélations spatiales, densité surfacique, optogénétique, diffusion.*

*Karya ilmiah ini adalah sebuah bentuk dedikasi penuh cinta:*
*dari seorang warga kepada negaranya,*
*dari seorang teman kepada handai tolannya*
*dari seorang saudara kepada kakak dan adiknya,*
*dan dari seorang putri kepada orang tuanya.*
*Utamanya pula dari seorang pribadi kepada dirinya,*
*agar dia bisa selalu berkaca kembali dan berkata:*
*" inilah pencapaianku dan aku bangga..."*

# ACKNOWLEDGEMENT

First of all, I would like to express my sincere gratitude to my supervisors, Prof. Antoine Delon and Dr. Irène Wang, for the opportunity to work with them. I have been continuously encouraged, inspired, and tolerated throughout my research work and during the manuscript writing. Their hearts of gold have touched me personally. Nothing could be further from the truth that their invaluable guidance, extensive knowledge, and immense patience have made this thesis possible.

I sincerely thank my thesis reviewers Dr. Rodolphe Jaffiol and Dr. Cyril Favard, for their willingness to review this manuscript and provide feedback. I would like to thank Prof. Irina Mihalcescu and Dr. Didier Marguet, as the jury, for their comments and suggestions to make this manuscript better. I also thank Prof. Warsito, as Education and Culture Attaché of the Indonesian Embassy, for his participation in my thesis defense.

I will not be able to reach this point in my professional life should these people are not crossing my path. I highly appreciate Dr. Martial Balland who has introduced me to his team and allow me to work with them, and who kept me motivated with his high optimism to my work, Dr. Olivier Destaing who has prepared the optogenetics sample and has thoughtfully encouraged me to be a better researcher in the future during our farewell conversation, Dr. Alexei Grichine who has introduced me to the confocal microscope and trained me on Dynascope, Dr. Arnold Fertin who has kindly adjusted the plugins for data analysis to suit my request, Dr. Sigolène Lecuyer and Dr. Delphine Debarre who have trained me on Leica SP8. I thank Dr. Didier Mondelain, Dr. Benjamin Cross, and Dr. Eva Faurobert for their remarks and suggestions on my thesis progress every year in the CSI meeting. I am also grateful for the assistance from my laboratory fellows: Tomas Andersen, Elisa Vitiello, Katharina Hennig, Vanni Petrolli, Adèle Kerdjouan, and Anirban Sarkar, who taught me a detailed preparation of samples, and of course, for the nice conversations and valuable discussions.

This doctoral journey is adventurous yet challenging. Fortunately, I received so many supports from whom I call family and friends. I would like to thank my family-like colleagues at the Department of Physics, Universitas Tanjungpura, for giving me the privilege to pursue the doctoral degree and taking over my responsibilities, and I certainly hope that my presence will be beneficial for all of us. I also thank Siti Nur'aini for having encouraged me to step foot

out of my comfort zone but not forgetting to keep me on track. *Terima kasih saya ucapkan kepada Pradityo Adi Wicaksono, Ali Jaya Meilio, Theodosius Marwan Irnaka, Dwi Adityarini, Revy Marlina, Hanna Martania Permatasari, Alyssa Diva Mustika, Catlea Agatha, Nofriyani Sirait, Istiqomah, Sonny Aribowo, Sophia L Surasetja, Joko Muslim, Tathi Masyitah, Erwin Sentausa, Ingelia Putri, dan teman-teman Persatuan Pelajar Indonesia (PPI) di Grenoble yang telah menjadi tempat bersandar dikala jauh dari keluarga. Je tiens un très grand merci à la famille Caïtucoli qui m'accueille chaleureusement dès mes premiers jours en France, me fait connaitre de la culture et la gastronomie française, et m'offre une consolation quand je me sens perdu.*

I very much appreciate the support from Lembaga Pengelola Dana Pendidikan (LPDP) for a full scholarship to obtain a doctoral degree. LPDP has opened up opportunities for me to dream big. So, as embedded in the heart of every awardee before me, these four words are the promise we keep: *"Indonesia, aku pasti mengabdi."*

Finally, my endless gratitude is for my parents, sister, and brother for their love, support, and prays. *Ibu dan (alm.) ayah tercinta, terima kasih sudah mencurahkan seluruh kasih sayang, menjagaku dalam doa, memberikan pendidikan terbaik, serta mengizinkanku mengejar impian. Adikku tersayang, Afrilya Herianty, terima kasih atas cintamu, tawamu, dan segala pengorbananmu. Mbak sayang dedek. Kakakku tersayang, Agus Fitryansyah, terima kasih sudah membersamai dan menjagaku sejak kecil di sekolah hingga sekarang. Semoga aku membuat kalian semua bangga, dan percayalah semua ini terwujud karena cinta dan doa kalian semua.*

Pontianak, December 2020

Dwiria Wahyuni

# LIST OF FIGURES

# TABLE OF CONTENTS

# Introduction

> *"In physical science, a first essential step in the direction of learning any subject is to find principles of numerical reckoning, and methods for practicably measuring, some quality connected with it. I often say that when you can measure what you are speaking about, and express it in numbers, you know something about it; but when you cannot measure it, when you cannot express it in numbers, your knowledge is of a meagre and unsatisfactory kind; it may be the beginning of knowledge, but you have scarcely, in your thoughts, advanced to the stage of science, whatever the matter may be".* (Lord Kelvin)

Let us begin this manuscript by mentioning a famous quote from Sir William Thomson (Lord Kelvin) [1] delivered in 1883, as written above, that emphasizes the importance of quantification for any parameters one wants to study. We certainly realize that quantification is a key to interpret findings and, therefore, to understand the relationship between observable events. However, wondering whether a quantification method is reliable has always been a question.

Likewise, in life sciences, where microscopy imaging has been a principal technique to observe and analyze biological structures, providing a quantitative aspect has always been a challenge. There are two important events in fluorescence microscopy: the discovery of fluorophores that have carried easiness in discerning proteins of interest from the background and the invention of the confocal microscope that allows thin optical sectioning and reduces

out-of-focus glare. Those two milestones have made quantitative functional imaging to become more feasible, which is beneficial in studying biological processes **(See Chapter 1 for more information)**.

Interactions proteins with biomolecules or other proteins regulate many biological processes. A large percentage of proteins is in dimers or higher-order oligomers forms while conferring everyday functioning. An example of natural oligomeric protein is haemoglobin, which is an oxygen transporter and functionally active as tetramer in higher vertebrates [2]. Identifying the nature of oligomeric states and determining the number of molecules is important. One possible technique to quantify them is to apply methods that are based on fluorescence fluctuations.

The Fluorescence Fluctuation Microscopy (FFM) methods share one key point, to regard the fluctuations as a source of information, rather than noise, for quantitative imaging. The most prominent FFM method is Fluorescence Correlation Spectroscopy (FCS) as the fundamental of other related fluctuation-based techniques [3,4]. The fluctuations in fluorescence, which can arise from processes such as intra- or inter-molecular reactions, diffusion, and transport, make it possible to evaluate the number density, diffusion, velocity, and interaction fraction of fluorescent molecules in the observation volume of the microscope [4] **(See Chapter 2 where we present the basis of these methods)**.

**In this thesis, we intend to exploit some advanced FFM analysis tools, with a focus on two spatial correlation techniques: Image Correlation Spectroscopy (ICS) combined with photobleaching to quantitatively determine the molecular concentration on a surface and Raster Image Correlation Spectroscopy (RICS) to apply on biological samples to observe the molecular dynamics.**

In the first part of our work, we focus on the development of a quantitative technique where we combine ICS and photobleaching to improve the quantification of the surface

density of molecules. *Firstly*, performing standard ICS on immobilized molecules has already given information about their surface density [5]. However, standard ICS can induce a bias when applied to systems such as molecules with multiple labeling or in aggregations state. Photobleaching has been introduced as additional control of such systems, but it is limited to cases of Poissonian labeling or homogenous oligomers. Hence, we propose a general formalism to relate the measured ICS parameters to the distribution of fluorophores. This model is applicable to a system with an arbitrary distribution of fluorophores. The approach is then demonstrated by using fluorescence beads deposited on a glass surface **(See Chapter 3, where results are presented)**.

*Secondly*, following the model that we proposed, we performed a combination of ICS and photobleaching (pICS) to study questions of biological interest. In cellular biology, the protein-surface interaction modulates cell adhesion, which is essential, for example, in cell migration. The adhesion proteins, such as integrins, are located on cell membranes. They establish the adhesion process through their engagement with the ligands of the extracellular matrix, for example, fibronectin, laminin, and collagen, that provide physical scaffolding for the cellular constituents [6]. We would like to estimate the number of molecules of ligands bearing various numbers of fluorophores that attached on the surface with pICS, as well as to have the degree of labeling. On the other hand, since the oligomeric state of cell surface receptors is believed to be linked to their biological functioning [7], we also used our method to perform a preliminary study of oligomerization in the cell cytoplasm (**See Chapter 4 where results are presented)**.

In the second part of the work, where we study the diffusion of proteins in cells, another fluctuation technique is performed, which is Raster Image Correlation Spectroscopy (RICS). The knowledge of the mobility of protein is important to understand the cellular mechanisms. Here, we studied an optogenetic system: a CRY2/CIBN system, which is of

interest to our research team. The CRY2 is a cytoplasmic protein, while CIBN is a protein attached to the membrane via CAAX. RICS analyzes the spatial autocorrelation from the fluctuation signals to calculate the diffusion constant of proteins. The CRY2/CIBN system can be activated upon illumination, where CRY2 will relocate to the membrane and attached to CIBN. The dissociation kinetics of the CRY2/CIBN complex is assessed by measuring the changes of fluorescence signals at the membrane when the cell is placed in the dark after photoactivation **(See Chapter 5 where results are presented)**.

We close the manuscript with a summary of the work.

# Chapter 1

# Fluorescence Microscopy

Long before fluorescence microscopy became an essential tool in analyzing biological systems, light microscopy has been widely used to make biological observations. The history of the light microscope began over 400 years ago when Janssen put a biconvex lens as the eyepiece and a plano-convex lens as an objective in a tube. His microscope was able to magnify an object ten times [8,9]. An *occhiolino* – a perfected version of the microscope by Galileo, was able to widen the field of view by adding a collecting lens [9]. *Micrographia* by Hooke, which illustrated insects, plants, etc., as they had been seen under a microscope, became a significant scientific artwork at the time. However, it was the contribution of van Leeuwenhoek that spotted the light microscope to biologists. He designed a single-lens microscope with 300 times of magnification and able to observe bacteria, nematodes, and spermatozoa [8,10].

When the fluorescence phenomenon was discovered, people were trying to design a microscope by integrating the fluorescence using fluorophores. It is now possible not only to label specifics organelles (nucleus, membranes, *etc*.), proteins and, ions ($Ca^{2+}$), but also, thanks to genetic tools, to transfect cells with fluorescent fusion proteins, which allows

functional imaging. By illuminating a fluorophore-labeled specimen with light corresponding to the fluorophore's absorption spectrum and then collecting the emitted light, the fluorescence microscope is able to visualize specific targets.

In this chapter, fluorescence microscopy will generally be discussed. We will start with the physical mechanism of fluorescence that allows its application to microscopy. The fluorescence can occur as a natural autofluorescence of a specimen or from a fluorescent substance, a fluorophore, tagging onto the specimen. However, the fluorophores may go through photochemical alteration, which is known as photobleaching, where they are no longer able to fluoresce. We will describe the application of fluorophores and the photobleaching phenomenon in fluorescence microscopy. Lastly, in the context of this thesis, we will briefly outline the foundations of the confocal microscopy technique.

## 1.1 Fundamental of Fluorescence

Like any other microscope, the fluorescence microscope also provides an enhanced image of a specimen that cannot be seen by naked eyes. However, the use of autofluorescence properties or fluorescent labeling offers an advanced feature for fluorescence microscopy in acquiring information about specific molecules. Thus, it allows the fluorescence microscopy to observe in greater detail, to manipulate and track more precisely the processes *in vivo* and in real-time [11].

### 1.1.1 What is fluorescence?

The observation of fluorescence, which was termed as *epipolic* dispersion, was first reported in 1845 when Herschel remarked a clear blue light was emitted from a colorless quinine sulfate solution as he sent a certain incidence of ultraviolet light. However, it was the work of Stokes in 1852 that put on detailed this optical phenomenon. He illuminated a

solution of quinine with invisible ultraviolet and observed that the emission light was shifted into a longer visible wavelength radiation, which was later known as the Stokes Shift. This led to research attempting to apply the fluorescence into microscopy, from Köhler who developed the ultraviolet microscope up to the construction of the first fluorescence microscope by Heimstädt and Lehmann in 1911 [10]. They managed to observe the autofluorescence of some biological samples: bacteria, protozoa, tissue, and bioorganic substances.

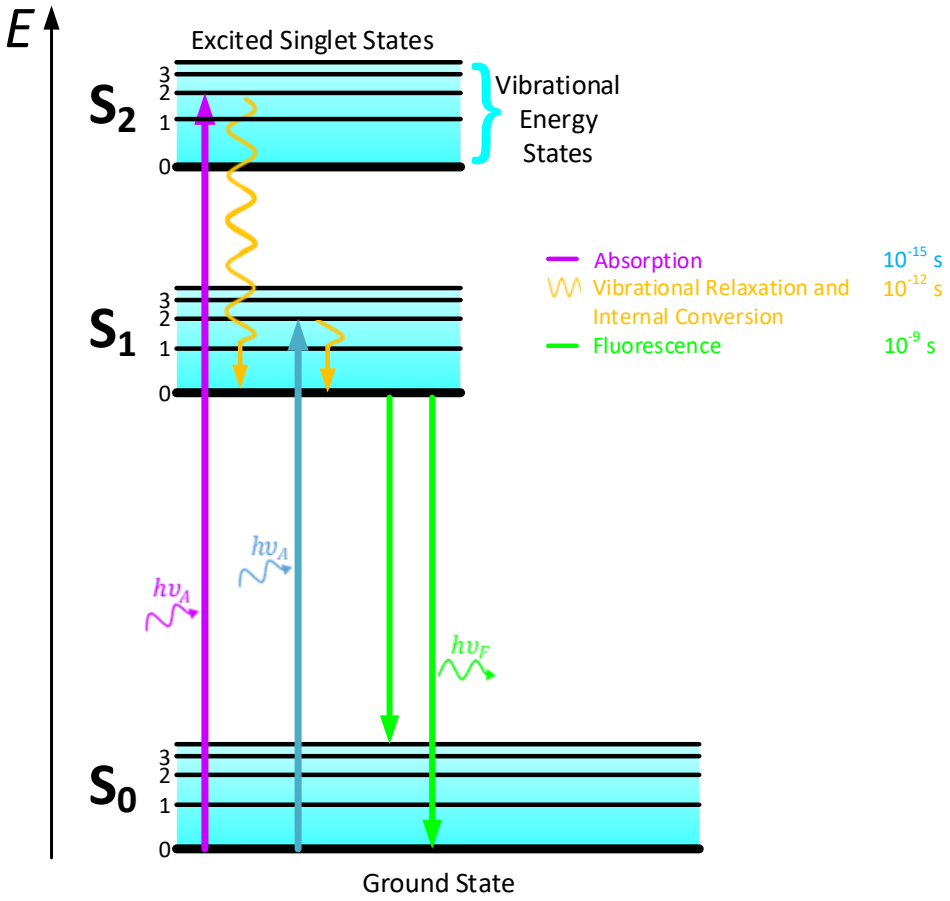


Figure 1.1: ***A typical Jablonski diagram***. *Molecules are excited from the ground state to a higher energy level by absorption of a photon from an external source. As the molecules return to the ground state, photons are emitted. In fluorescence, the excitation does not change the electron spin direction. Adapted from* [12].

Fluorescence and phosphorescence are specific parts of photoluminescence which are governed by a three-stage process: electronic excitation of a molecule as it absorbs light at a given wavelength, vibrational relaxation of electron from the excited state to the lowest

vibrational level, and photon emission with a longer wavelength (less energy) when returning to a stable state. Fluorescence lifetime is much shorter (typically in nanoseconds) than phosphorescence (typically from microseconds to seconds). The mechanical process of light absorption and emission is illustrated by the Jablonski diagram (Fig. 1.1).

The Jablonski diagram visualizes the possible transitions of molecules after photoexcitation. The vertical axis indicates energy. Horizontal black lines are electronic energy states of a molecule where each of them has vibrational energy states (from lowest to highest energy levels as numbered by 0, 1, 2, …). Singlet states, with a total spin angular momentum of zero, are depicted by ground state ($S_0$) and excited states ($S_1$, $S_2$, etc.). The first excited triplet states, with a total spin angular momentum of one, is denoted by $T_1$. Absorption of a photon of energy $h\upsilon_A$ (purple and blue line) from external invisible or UV light drives an excitation of the molecule. The transition from the ground state to the excited state occurs in femtosecond timescale. The excited states which last for a finite time (a few nanoseconds) are non-equilibrium states. Here, the molecule energy is dissipated due to vibrational relaxation (yellow arrows) until it reaches the lowest vibrational level. When the molecule is in a higher excited state, it undergoes an internal conversion to a lower excited state then followed by vibrational relaxation. Hence, the molecule that returns to the ground state results from the lowest vibrational energy state of $S_1$. The fluorescence emission (green lines) from the returning photon has lower energy $h\upsilon_F$ than that of the absorption [12].

The fluorescence, as mentioned above, involves a loss of energy during the process. The energy of the fluorescence photons is typically lower than that of the absorption ones. In other words, the fluorescent molecule, or fluorophore, is excited at a shorter wavelength (toward blue), but the emitted photon has a longer wavelength (toward red). This change is called the Stokes' shift (Fig. 1.2) that describes the difference between the maxima of fluorophore absorption and emission wavelengths.

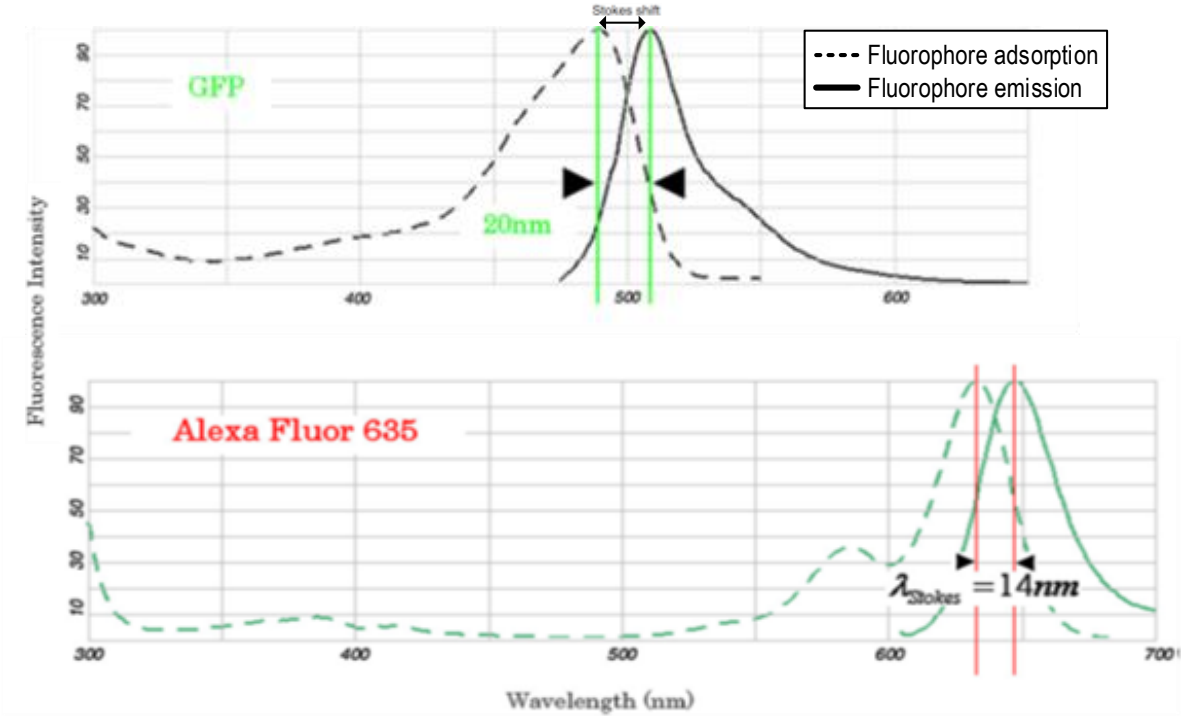


Figure 1.2: ***Stokes' shift on the spectrum of fluorophores***. *The peak of GFP and Alexa Fluor emission spectra is shifted from the peak of excitation wavelength due to photon energy loss. Adapted from* [13].

Figure 1.2 shows fluorescence spectra for Green Fluorescence Protein (GFP) and red Alexa Fluor. The difference in absorption and emission maxima is in few tens of nanometers. To obtain maximum fluorescence intensity, the fluorophore should be excited with a wavelength near to or at the excitation maximum (490 nm for GFP and 633 nm for Alexa), and the detection range should include the peak of emission maximum. In fluorescence spectroscopy, a higher Stokes' shift is advantageous because it would be easier to spectrally separate the excitation from the emission by optical filters.

### 1.1.2 Fluorophore: a probe to create a molecular reporter

At the beginning of its development, despite a successful observation of biological samples by Heimstädt and Lehmann [10], fluorescence microscopy had a limited initial application because it relied only on the autofluorescence of the object. It was two decades

later that a technique of secondary fluorescence was developed by Haitinger and some other scientists [14]. This technique used fluorescent chemical compounds stained onto samples that he termed as fluorochrome (*i.e.*, **fluorophore**). Research to invent fluorescent probes and reporters has been carried out since then, and by now, thousands of fluorophores can be found [12] spanning from the ultraviolet to near-infrared spectral regions.

The fluorophore is essential in fluorescence microscopy to obtain a keen image of a sample. One can opt for organic fluorophore, fluorescent protein, or quantum dots. An organic fluorophore is a small molecule (0.2–1 kD), which can be either natural or synthetic. It can be coupled to macromolecules such as proteins. Organic fluorophores cover a broad range of absorption-emission wavelengths up to the near-infrared region (with a peak emission >700 nm). Examples of these fluorophores are Fluorescein, Rhodamine, and Alexa Fluor [15]. Fluorescent proteins have much larger weights (~25 kD) compared to organic fluorophores that are typically less than a kDa [16]. The genetically encoded green fluorescent protein (GFP) is one of the commonly used fluorescent labels. The advantage of fluorescent proteins is that they can be fused to the protein of interest to image its localization and dynamics in living cells [17]. The fluorescent proteins are available in colors from blue to far-red. However, unlike organic fluorophore, no near-infrared fluorescent protein has been developed [18]. Quantum dots are semiconductor nanocrystals that have controllable core sizes, which generate a wide range of emission peaks. The excitation spectra of quantum dots are broad, making it possible to choose a unique excitation wavelength far from the emission ranges to avoid background scattering. Nonetheless, the large size of quantum dots (10nm) limits their diffusion across the cellular membrane, causing no emission is read [19]. In comparison to organic dyes, quantum dots have a greater photostability at similar wavelengths [20], although they are also reported to be toxic [21].

Understanding the properties of fluorophores is a way to decide which fluorophore to use besides importantly knowing the type of measurement (conformational changes, protein-protein interaction, single-particle tracking, protein counting, or live cell localization) one would like to perform [15]. The spectral properties (excitation and emission spectrum) are common optical criteria of fluorophores, which have been explained previously by the Jablonski diagram (Figure 1.1). Among others, crucial properties that should be noticed for a preferable fluorophore are high fluorophore brightness, which is the product of fluorescence quantum yield and extinction coefficient, and optimum photostability [13,22]. The latter will have its dedicated section later in this chapter.

The extinction coefficient (expressed in $M^{-1}cm^{-1}$) quantifies the quantity of light that can be absorbed in a specific wavelength for one molar concentration of these fluorophores. Fluorophores with a high extinction coefficient will absorb more light. The organic fluorophores and fluorescent proteins have extinction coefficients of $10^4 – 10^5$ $M^{-1}cm^{-1}$ [23].

Fluorescence quantum yield $(\phi_{fl})$ measures the fluorescent efficiency that is the ratio of the number of emitted photons (radiative rate constant, $k_r$) to the total decay rate (sum of radiative and non-radiative decay rate constants, $k_r + k_{nr}$)) [13] expressed as

$$\phi_{fl} = \frac{k_r}{k_r + k_{nr}} \tag{1.1}$$

The fluorescence quantum yield goes towards unity when the non-radiative rate gets negligible compared to the rate of radiative transition. A fluorophore with a high quantum yield is preferable for an experiment. It is worth to notice that the quantum yield is also affected by the fluorophore environment [15], such as temperature, ionic strength, and pH. A high excitation intensity can also decrease the fluorescence quantum yield because of non-linear processes.

The fluorescence (excited state) lifetime is the average time the fluorophore spends in the excited state S1, prior to returning to the ground state. It is related to the radiative and non-radiative rate constants as [13]

$$\tau_{fl} = \frac{1}{k_r + k_{nr}} \tag{1.2}$$

The lifetime also depends on environmental factors. Fluorophores generally have a fluorescence lifetime in the range of nanoseconds [15].

One of the most used fluorophores is a green fluorescent protein (GFP). It was isolated from jellyfish *Aequorea victoria* (Fig. 1.3(a)) in 1961 as a by-product of aequorin, which was the actual bioluminescent protein target [24]. Although its chromophore had been identified, GFP remained useless for the next 30 years [25] until it was cloned and used for tracking gene expression in bacteria and the sensory neurons of the nematode *C. elegans* [26] that marked a major breakthrough for cell biology and a revolution in optical microscopy [27]. Since then, research had been carried out to produce mutants of the wild-type GFP through a single-point mutation genetic engineering [28] and of other species such as Anthrozoa species in corals, which are referred to yellow (YFPs) or red (RFPs) fluorescent proteins [12]. By now, a palette of fluorescent proteins is accessible (Figure 1.3(c)) with spectrum maxima from the blue region (eBFP; 380/440 nm) to the red region (mPlum; 590/648 nm). A unique feature of GFPs and GFPs-like is that the chromophore is formed spontaneously after cyclization of the polypeptide chain and can fluoresce without the need of cofactor. Consequently, they can be applied as genetic tracer molecules in cells [12]. Due to their roles in the discovery and development of GFP, three scientists: Shimomura, Tsien, and Chalfie, had jointly received the Nobel Prize in Chemistry in 2008.

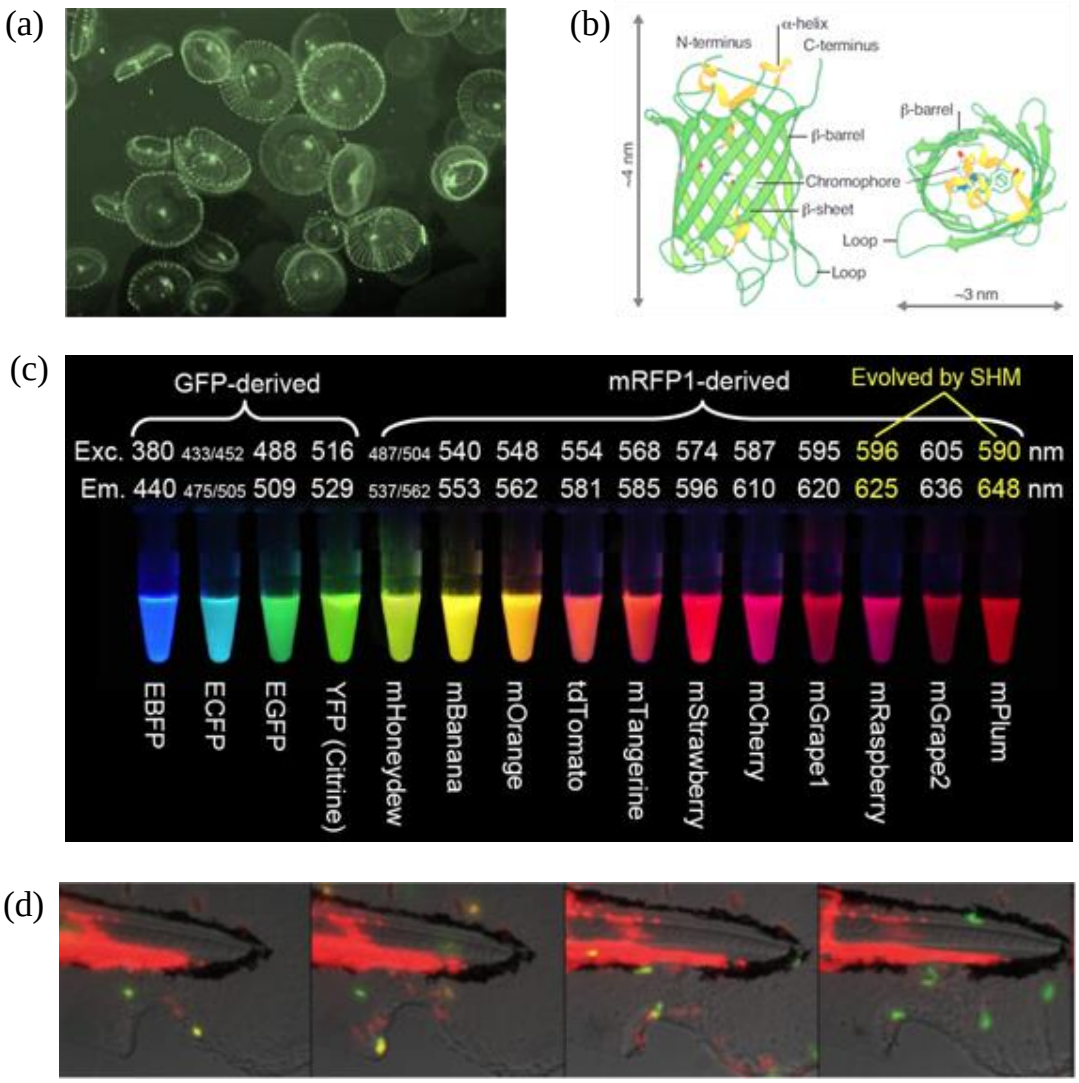


Figure 1.3: ***Green Fluorescent Protein (GFP); its origin and application***. (a) *Jellyfish Aequorea victoria is found in coastal waters and emits light in the blue-green region.* (b) *The backbone fold of GFP, where its chromophore is shielded by β-barrel structure.* (c) *A palette of engineered fluorescent proteins spanning from blue to far-red spectral region.* (d)*Application of fluorescent proteins to image wound healing in zebrafish; neutrophils express GFP, and the entire blood cell lineage is mCherry. During the first few hours, macrophages (red) and neutrophils invade the wound area and eventually clear the area of bacteria and debris to allow wound healing. Adapted from* [16,24,28,29].

### 1.1.3 Photobleaching

Despite its advantages in providing a keen image of an object, fluorescence microscopy has some limitations, among which irreversible photobleaching of the fluorophores is unavoidable. Photobleaching is a phenomenon where an assembly of fluorophores emits a gradually fading light with time (Fig. 1.4) due to a photo-induced

chemical modification of the fluorophore. Meanwhile, at the single-molecule level, the emission rate instantaneously drops to zero and is irreversible. Photobleaching is favored by many factors including, molecular collisions, energy transfer, metastable triplet state, and presence of oxygen [13].

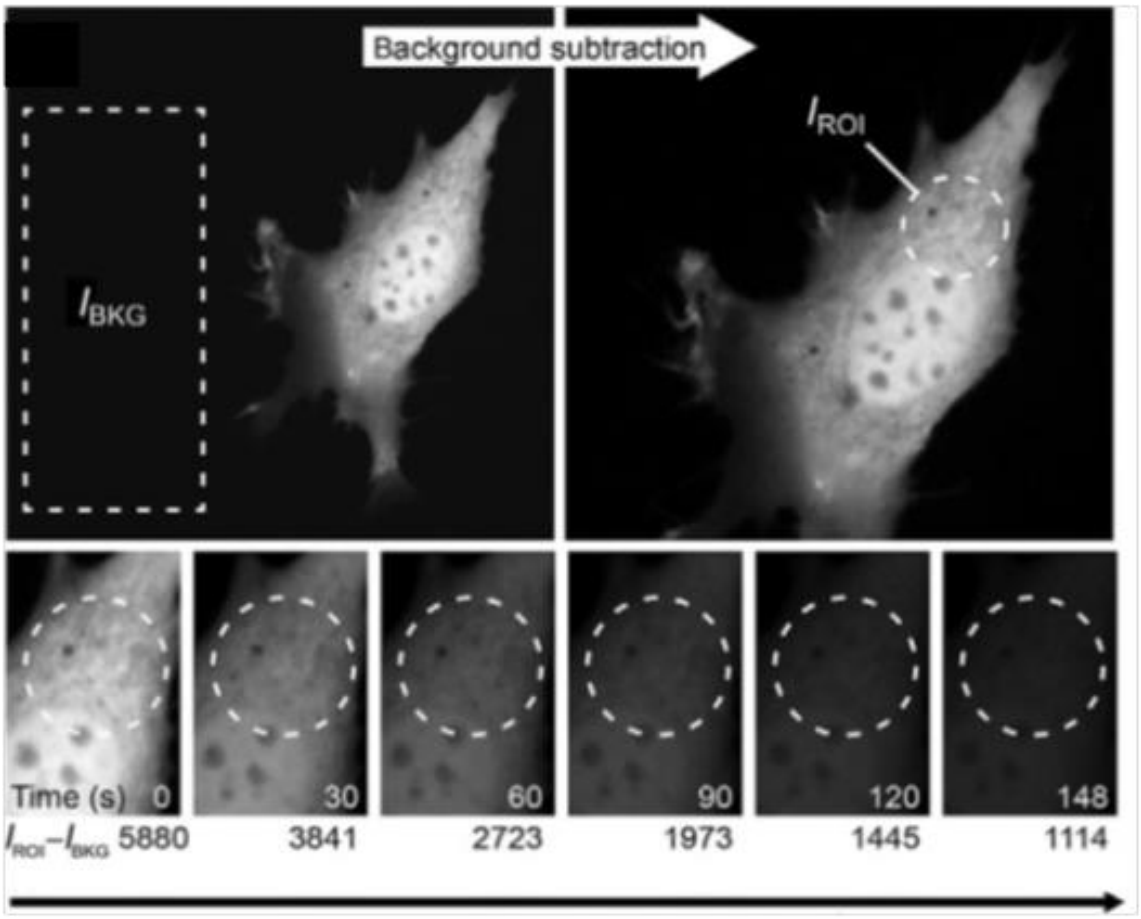


Figure 1.4: ***Photobleaching time-lapse sequences***. *Photobleaching on a cell that expressed by GFP can be identified from the loss of fluorescence intensity on a region of interest (ROI), $I_{ROI}$. Quantification of mean intensity is corrected by subtraction of background intensity ($I_{BKG}$) calculated from mean intensity outside the cell. Adapted from* [30].

Fluorophores are prone to photobleaching, which is generally undesirable as it can lead to loss of information. Even though no simple solution has been established to eliminate the photobleaching [30], the impact of photobleaching on imaging can be reduced by optimizing the fluorescence imaging system settings, which include compromising laser power and the frequency and duration of illumination.

The number of excitation-emission cycles, that is, of emitted detectable photons before a molecule, on average, is bleached is called the photon budget. For example, a single molecule of fluorescein isothiocyanate (FITC) is estimated to have about 30,000 cycles before it stops emitting photons [31].

As mentioned earlier, low photobleaching quantum yield and a small effective photobleaching rate are preferred for a fluorophore. The photobleaching quantum yield, $\phi_b$, is the ratio of the number of photobleaching events to the total number of absorbed photons. More photostable fluorophores such as Rhodamine and eGFP are reported to have photobleaching quantum yield $\phi_b \approx 10^{-7} - 10^{-6}$ and $\phi_b \approx 10^{-5}$, respectively [22,32]. On the other hand, fluorescein protein with $\phi_b \approx 10^{-4}$ is prone to photobleaching [33] even though its fluorescence quantum yield attains 0.95 [12].

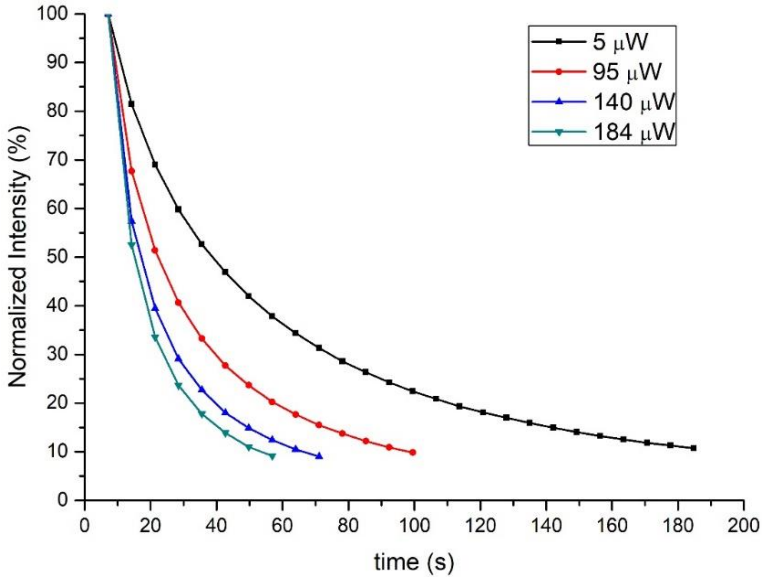


Figure 1.5: ***Fluorescence decay due to photobleaching***. *Rhodamine tagged to fibronectin protein emits fluorescence signals that decrease gradually with time. The faster the absorption rate because of the increase of the laser power, the shorter the fluorescence decay time will be.*

The effective photobleaching rate, $k_b$, is related to the survival time of fluorophore, $\tau_b = 1/k_b$, which is the average time during which a fluorophore can emit photons before it

loses the ability to fluoresce. This rate is the product of the absorption rate of photons times the photobleaching quantum yield:

$$k_b = k_a \phi_b \tag{1.3}$$

Generally, in experiment as in Fig. 1.5 for photobleaching of Rhodamine, we could observe the rate of photobleaching is higher when we increase the laser power.

On the other hand, certain specialized techniques have exploited the photobleaching of fluorophore since the 1970s. One widely used technique is fluorescence recovery after photobleaching (FRAP) to quantify the dynamics of fluorescently tagged molecules on the cell surface or inside the cytoplasm and observe the molecules binding interaction. FRAP takes advantage of the rapid and irreversible photobleaching of fluorescently labeled molecules within a region of interest (ROI). The photobleaching is completed by using an intense laser for short durations of time. Then, the fluorescence intensity of an ROI and its surroundings is monitored using a low-intensity excitation light. The recovery-rate constant within the ROI gives information related to molecular diffusion and binding interactions [34,35].

## 1.2 Confocal microscopy

Biological specimens have various thicknesses because of their internal structures. When the fluorophore is tagged onto the specimen, the conventional fluorescent light microscope will also detect light from above and below the focal plane, causing the image to blur and to lose contrast [8]. To introduce optical sectioning in fluorescence images, a confocal microscope system (Fig. 1.6(c)), to which a pinhole aperture was integrated, was introduced and patented by Minsky in 1961 [36]. Confocal microscopy is an imaging technique that uses pinhole aperture to eliminate out-of-focus glare on a specimen. The in-focus volume within a sample that is efficiently detected is called the confocal volume, which

depends on the laser focusing and the size of the pinhole. One should always keep in mind that the microscope produces a two-dimensional image of a specimen that is three-dimensional. In a laser scanning confocal microscope, a complete image of a selected area is generated by scanning the focal point of illumination across a specimen. By taking a series of two-dimensional images at different depths (Fig. 1.6(a)), a three-dimensional image can be reconstructed with confocal microscopy (Fig. 1.6(b)).

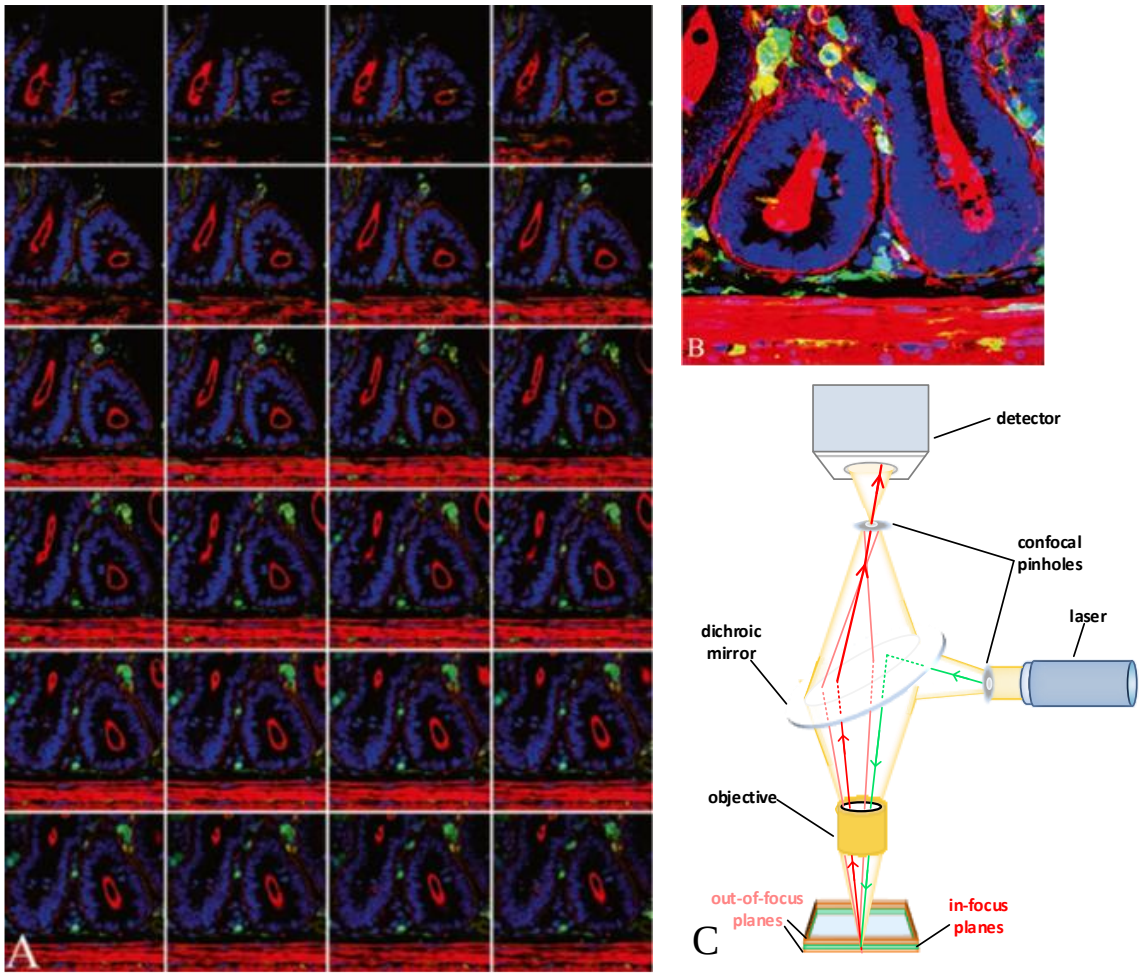


Figure 1.6: ***Confocal microscopy***. *(A) Optical sectioning with z-series through a section of intestine stained with multiple fluorescent dyes; blue: DAPI stain for nuclei, red: f-actin stain, green: GFP, yellow: mRNA stabilizing protein. (B) Image reconstruction of all sections in (A). (C) Scheme of laser scanning confocal microscope. Exciting laser light is reflected by a dichroic mirror and focused on the specimen in a focal plane. As the laser scans, fluorescence emitted from the focal plane passes through the mirror, and only light that passes through the pinhole aperture is detected and forms the image. Adapted from* [31].

As in other imaging systems, image formation in the confocal microscope involves the Point Spread Function (PSF) that can be described as an image of the intensity distribution of an infinitely small point object [37]. The PSF depends on the numerical aperture (NA) of the objective and the size of the pinhole. For eGFP emitting at 510 nm through a 1.4 NA objective on the confocal microscope, the theoretical maximum lateral resolution is ~200 nm and axial resolution of ~800 nm [38].

Selecting and adjusting the confocal microscope parameters in making an image acquisition is sometimes confusing. It is worth noticing that adjusting one parameter (for example: increasing the dwell time to collect more photons) could make other things worse (like photobleaching).

Pixel dwell time, scanning speed, pixel size, and light source are relevant points to optimize when acquiring images. The pixel dwell time, which is controlled by scanning speed, refers to the time spent by the laser to scan a pixel. Therefore, it affects the number of photons entering the detector resulting in lower pixel intensity for faster scanning. Meanwhile, appropriate pixel sizes for the image acquisition are of the order of 100 nm/pixel. These sizes are enough to sample the point spread function of the confocal microscope.

A laser is used as a source of light for a confocal microscope. The choice of laser lines depends on the fluorophores: 561nm-laser line to excite Rhodamine or 488nm-laser on eGFP. Adjusting the suitable laser power is crucial to record a sufficient signal-to-noise and to avoid photobleaching. It is important to notice that the photobleaching properties of molecules that we mentioned previously are subject to a low excitation irradiance.

Reminding some basic concepts of fluorescence microscopy, which we have described above, is required when one wants to obtain proper imaging. In the next chapter, we will present how to extract quantitative information from the fluorescence images collected by the microscope using analytical tools of fluorescence fluctuations.

# Chapter 2

# Fluorescence Correlation Techniques

Fluorescence microscopy allows us to study biological processes in real-time, either at the cellular or molecular levels. One of the quantitative techniques using fluorescence microscopy is Fluorescence Fluctuation Microscopy (FFM), which is a family of techniques utilizing the intensity fluctuations due to molecular mechanisms such as particle movements, conformational changes, chemical, or physical reactions. This technique has been developed and used to study molecular dynamics [39], protein interactions [40], and to determine the degree of aggregation of proteins by characterizing the molecular brightness of fluorescent protein from the number of particles in a given volume [41].

One of the most widely used fluctuation techniques is Fluorescence Correlation Spectroscopy (FCS). In this chapter, we describe the fundamentals of FCS, which is based on the temporal correlation of intensity from a very small detection volume. Some extensions of FCS measurement will also be mentioned here as we exploit them in this thesis.

## 2.1 Fluorescence Correlation Spectroscopy

The Fluorescence Correlation Spectroscopy (FCS) technique was first introduced in 1972 [42] as a correlation method to observe the relaxation of a thermodynamic equilibrium system, followed by some development of the technique in the following years [3,34,43]. However, in the first works of FCS, the amplitude of measured fluorescence intensities was small against a background noise [44] due to low detection efficiency and a large number of particles; also, a significant amount of time was needed to achieve an acceptable signal-to-noise ratio [45].

For the fluctuations to be visible, the concentration of fluorophores in the sample and the observation volume have to be small enough so that the relative fluctuations that scale as a reciprocal of the number of molecules, $1/N$, are not drowned in the noise and parasites. Nowadays, the typical concentration for FCS measurement is between sub-nanomolar ($< 1$ nM) and micromolar, and the experimental observation volume is around one femtoliter, which corresponds to a volume of an E.coli bacterial cell. With the invention of the confocal microscope, where the volume of observation is reduced with the utilization of wide aperture lenses in the confocal optical arrangement, the FCS technique has been improved and can now be considered to be a well-established technique [46].

In respect of the classical relaxation methods, the novel concept FCS relies on spontaneous fluctuations of fluorescence intensity caused by deviations from a mean. These fluctuations, instead of being considered as a noise that perturbs the signal, are treated as a source of information related to the dynamics of the molecules that can be extracted by temporally autocorrelating the recorded intensity signal [47].

As introduced before, fluctuations in the fluorescence signals are caused by different processes, for example, molecular diffusion, fluorophore blinking, conformational transitions, quenching associated with aggregation, and molecular rotations. In a specific case of

diffusion, the fluorescence signal should exhibit a self-similarity on time scales smaller than or equal to the time the fluorophores take to diffuse through the confocal volume. The autocorrelation analysis measures the probability that the signal at different times still belongs to the same molecular event. Thus, evaluating the time scale where the self-resemblance disappears yields information about the diffusion time of the molecules. The autocorrelation function can be written as

$$G(\tau) = \frac{\langle \delta F(t) \delta F(t+\tau) \rangle}{\langle F(t) \rangle^2} \tag{2.1}$$

where $F(t)$ is the fluorescence intensity at time $t$, while $\tau$ is the correlation (or lag) time, and $\delta F(t) = F(t) - \langle F(t) \rangle$ are the fluctuations around the mean value.

The autocorrelation function can be expressed by the following analytical formula if the observation volume is approximated by a three-dimensional Gaussian profile [47]

$$G(\tau) = \frac{1}{N}\left(1 + \frac{\tau}{\tau_D}\right)^{-1}\left(1 + \frac{\tau}{S^2\tau_D}\right)^{-1/2} \tag{2.2}$$

where the diffusion time $\tau_D = \omega_0^2/4D$ is related to the diffusion constant $D$ and the lateral waist $\omega_0$ of the observation volume. In this equation $1/N$ represents the zero-lag amplitude of the autocorrelation function, where $N = C \cdot V_{eff}$ is the average number of particles of concentration $C$ in the effective detection volume $V_{eff} = \pi^{3/2}\omega_0^3 S$. The parameter $S$ depicts the elongation of the observation volume, with $S = \omega_z/\omega_0$, where $\omega_z$ is the axial waist (half-length) of the observation volume. The parameters $\omega_0$ is usually determined by a calibration measurement using a dye with a known diffusion coefficient.

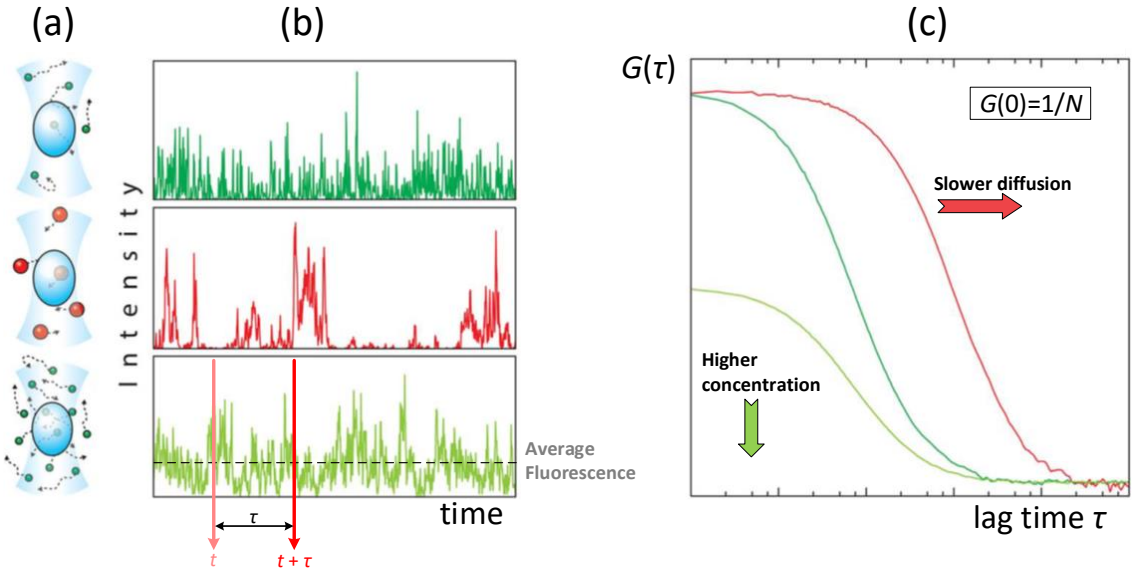


Figure 2.1: ***Fluorescence Correlation Spectroscopy***. *(a) Schematic representation of the observation volume (light blue), slow (red) or fast (green) moving fluorescent molecules, and a higher concentration (light green) of fast-moving fluorescent molecules. (b) The movement of the molecules through the observation volume generates fluctuations in the intensity trace. (c) The autocorrelation value when* $\tau = 0$ *is inversely proportional to the occupation number, so the amplitude of the function decreases as the molecular concentration increases (green arrow) and its decay time reflect the diffusion coefficient (red arrow). Adapted from* [48].

The spontaneous motion of the fluorescent molecules through the observation volume introduces fluctuations in the intensity trace, as shown in Fig. 2.1, of which duration depends on how fast the molecules move. Slow-moving molecules spend a longer time to pass through the observation volume, thus generate long-lasting fluctuations. In this case, the autocorrelation function of the slow-moving particles will slowly decrease with $\tau$ compare to the fast-moving molecules. On the other hand, when molecules of high concentration (and therefore a large number of molecules) are located within the observation volume, the change in fluorescence signal $\delta F$ due to one fluorescent molecule going in-and-out of the volume will be small. Hence, the amplitude of the autocorrelation function is lower in comparison to a case with a low concentration [48].

## 2.2 Extension of Fluorescence Correlation Spectroscopy

In spite of being well-known as a minimally invasive technique and versatile to various applications, Fluorescence Correlation Spectroscopy (FCS) is mostly concerned with systems with fast dynamics, such as diffusion in solutions, cytoplasm, etc. The accessible timescales range for FCS from several sub-microseconds to several hundred milliseconds. Therefore, molecules that have slow dynamics (such as membranous molecules) or even those that are immobile (such as proteins bound to the cytoskeleton) cannot be studied using this technique. When molecules are not fast enough, significant acquisition time is needed to have a sufficient signal-to-noise ratio so that the molecules can be photobleached before leaving the measurement volume and spurious sources of drift can become dominant. In the case of immobile molecules, there are no occupancy changes on the confocal volume; thus, no fluctuations will be detected.

Novel techniques have been developed as extensions of FCS, terming as Image Correlation Spectroscopy (ICS) techniques, to overcome the limitations of FCS within the scope of fluorescence fluctuation methods, as shown in Figure 2.2. These techniques, which correlate images acquired with the laser scanning confocal microscope, have the same principle of the analysis as in FCS. In general, image correlation techniques are basically classified based on how the images are analyzed, whether it is correlated in space (spatial ICS [5], Raster ICS (RICS) [49]), in time (Temporal ICS (TICS) [50], *k*-space temporal ICS (kICS) [51]), or in both time and space (Spatiotemporal ICS (STICS) [52]).

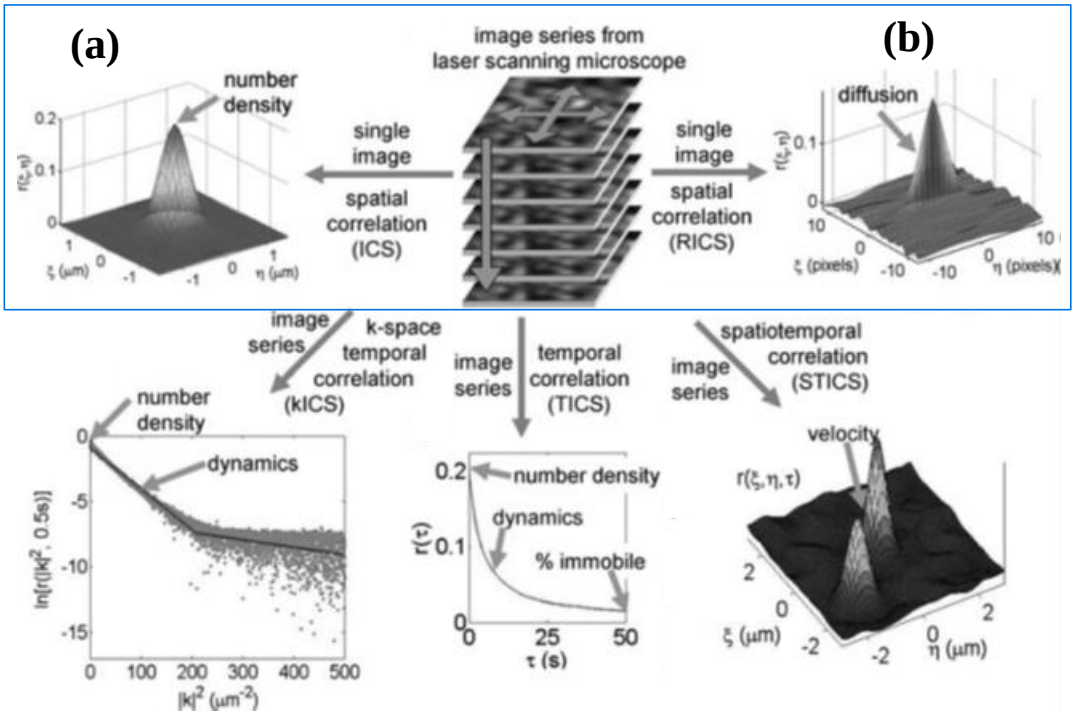


Figure 2.2: ***Image Correlation Spectroscopy Techniques***. *Several variants of image correlation spectroscopy were developed with the purpose of extracting information such as concentration, diffusion, flow, dynamics, and the fraction of immobile molecules. Two techniques (blue box) are chosen for this thesis: (a) Spatial Image Correlation Spectroscopy (ICS) and. (b) Raster ICS (RICS). Taken from* [4].

Throughout the thesis, we exploit two fluctuation methods: Spatial Image Correlation Spectroscopy (ICS) and Raster Image Correlation Spectroscopy (RICS). Spatial ICS is performed on a system of immobile molecules to determine the density or aggregation state of molecules based on spatial autocorrelation of the fluctuations on an image. On the other hand, RICS is applied to a system of fast-diffusing molecules. Images acquired by raster scanning contain spatial and temporal information; thus the spatial autocorrelation of the images also contains spatiotemporal information, which allows us to measure fast transport dynamics [53]. A prominent distinction between these two ICS techniques lies in the way of exploiting the autocorrelation function to obtain the corresponding information. Spatial ICS hinges on the amplitude on the autocorrelation function, which tells the number density or aggregation states, while RICS relies on the shape of the autocorrelation function to extract the diffusion.

# Chapter 3

# Combination of Image Correlation Analysis and Photobleaching

One common and challenging problem in fluorescence microscopy is to determine the number of molecules and aggregations of molecules (*i.e.*, aggregates of molecules or multi-labeled molecules) in images. In general, the standard Image Correlation Spectroscopy (ICS) renders the number of molecules and the aggregation state based on the molecular brightness. However, if the system of molecules holds a distribution of brightness, performing standard ICS may introduce a systematic bias when determining the aggregation states because the brightness is varied from one aggregate to another.

Photobleaching Image Correlation Spectroscopy (pICS) is a relatively new method and first introduced as an alternative method to determine oligomeric states by analyzing the brightness of molecules but without the necessity of calibrating to a monomeric fluorophore brightness. However, the pICS method has only been applied to specific cases such as molecules with a homogenous size of oligomers or with the Poisson distribution of labels.

We propose a general formalism that relates the ICS output (average number of molecules and brightness) to the initial distribution of fluorophores. Hence, this model is

applicable to a system with an arbitrary distribution of fluorophores and allows to extract some statistical parameters related to the distribution.

We start this chapter by presenting the conventional ICS, followed by analytical derivation to construct our pICS model. After that, we describe the procedure to validate our method using fluorescence beads attached to a glass surface. Finally, we used particle counting to obtain more information about the sample, and we would like to see if there is consistency with our pICS model.

## 3.1 Spatial Image Correlation Spectroscopy (ICS)

Fluorescence Correlation Spectroscopy (FCS) technique analyzes the fluctuations of molecules passing through the beam. When the molecules are immobile, one can change the fluctuations detection manner by moving the beam to scan the surface, so-called Image Correlation Spectroscopy (ICS). This technique takes advantage of the spatial fluctuations of the fluorescence signal in an image to determine the surface density of molecules [5]. This information is obtained by considering that the amplitude of the normalized spatial autocorrelation function of an ensemble of evenly distributed immobile points is inversely proportional to the surface density (its width being related to the Point Spread Function (PSF) of the imaging system).

The fluorescence signal, $F(x,y)$ has an average intensity of $\langle F \rangle$ and fluctuations of $\delta F(x,y) = F(x,y) - \langle F \rangle$. When the autocorrelation analysis is performed, we correlate the intensity fluctuations at every pixel in a single image with that at a shifted point in the same single image (Fig. 3.1(a)), with a proper normalization

$$G(\xi,\eta) = \frac{\langle \delta F(x,y)\delta F(x+\xi,y+\eta)\rangle}{\langle F(x,y)\rangle^2} \tag{3.1}$$

where $\xi$ and $\eta$ are the shift variable in *xy*-space, and the angle brackets, $\langle \quad \rangle$, indicate an integration over all spaces. Over a short shift, the fluorescence signals are relatively similar, and the amplitude of the autocorrelation curve is high. Over a larger shift, the signals become less similar and the correlation function tends to vanish. Then the calculated spatial autocorrelation function of the PSF is usually fit with a Gaussian function [5]

$$G(\xi,\eta) = G(0)\exp\left(-\frac{(\xi^2+\eta^2)}{\omega_0^2}\right) + G_\infty \tag{3.2}$$

Since the image is restricted in size, it is usually difficult to sample enough data to allow the correlation function to vanish at large correlation distances. Therefore, the term $G_\infty$ is an offset that is introduced to account for incomplete decay of the correlation function. The term $G(0)$ represents the zero-shift amplitude of the correlation function, which is related to the average number of particles, *N*, within the observation volume (*i.e.*, PSF) of radial extent $\omega_0$, and written as

$$G(0) = \frac{1}{N} \tag{3.3}$$

Here, it is assumed that the size of the fluorescence particles or molecules are much smaller than the PSF of the imaging system. Any decrease in the surface density of the molecules would increase the autocorrelation amplitude. As the confocal microscope scans the surface, a less dense surface would have fewer excited molecules in the observation area. Consequently, the magnitude of the autocorrelation function increases due to a higher relative fluctuation between pixels (Fig. 3.1(d)). Conversely, when the concentration becomes too high, the surface becomes crowded with the molecules, which tend to interact or to form structures. The practical limit to perform ICS is thus given by the appearance of fluorescent structures due to diffusion of molecules on the surface and aggregation, that occur at high density, which lead to signals that dominate the autocorrelation function.

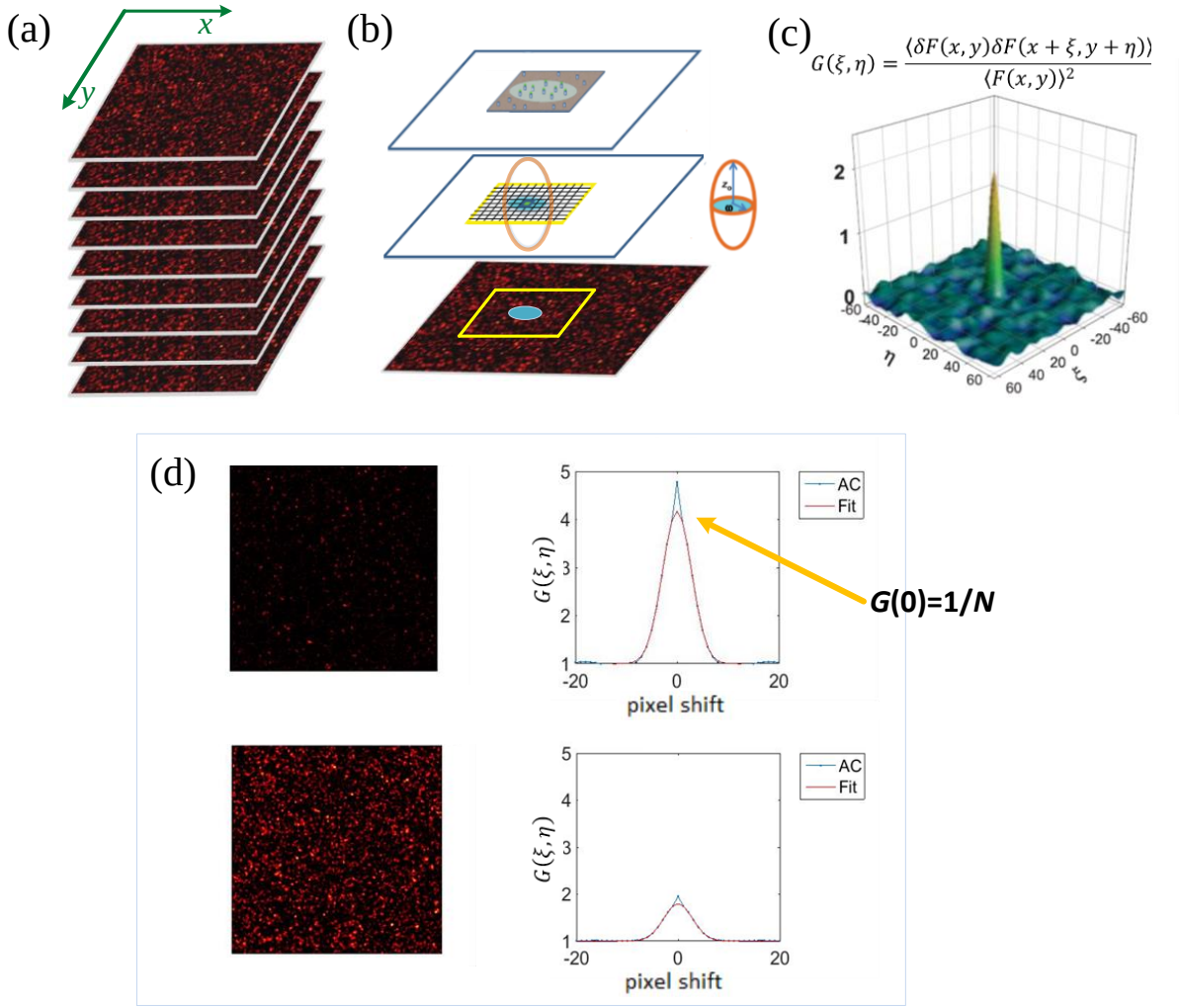


Figure 3.1: ***Spatial ICS***. *(a) Schematic of an image series acquired with laser scanning confocal microscope (b) A region of interest (yellow rectangle) in xy-space in a single image is selected, and a spatial correlation function is calculated from the chosen pixels (c) A spatial correlation function shows the peak amplitude at zero spatial lags. This amplitude is inversely proportional to the mean number of independent fluorescent entities in the focal volume/area. (d) The autocorrelation profile from fluorescence images shows a lower amplitude when the surface is denser because fewer fluctuations are recorded. Adapted from* [54].

## 3.2 Photobleaching Image Correlation Spectroscopy (pICS)

Image Correlation Spectroscopy (ICS) is straightforwardly applicable for immobilized molecules with a homogenous (*i.e.*, unique) brightness. However, the number of molecules (*i.e.*, their surface concentration) obtained by this method is biased with systems of molecules holding multiple labeling or molecular aggregations. More precisely, the systems we refer to

could be a biomolecule bearing multiple fluorophores (for instance, Fibronectin having 1 to 3 fluorophores/ligands, Fibrinogen that has approximately 15 fluorophores/ligands), a bead containing multiple labels, or aggregation of single molecules or beads. Consequently, instead of having a unique brightness, these entities come with a distribution of brightness, which contributes to the overall fluctuations of intensity that must be considered in the analysis.

For that reason, photobleaching has been introduced as an additional control to fluctuation methods to characterize fluorescent multi-labeling [55] and to determine the states of aggregation of protein in nerve cells [56]. In the following, we explain these studies, which have the same concept as our work, and then we continue by describing our approach to exploit sequential photobleaching to estimate the measured number of molecules and the brightness.

### 3.2.1 State-of-the-art of photobleaching ICS (pICS)

Determining the number of fluorescent labels incorporated into the molecules is important in biological studies, especially for single-molecule measurements and/or to reveal aggregation. Fluorescence data from DNA strands (cDNA) tagged by Alexa was used to determine the number of fluorophore labels per strand by alternating FCS measurement and photobleaching in a series of acquisitions that were carried out in solution [55]. The so-called apparent mean number of molecules, $N_{\mathrm{app}}$ in the observation volume was measured by FCS so to obtain the apparent photon count rate per cDNA strand, $\mathrm{CRM}_{\mathrm{app}} = \mathrm{CR}/N_{\mathrm{app}}$, where CR is the overall count rate. Here, cDNA strands were assumed to have a brightness distribution (i.e., a distribution of the number of labels on strands) that follows a Poisson law, justified by the fact that the Alexa dyes occupy only a small number of available sites on cDNA strands. As a consequence of this assumption, the apparent number of molecules and the count rate per molecule are related to the count rate as

$$N_{app} = N_{tot}\left(\frac{CR}{N_{tot}\varepsilon + CR}\right) \tag{3.4}$$

$$CRM_{app} = \varepsilon\left(1 + \frac{CR}{N_{tot}\varepsilon}\right) \tag{3.5}$$

where $N_{\text{tot}}$ is the total number of strands, and $\varepsilon$ is the count rate per label. Note that the apparent number of molecules, $N_{\text{app}}$, is smaller than the number of strands, $N_{\text{tot}}$, especially because the latter involves all the strands including those that do not bear any label. If the initial count rate is much larger than $N_{tot} \times \varepsilon$, $N_{app} \to N_{tot}$, meaning that all the strands are seen (there are no bare strands). Conversely, when the count rate vanishes, then $N_{app} \to \mathrm{CR}/\varepsilon$, that is, the strands that remain bright are the very few ones that bear only one Alexa label. Correspondingly, at a high count rate, the apparent count rate per molecule $\mathrm{CRM}_{app} \to \mathrm{CR}/N_{tot}$ (all the strands are seen), while at a low count rate, the apparent count rate per molecule $\mathrm{CRM}_{app} \to \varepsilon$, which means that the brightness of the remaining non-dark strands comes from the single label they bear.

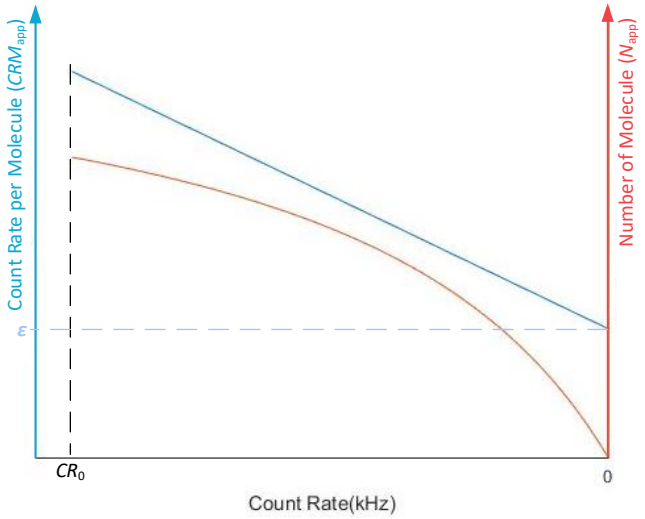


Figure 3.2: ***Theoretical apparent count rate per molecule ($CRM_{app}$, blue line) and apparent number of molecules ($N_{app}$, red line) as a function of the total count rate (CR) during photobleaching.*** *In the case where $CR \gg N_{tot}\varepsilon$, that is when the proteins bear many unbleached dyes (like at the beginning of the photobleaching process), the fluorescence signal is proportional to the apparent brightness of the proteins multiplied by the total number of proteins. At the end of the photobleaching, where the CR approaches zero, the brightness of the proteins $CRM_{app}$ equals to that of a single dye ($\varepsilon$). Knowing the initial count rate ($CR_0$), one can calculate the initial number of dyes ($\bar{n}$).*

An interesting output from this study is that, due to the Poisson distribution assumption, it makes it possible to extract the degree of labeling, $\bar{n}$, (i.e., the initial mean number of fluorophores per strand, including the bare strands, before photobleaching has started), which is given by

$$\bar{n} = \frac{CR_0}{N_{tot}\varepsilon} \tag{3.6}$$

where $CR_0$ is the initial count rate. This approach will also be explored later in Chapter 4 to calculate the surface density of extracellular matrix ligands, where the distribution of initial labels is also assumed to follow a Poisson Law.

In another study, photobleaching has also been adapted to ICS to detect the oligomerization of beta-amyloid (A$\beta$) peptide on nerve cells [7,56]. The principle of this photobleaching-ICS method is that the probability of finding a molecule after photobleaching is related to the degree of aggregation. The authors pointed out that in the homogenous oligomer distribution case, during photobleaching, the measured cluster density decays linearly for monomers (because monomer needs a single step of photobleaching to lose fluorescence) and non-linearly for higher-orders oligomers as a function of the fraction of remaining fluorescence.

To conclude, these previous studies describe the possibility of adding photobleaching to the analysis of ICS. However, up to now the application was thought to be limited to very specific labelling distributions, like Poisson or homogenous oligomer distributions. In the latter case, the authors' conclusion gave the feeling that one can directly determine the oligomerization state from the photobleaching decay regime while, in fact, the only information that can be extracted by analyzing the fluorescence decays is a combination of mean and variance of oligomer distribution, as described in the next section.

### 3.2.2 Photobleaching ICS (pICS) Model

In our approach with pICS, we consider that the system contains a mixture of molecules with an arbitrary distribution of brightness. Like any fluctuation method, pICS also exploits the mean and fluctuations of intensity through the 1st and 2nd moments of the intensity distribution. Here, we develop a model that relates the number of molecules and the brightness as functions of the moments of the number of label distribution prior to the photobleaching decay. We will also see that, unfortunately, it is not possible to disentangle the mean and the variance of the label distribution.

In the case of a single kind of fluorescent entities, the autocorrelation amplitude, $G(0)$, is the inverse of the mean apparent number of molecules (Eq. 3.3). Note that, for sake of simplicity, throughout the rest of the manuscript, we drop the word “apparent” and the corresponding subscript "$_{app}$". When we consider a system consisting of several entities, regardless of the number of entities and their brightness distribution, the autocorrelation amplitude reads as the sum over all fluorescent entities in the system [7].

$$G(0) = \frac{\sum \varepsilon_i^2 N_i}{(\sum \varepsilon_i N_i)^2} \tag{3.7}$$

where $\varepsilon_i$ is the brightness or number of photons counts per entity of the $i$-th species and $N_i$ is the average number of entities of this species in the system.

We then consider a special case where each entity consists of $n$ identical fluorophores, either because they are oligomers composed of identical monomers or because they bear multiple identical labels (Fig. 3.3). We assume that there is no quenching between the fluorophores and that the brightness of a single fluorophore is constant, whatever the number of fluorophores in the assembly. In this case, the brightness of an entity holding $n$ fluorophores (or a $n$-mer) is $n\varepsilon$, where $\varepsilon$ is the brightness of a single fluorophore, with the corresponding number of entities $N_n$. Then, the autocorrelation amplitude is written as

$$G(0) = \frac{\sum n^2 N_n}{(\sum n N_n)^2} \tag{3.8}$$

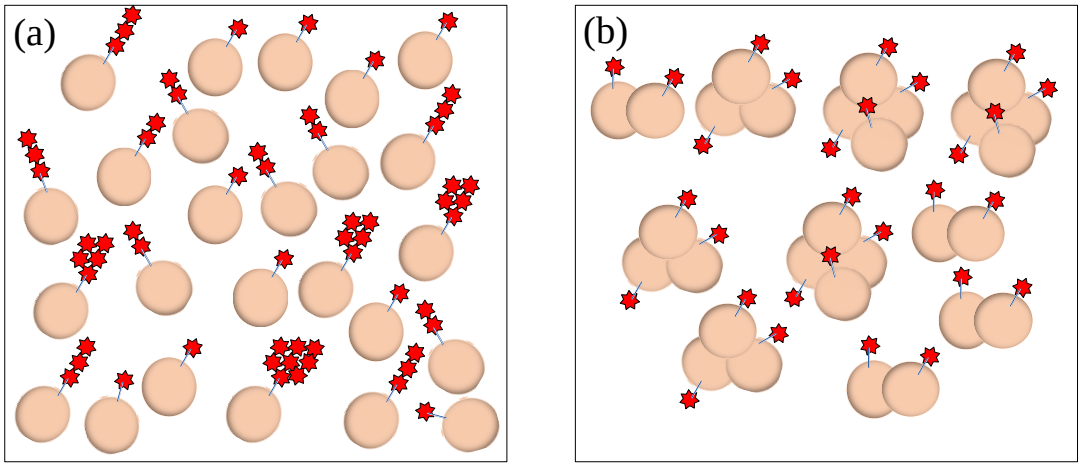


Figure 3.3: ***Systems of interest for pICS method.*** *The pICS method works on systems such as: (a) multiple labelling of identical molecules, and (b) oligomers made of equally bright monomers. In these systems, the fluorophores are identical. Assuming no quenching takes place, the brightness of a single fluorophore, $\varepsilon$, is constant.*

We stress the fact that the underlying assumption is that the fluorophores bore by the molecules or the oligomers are very close to each other, compared to the wavelength. That is, they are colocalized.

To describe the effect of photobleaching, we propose an approach that can be applied to any initial distribution of labels or oligomer size. In the following, we present a derivation similar to that of Ref. [56]. However, we generalize the formalism in order to provide analytical expressions for both the number of molecules and the brightness for any initial distribution of labels or oligomer size.

Since photobleaching is a random process, we assume that at any stage during the experiment, any fluorophore has the same probability not to be bleached, given by *p*. As the fluorescence signal is proportional to the total number of non-bleached fluorophores, this probability is given by $p = \langle F \rangle_t / \langle F \rangle_0$, where $\langle F \rangle_t$ is the fluorescence signal at time *t*, and that

$p = 1$ at time $t = 0$, when photobleaching has not yet occurred. If an entity initially bears *n* fluorophores, the probability $P_{n,p}(k)$ to find *k* non-bleached fluorophores within this ensemble of *n* fluorophores is given by the binomial distribution

$$P_{n,p}(k) = \binom{n}{k} p^k (1-p)^{(n-k)} = \frac{n!}{(n-k)!\,k!} p^k (1-p)^{(n-k)} \tag{3.9}$$

At every photobleaching stage, $p$ is used as a characteristic number, which we will call the *relative fluorescence* for the rest of the manuscript. The autocorrelation amplitude that depends on the relative fluorescence *p* can be written as

$$G_p(0) = \frac{\sum_n M_2(n,p) N_n}{[\sum_n M_1(n,p) N_n]^2} \tag{3.10}$$

the mean number of still bright labels of the species (that initially bore *n* fluorophores) at the relative fluorescence $p$ is given by $M_1(n,p) = \sum k P_{n,p}(k)$, while the mean square of this number would be $M_2(n,p) = \sum k^2 P_{n,p}(k)$. In these expressions, one can identify the first- and second-order moments of a binomial distribution, which are [7].

$$M_1(n,p) = \sum k P_{n,p}(k) = np \tag{3.11}$$

$$M_2(n,p) = \sum k^2 P_{n,p}(k) = np(1-p) + (np)^2 \tag{3.12}$$

After replacing these moments in Eq. 3.10, we obtain

$$G_p(0) = \frac{p^2(\sum_n n^2 N_n) + p(1-p)(\sum_n n N_n)}{p^2(\sum_n n N_n)^2} \tag{3.13}$$

Where the autocorrelation amplitude is now expressed using moments of the initial distribution of fluorophores.

Let us introduce the initial mean number of fluorophores per entity (first-order moment) as $\bar{n} = (\sum n N_n)/N_{tot}$, and the initial second-order moment of the fluorophore distribution as $\overline{n^2} = (\sum n^2 N_n)/N_{tot}$, where $N_{tot} = \sum N_n$ is the total number of entities. Using these notations, the measured number of entities *N* and the measured molecular brightness (or count rate per entity) *CRM* become:

$$N(p) = N_{tot}\frac{\bar{n}p}{\left(\frac{\overline{n^2}}{\bar{n}} - 1\right)p + 1} \tag{3.14}$$

$$CRM(p) = \varepsilon\left[\left(\frac{\overline{n^2}}{\bar{n}} - 1\right)p + 1\right] \tag{3.15}$$

Interestingly, whatever the initial fluorophore distribution is, the measured brightness is an affine function of $p$, of which slope equals $\varepsilon\left(\frac{\overline{n^2}}{\bar{n}} - 1\right)$, and intercept at $p$ = 0 equals the brightness of a single fluorophore, $\varepsilon$. In addition, it can be checked that, according to Eq. (3.15), *CRM* is independent of the number of dark entities in the initial fluorophore distribution. Although the two first moments depend upon this proportion, this is not the case of $\overline{n^2}/\bar{n}$, that is of the measured brightness (that is not sensitive to invisible entities), as expected. Conversely, the measured number of entities, *N*, depends upon the proportion of dark ones, through the first moment, $\bar{n}$.

In the general case of an unknown fluorophore distribution, only the parameters $\varepsilon$, $\overline{n^2}/\bar{n}$, and $N_{tot}\bar{n} = N(p = 1) \times \overline{n^2}/\bar{n}$ can be deduced from using the autocorrelation as a function of photobleaching. This is in contradiction with Ref. [56] that implicitly stated that one could directly obtain the aggregation state by analyzing the decay of the cluster density versus the fraction of fluorescence remaining $p$. As a matter of fact, to get more information than the above-mentioned outputs, one needs additional hypotheses, such as stating that all oligomers have the same size or that the number of fluorophores follows a Poisson distribution.

In the case of Poisson distribution, such as the DNA strand labeling [55], since the Poisson distribution assumption implies $\overline{n^2} = \bar{n} + (\bar{n})^2$, the average initial number of fluorophores per DNA strands, $\bar{n}$, can be deduced from the slope of the brightness.

$$CRM(p) = \varepsilon(\bar{n}p + 1) \tag{3.16}$$

The real number of DNA strands can be extracted from the measured number of strands in order to obtain unbiased concentration measurement.

$$N(p) = N_{tot}\frac{\bar{n}p}{\bar{n}p+1} \tag{3.17}$$

We stress the fact that Eq. 3.16 and 3.17 are equivalent to Eq. 3.5 and 3.4; but derived in a more general framework.

To conclude this section, we showed theoretically that photobleaching can provide some information on the distribution of fluorophores. This information is limited, without other assumptions, only to the parameters $\varepsilon$, $\overline{n^2}/\bar{n}$, and $N_{tot}\bar{n}$. It is also worthwhile to stress the fact that the initial number of molecules (i.e., the one estimated before any bleaching has been applied) can be written (according to Eq. 3.14) as

$$N(1) = N_{tot}\frac{(\bar{n})^2}{\overline{n^2}} = \frac{N_{tot}}{1+\ (\sigma/\bar{n})^2} \tag{3.18}$$

where $\sigma$ is the standard deviation (SD) of the number of labels distribution. Therefore, except in the special case where all the entities initially bear the very same number of fluorophores (SD=0!), $N(1)$ is an underestimation of the true number of molecules. However, this is not a very severe effect. For instance, the Poisson distribution, which is a rather broad one, predicts a factor larger than 2 only if $\bar{n} < 1$.

## 3.3 Material and method

The experiments were carried out on fluorescent nanobeads because they are sufficiently bright to allow visualization of the signals over the noise, even for a low concentration of beads. The measurement of beads at low concentration is important for us as we would like to compare our model to particle counting.

### 3.3.1 Sample Preparation

***Fluorescent Nanobeads***

We used 20 nm red fluorescent polystyrene beads (FluoSpheres® Carboxylate-Modified Microspheres from Invitrogen, Reference F8786) [57]. The manufacturer specifies that variety of dyes are incorporated inside the polystyrene beads and not conjugated on the outside, which will mostly shield the beads from any dye-specific effect regarding charge or hydrophobicity. It is also specified that the beads emit, on average, a fluorescence signal equivalent to the fluorescence of 180 fluorescein molecules. The fluorescent beads are maximally excited at a wavelength of 580 nm and have a fluorescence emission maximum at 605 nm.

The initial number of beads is $5\times10^{15}$ particles/mL. We prepared samples with two different nominal concentrations, which we will refer to as low and high concentrations, respectively, throughout the discussion.

***Beads plating on the glass surface***

The fluorescence nanobeads were immobilized on a glass substrate (Nunc® Lab-Tek® II Chambered Coverglass, surface chamber of 0.7 $cm^2$) covered by poly(l-lysine). To prepare the surface, the chamber was treated with $O_2$ plasma for 40 seconds, then 100 μL of poly(l-lysine) was poured into each chamber to cover the surface and left for 30 minutes. After taking out the poly(l-lysine) and washing the surface, we poured 200 μL of bead solution for each concentration into the chambers and left them in the darkness for 4 hours. After the beads attachment, we washed the surface and replaced the non-attached-beads solution with 200 μL of miliQ water.

### 3.3.2 Experimental procedures

The experiments were performed on a Leica SP8 laser scanning confocal microscope, which is equipped with a DPSS laser at 561 nm and a hybrid detector (HyD) that we used throughout our experiments in photon counting mode. We used a 63×-oil objective (NA 1.4). Series of 20 images of beads on glass surface were recorded with a pixel dwell time of 10 µs, a pixel size of 50 nm, and an image size of 512×512 pixels (25×25 µm). A series of images is necessary to improve the signal-to-noise ratio and to provide statistics on the spatial autocorrelation function. The series of bead images were collected from eleven zones for the low concentration and nine zones for the high concentration on the same substrates. The image acquisitions were carried out with a low laser power (5 µW), in order to mitigate photobleaching during image acquisitions. Between each series of image acquisition, photobleaching was performed by scanning the surface with a higher laser power (500 µW) for 15 seconds. The experimental procedure can be seen in Figure 3.4. After eight sequences of photobleaching, the initial intensity of the image would decrease by up to 90%.

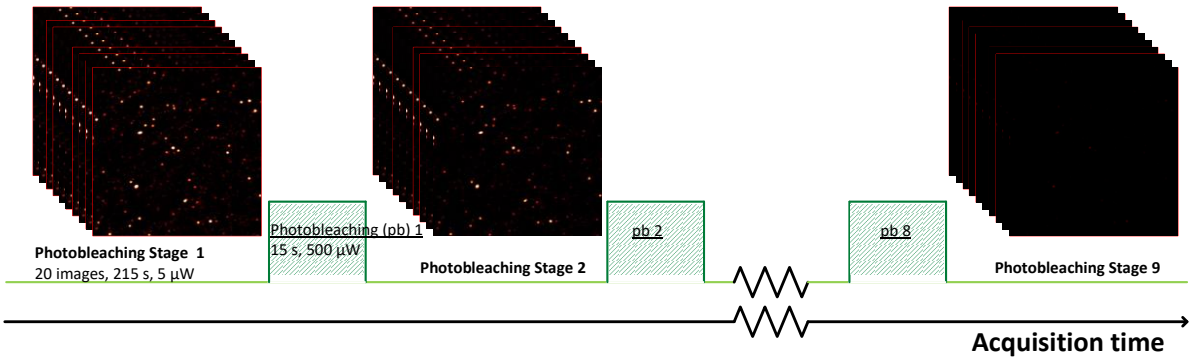


Figure 3.4: ***Image acquisition process***. *The acquisition started at $t = 0$, namely at the first Photobleaching Stage, by sending 561nm-laser of 5 µW for about 215 seconds to record 20 images. Then, the sample is photobleached by increasing the laser power to 500 µW for 15 seconds. The acquisition-photobleaching sequences were repeated and ended at Photobleaching Stage 9 where the initial intensity has reduced to be about 10% of its initial value.*

### 3.3.3 Image processing

***Image Correlation Analysis***

Image analysis for image correlation was performed with custom-made routines (I. Wang, LIPhy) in MATLAB (The MathWorks). The script allows us to automatically perform background subtraction (we will explain about the background in the second time) and image correlation analysis (ICS). Each fluorescence image is first subtracted by the background and then the script calculates the spatial autocorrelation of an individual image. The autocorrelation can be calculated directly using Eq. 3.1., but it is a tiresome process. A more efficient but equivalent way is to calculate the discrete spatial autocorrelation function from the fast Fourier transforms, FFT, which is calculated as the product of the Fourier transform of the original function and its complex conjugate

$$G(x,y) = \mathrm{FFT}^{-1}(\mathrm{FFT}[F(x,y)] \cdot \mathrm{FFT}^{*}[F(x,y)]) \tag{3.19}$$

where $\mathrm{FFT}^{-1}$ is the inverse fast Fourier transform, and the * indicates the complex conjugate operation. In practice, using fast Fourier transforms computer algorithms, Eq. 3.19., is a more rapid approach to calculate the autocorrelation. Then the autocorrelation is averaged over the series of image.

After calculating the spatial autocorrelation function, the fitting is performed with a Gaussian function as in Eq. 3.2. In our script, the fitting parameters ($G(0)$, $\omega_0$, and $G_\infty$) are left free, which in turns are determined with non-linear least square solver. Knowing the value of $G(0)$, we could obtain the average number of fluorescent particles in the observation volume from Eq. 3.3, and the brightness of molecules. The ICS analysis is performed for every image series acquired in each photobleaching stages, i.e., for varying relative fluorescence. The corresponding values are plotted as a function of the relative fluorescence level ($p$) to have a $N$ and $CRM$ graph, and then each of them is plotted with Eq. 3.14 and 3.15 from the pICS model. The fit of $CRM(p)$ function gives the single label brightness $\varepsilon$, which is

the extrapolation at $p$=0 and the statistical parameter $\overline{n^2}/\bar{n}$ that is derived from the slope, while the fit of the $N$ graph gives $N_{tot}\bar{n}$.

***Particle Counting Analysis***

Apart from ICS, we also perform particle counting analysis using a modified MATLAB script [58,59] only on the surface of the low concentration of beads. Firstly, to count the number of particles, $N_{tot}$, we use the images before photobleaching is performed. After the background subtraction, the script determines the intensity of pixels, and then it calculates the cumulative sum (i.e., calculates how many pixels above some value). This allows us to determine a threshold, which is generally set at 1% of the maximum intensity of the pixels in the image (see later for discussion on the influence of the threshold value). Then particle detection is performed by looking for local maxima at a spatial scale given by the PSF dimension. Then the values of these local maxima equal or higher than the threshold are considered as particle while the pixels with weaker gray levels are weed out. Knowing the total number of particles counted at the initial stage, image size (25 μm$^2$), and the size of the PSF, the average number of particles in the confocal volume, $N_{tot}$, can be obtained.

Secondly, the script computes the brightness of every particle, which is obtained by integrating the background-corrected pixel intensities over a disk of 1 μm in diameter around the particle and dividing by $\pi\omega_0^2$, so that it stands for the emission rate of the particle at the maximum of the PSF. Then we obtain the histogram of brightness distribution, which we divide into 100 bins. To extract the value of the average number of fluorophores per particle before photobleaching, we convert this histogram into a histogram of the distribution of the fluorophores by using the value of the brightness of a single particle that we obtain from pICS methods. From the histogram, we can calculate the average number of fluorophores and their second moment.

***Background Subtractions***

Before performing image analysis, it is important to correct the raw images from the background; otherwise, the fluorescence intensity is not properly estimated, and the autocorrelation amplitude is biased. The background may come from scattering and reflection from the glass interface or free fluorophores in solutions that detached from the beads. In our method, we initially generated a mask to cover the beads detected at the initial stage where no photobleaching has been performed yet (Fig. 3.5). On each detected bead, a disk of radius 0.5 μm is created as the mask. Pixel intensities of the area outside the mask, i.e., where the beads are not detected at the initial stage, are then averaged at each stage to provide the background level for a given image. The mask is set using the initial image (non-photobleached) and kept the same for all subsequent photobleaching stages. This background determination was only possible for a low concentration of particles where we could more confidently mask all the particles, and the area used to determine the background was larger.

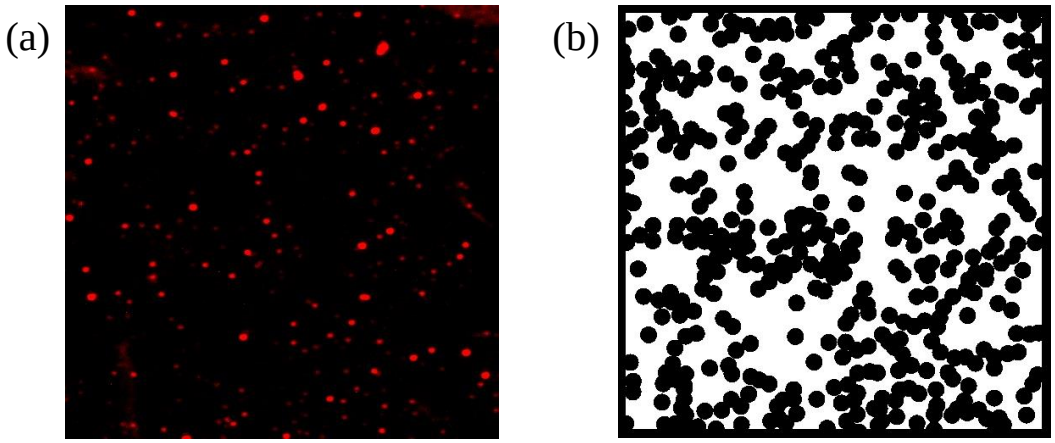


Figure 3.5: ***Beads masking***. *(a) Fluorescence image of beads at low concentration at the initial stage. (b) A 10-pixels (0.5 μm) radius-circular mask (black circles) is generated, and the configuration is maintained throughout the series of photobleaching stages. The white area outside the mask is averaged with exclusion of the intensity from the beads to have a value of the background for each relative fluorescence.*

However, we found that the background signal is not always the same for every zone of measurement. We suspected that the variability of the background from one zone to another was coming from the different intensity of the scattered light due to the roughness or the local tilt of the glass substrate. The standard deviation of the background is 20% of the mean. Nevertheless, the background values remain constant during photobleaching for each zone, suggesting that the background did not photobleach with the relative fluorescence. Hence, we decided to fix the background at one single value obtained as the mean value of all backgrounds from the beads masking method. We then applied this constant background value of 8 kHz for both low and high concentrations. Corrected images were then used to perform ICS and particle counting.

## 3.4 Validating the Photobleaching ICS (pICS) Model

We analyze the images acquired from the photobleaching experiment with beads in two parts. Firstly, we used the full series of photobleaching experiments for validating our pICS model with low and high concentrations of beads solution. Secondly, we applied the particle counting to obtain more information about the beads sample and to check the consistency of our pICS method by comparing its results at low concentrations with those of particle counting at the initial stage. As a matter of fact, in particle counting, it is important to deal with low concentrations to unambiguously detect single particles.

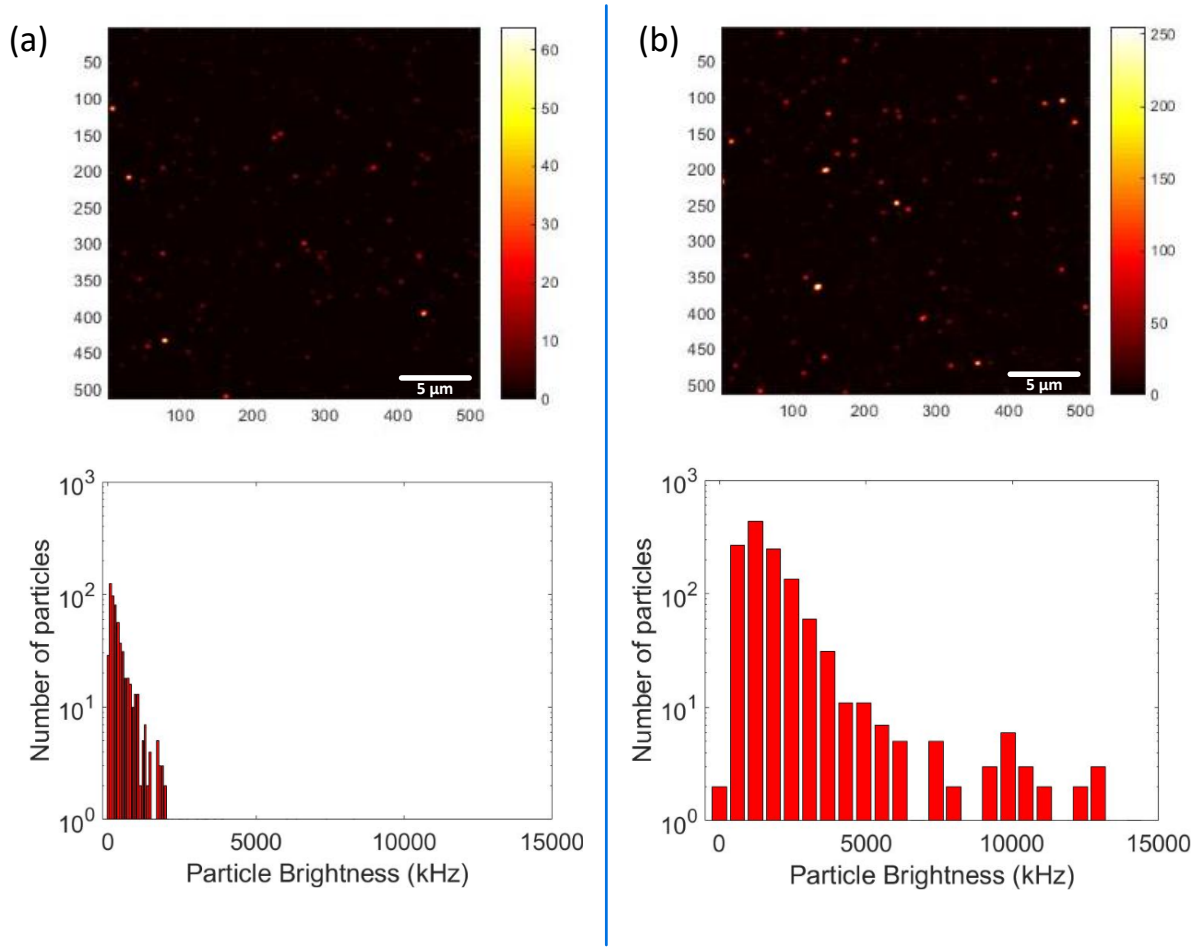


Figure 3.6: ***Fluorescent particles***. *Deposited beads (with images size is 25µm) on the glass surface at two different concentrations of beads suspension: (a) low concentration and (b) high concentration, with their corresponding histogram of particle intensity (from one measurement) in the bottom. The maximum particle intensity is higher for high concentrations. Both histograms display a wide distribution of brightness.*

A typical image of the fluorescent beads is shown in Fig 3.6(a) and (b) for high and low concentrations, respectively. At high concentrations, it is obvious that there are more particles attached to the glass surface and that we have higher particle intensities. When we initially decided to do experiments on beads, we expected that the beads had a very similar brightness. Surprisingly, on each image, we observed that the particle intensities are not homogeneous and that the detected particles exhibit a wide distribution of brightness (see the histogram in Fig. 3.6), which could come from the variation of the number of fluorophores that are incorporated into the beads [57] or aggregates of beads.

The histograms of particle intensity in Fig. 3.6 are derived from a zone where the photobleaching has not yet been performed. The histogram from a high concentration sample shows a larger particle brightness compared to the low concentration sample. The distribution of particle brightness can be due to either the number of fluorophores on the beads or to bead aggregation (in which case, an object seen as a single particle is made of several, non-resolved, beads). This would explain why we observe more bright particles at high concentration. Nevertheless, we used the bead system to test our model introduced in Sec. 3.2.

### 3.4.1 Photobleaching ICS (pICS) model applied on beads

The autocorrelation analysis as the function of the relative fluorescence ($p$) is shown in Fig. 3.7. The values of the number of particles and the count rate per particle decrease as the system is photobleached. Due to the low density of the solution of beads, the estimation of these values in a single zone is prone to errors. The uncertainty of these values comes from different zones (a 25 $\mu m^2$ image) that we used to analyze, and it presents the variability between zones. The variability is prominent when plotting the average of the number of particles where the data are significantly dispersed.

We estimated, for the low concentration, the brightness of a single label $\varepsilon$ to be 58 ± 22 kHz, while for the high concentration, the single label brightness is 53 ± 49 kHz. This consistency indicates that our model is adequate. Although we do not know what fluorophores label the beads, the value of the brightness is in the order of magnitude of the brightness that we obtained with other organic dyes.

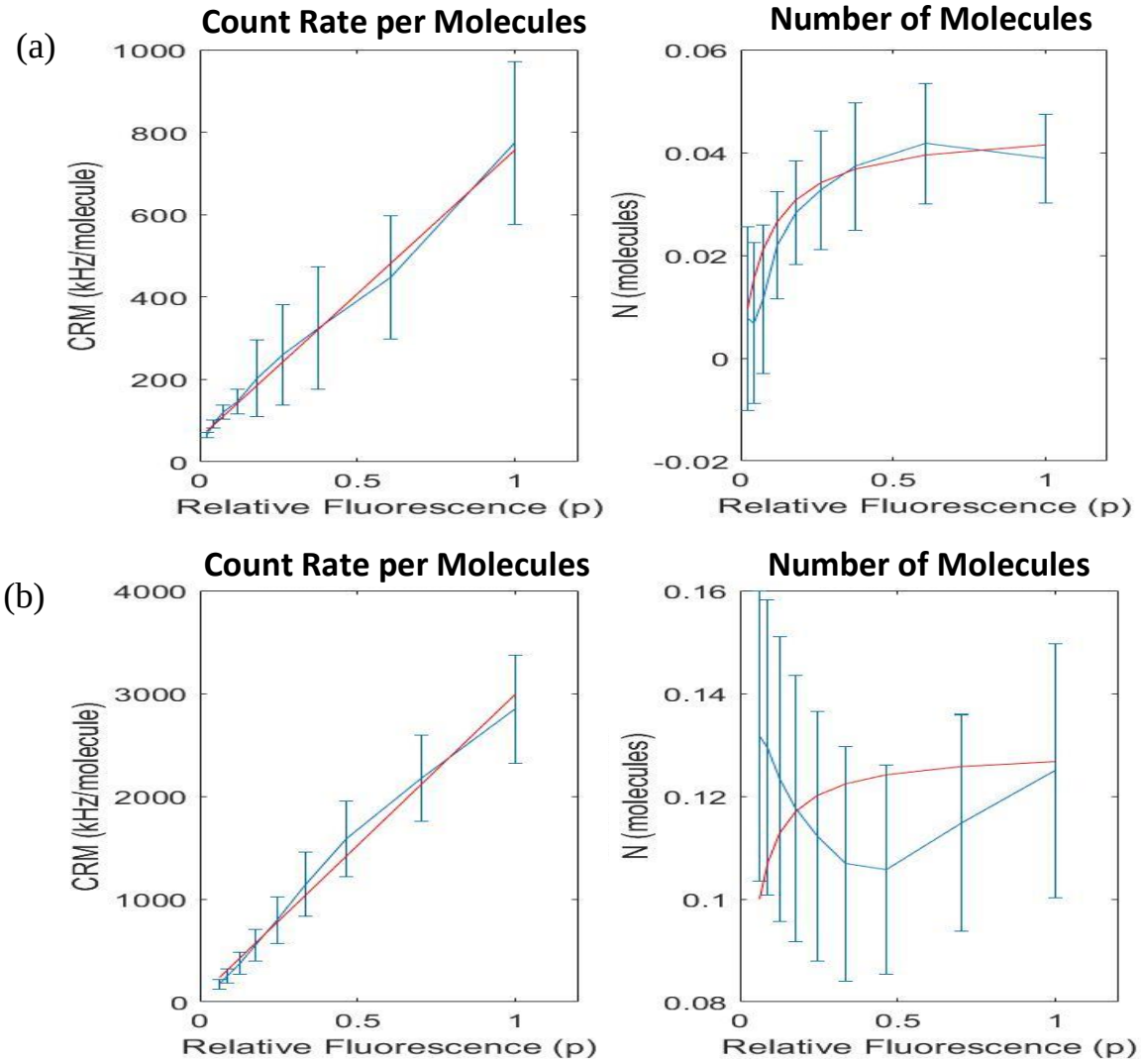


Figure 3.7: ***Count rate per molecule and number of molecules as a function of the relative fluorescence, p.*** *Plotting for: (a) low concentration (calculated from 11 zones), and (b) high concentration (calculated from 9 zones). The number of beads and count rate per beads decrease as a function of the relative fluorescence. The error bars are obtained from the standard error of the mean of all zones for each relative fluorescence.*

On the other hand, the autocorrelation analysis also provides the statistical parameter $\overline{n^2}/\bar{n}$, which is 13 ± 4 for low concentration and 56 ± 49 for high concentration. A higher concentration of the beads favors beads aggregation, thus increasing the number of labels per bead or aggregate, $\bar{n}$. Thus, $\overline{n^2}/\bar{n} = \bar{n} + var(n)/\bar{n}$ would also increase since this ratio is directly related to the variance of the number of labels. Although the difference in $\overline{n^2}/\bar{n}$ between low and high concentration should be mitigated by the large uncertainties, it is not

inconsistent with the fact that aggregates of beads are present at high concentration. In addition to this, we could deduce the parameter $N_{tot} \times \bar{n}$, which is 0.54 ± 0.02 at low concentration and is 7.1 ± 0.1 at high concentration. These values are consistent with the fact that the high concentration (that is, $N_{tot}$) is about ten-fold higher and that it favors aggregation (that is, increases $\bar{n}$). Unfortunately, it is not possible to determine individually $N_{tot}$ and $\bar{n}$.

### 3.4.2 Comparing pICS with the particle counting method

In the particle counting analysis, we used the image before the particles were photobleached and the low concentration only. The total number of particles in the confocal volume that we obtained is $N_{tot} = 0.15$, and the surface density of 0.94 particles/µm$^2$.

On the same images as those we used for particle counting analysis, we could verify that the standard ICS (without photobleaching procedure) gives bias on the estimation of the number of molecules. The amplitude of the autocorrelation in the case of the standard ICS provides the value of the total number of particles as $N_{tot} = 0.04$. This value is about four times smaller than what we obtained with particle counting. This difference comes from the fact that when doing ICS on molecules with a non-unique brightness, i.e., we ignore the distribution of fluorophores on particles, we will underestimate the number of molecules.

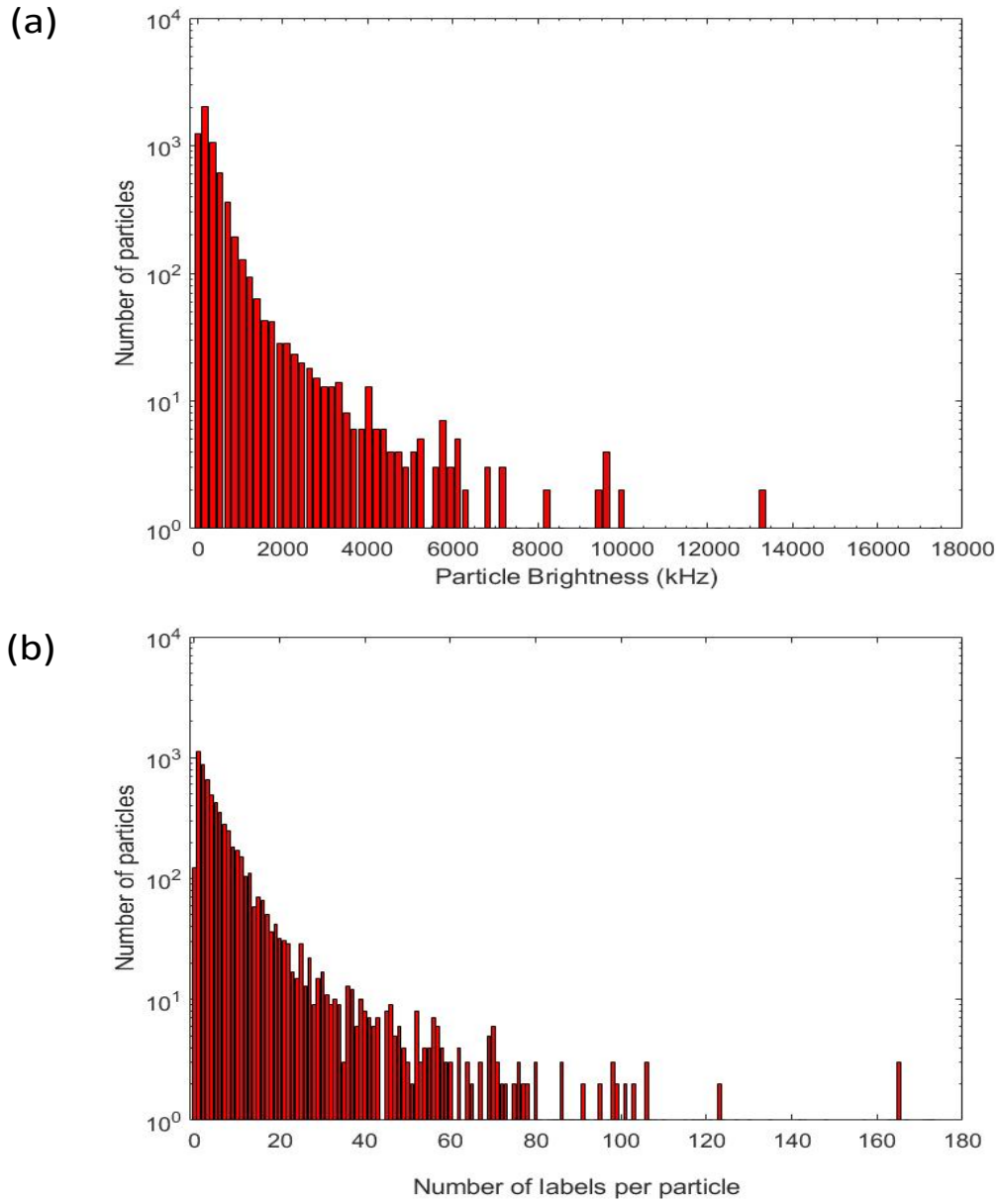


Figure 3.8: ***Histograms of intensity and number of labels distribution.*** *Plotting of (a) the particle intensity for beads at low concentration and, (b) the number of labels which is converted from particle intensity assuming the brightness of a single fluorophore to be 58 kHz. From the histogram of the number of labels at the initial stage, one can determine the initial mean number of labels as* $\bar{n} = 8.4$.

Using histogram from particle counting analysis, we could also compare the parameters of $\overline{n^2}/\bar{n}$ and $N_{tot} \times \bar{n}$ that were obtained with pICS method in Sec.3.4.1. The distribution of particle brightness at low concentration (calculated from eleven zones) at the initial stage (without the photobleaching) is shown in Fig. 3.8(a). The histogram of intensities shows a wide distribution of brightness. From the initial intensity distribution and by

assuming that the particle had the same monomer brightness value as obtained with the pICS, $\varepsilon = 58$ kHz, the particle brightness is converted into the number of labels per particle, since the number of labels per bead can be estimated by using the particle brightness divided by the brightness of one label, as determined with pICS. Figure 3.8(b) shows the distribution of the number of labels per particle. From this histogram, we can obtain the mean number of labels per particle which is $\bar{n} = 8.4$, and also the second moment of the number of labels as $\overline{n^2} = 292$.

Finally, we obtained parameters $\overline{n^2}/\bar{n} = 35$ and $N_{tot} \times \bar{n} = 1.29$ with the particle counting. These values are in the same order of magnitude to those that we obtained from pICS, which are $\overline{n^2}/\bar{n} = 13$ and $N_{tot} \times \bar{n} = 0.54$. The discrepancy of $N_{tot} \times \bar{n}$ between the two methods, however, is not surprising because the number of particles is highly variable from one zone of measurement to another, so that the parameter $N_{tot} \times \bar{n}$ obtained in ICS by averaging values from several zones is prone to large uncertainty. On the other hand, the parameter $\overline{n^2}/\bar{n}$ is related to the distribution of labels, so if the particles that we are considered are the same in both methods, there should be no difference in the value of $\overline{n^2}/\bar{n}$. However, since the particle counting relies on the spatial selection filters, there could be some low-intensity structures ignored by the particle counting, while, on the contrary, every signal contributes to ICS. Hence, that may be why the value of $\overline{n^2}/\bar{n}$ is higher in particle counting.

***Evolution of the Distribution of the Number of Labels During Photobleaching Stages***

From the initial distribution of the number of labels, we can also theoretically predict the distribution of the number of labels per beads for any given relative fluorescence and compare it with the measured distribution assuming a known and constant monomer brightness. Using the initial distribution of the number of labels per particle, we calculated,

for each bins of the number of labels, the subsequent distribution of non-bleached labels as the function of the relative fluorescence, *p*, using Eq. 3.9, then we added them to obtain the whole distribution.

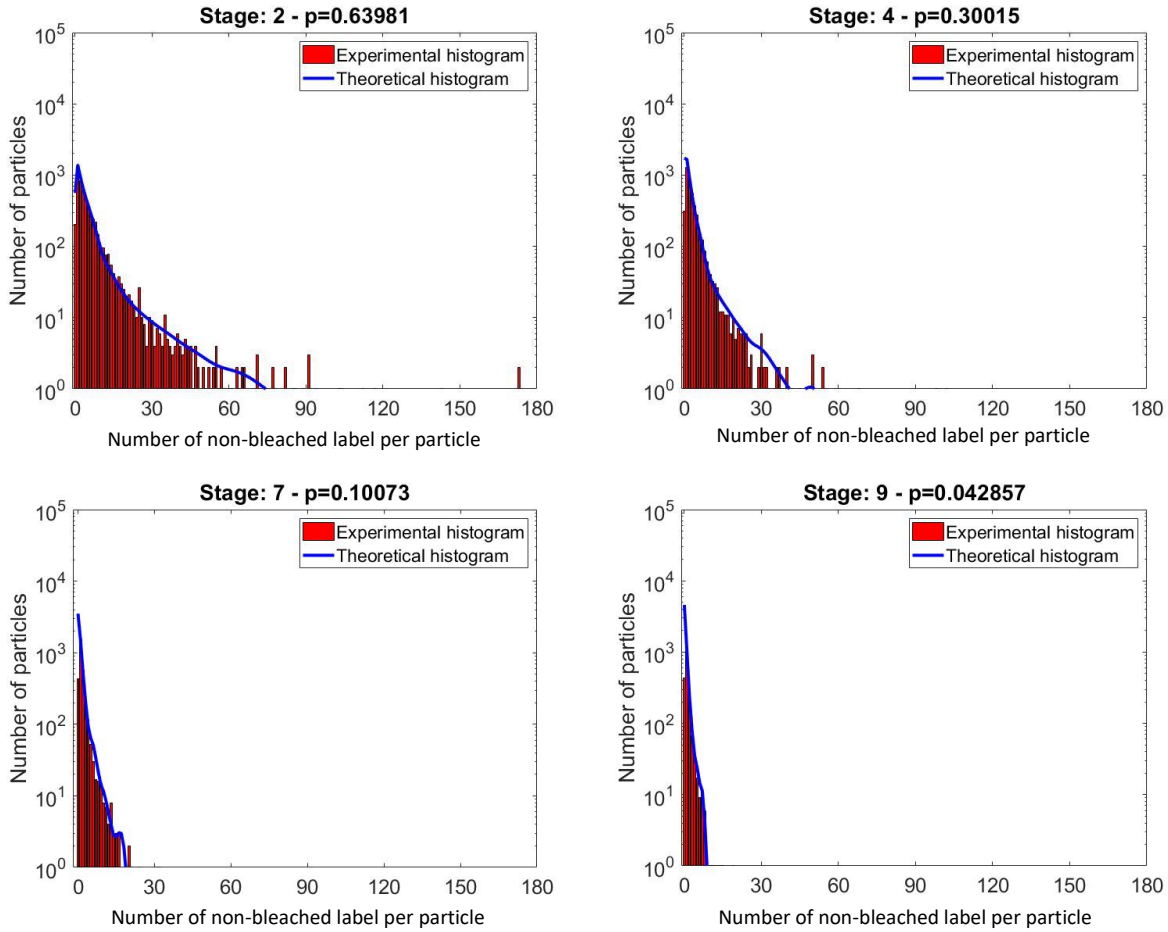


Figure 3.9: ***Experimental histogram evolution during photobleaching compared to the theoretical prediction.*** *The experimental histogram (red bars) for a given relative fluorescence shows that the distribution of the number of labels behaves according to the theoretical histogram prediction (blue line), given the initial distribution.*

The comparison of the distribution that we predicted theoretically (blue line) to the experimental data (red bars) is shown in Fig. 3.9 for some photobleaching stages (stage 2, 4, 7, and 9). Here, we could see that during the photobleaching stages, the histogram changes accordingly to the theoretical model.

### *Impact of Thresholding on Particle Counting*

We would like to investigate the impact of thresholding on the parameters obtained by the particle counting method. We varied the threshold from 0 and 7%. As a reminder, the threshold that we used in the current particle counting analysis (1% of the maximum intensity) corresponds to a situation where we visually perceive that all the beads could be detected. The determination of the threshold was done in the initial image before the photobleaching process.

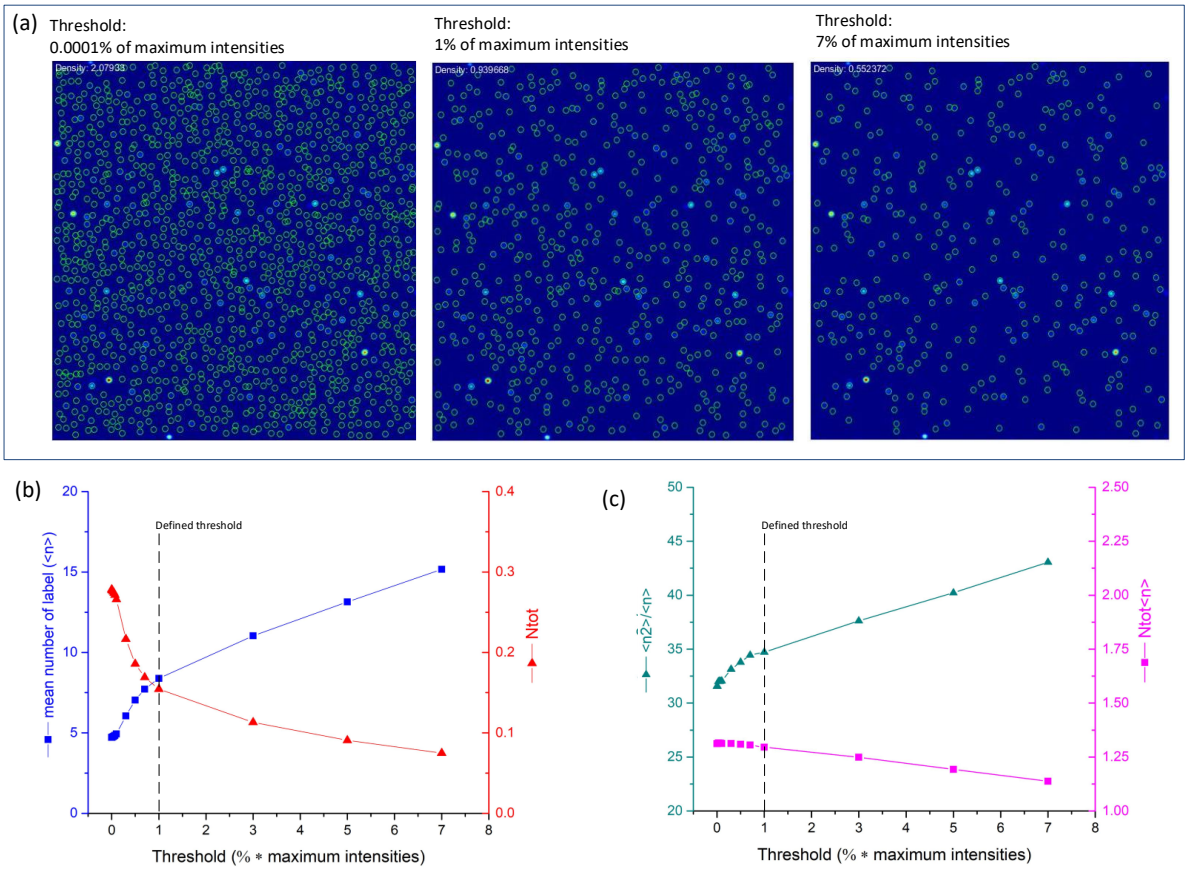


Figure 3.10: ***Effect of threshold in particle counting.*** *(a) Increasing the threshold leads to fewer particles detected in the image. (b) The total number of particles in the observation volume $N_{tot}$ increases (red line) when the threshold decreases, while the mean number of labels $\bar{n}$ decreases (blue line). (c) The statistical parameter $\overline{n^2}/\bar{n}$ also decreases (cyan line) with the decrease of the threshold due to $\bar{n}$, while $N_{tot} \times \bar{n}$ that consist of two parameters that behaves oppositely, increases (magenta line).*

Figure 3.10 shows the effect of the threshold on the counted particles, the value of $\bar{n}$, $\overline{n^2}/\bar{n}$, and $N_{tot}$. When the threshold decreases, there would be more particles counted (Fig.

3.10(a)), thus the number of particles in the detection volume, $N_{tot}$, increases (red triangle, Fig. 3.10(b)). In addition, when decreasing the threshold, since dimmer particles are taken into account, we observe a decreasing number of labels per particle, $\bar{n}$ (blue square) as seen in Fig. 3.10(b). In spite of the observed changes of $N_{tot}$ and $\bar{n}$, the value of $\overline{n^2}/\bar{n}$ (cyan triangle) is not very sensitive to the threshold value, and so is the $N_{tot} \times \bar{n}$ (magenta square) in Fig. 3.10(c) as they depend on two quantities that behave contradictorily to the change of the threshold. Hence, we could say that the threshold is not responsible for the discrepancy of the values of $\overline{n^2}/\bar{n}$ and $N_{tot} \times \bar{n}$ between pICS and particle counting methods.

## 3.5 Conclusion

We have developed a photobleaching Image Correlation Spectroscopy (pICS) method based on the fluctuation techniques. We described a general formalism of relation between the measured brightness (and so the measured number of molecules) and the initial distribution of fluorophores. To validate the model, we did measurements on beads that exhibit a wide distribution of particle brightness. This system is interesting to test our pICS model, while at the same time, we could use it with the particle counting method as an independent way to calculate the surface density.

Performing pICS, we obtained a consistent value of single fluorophore brightness $(\varepsilon)$ between the high and low concentration of the beads solution. We could also derive the value of the statistical parameters of $\overline{n^2}/\bar{n}$ and $N_{tot} \times \bar{n}$. However, in the experiment with beads, we cannot access each quantity individually.

Another limitation of pICS method would be that when performing photobleaching, it may introduce phototoxicity to the system. Meanwhile, with particle counting, we could determine the number of particles in the confocal volume $N_{tot}$ and the number of labels $\bar{n}$,

and the second moment $\overline{n^2}$, which can be compared to the values that were obtained with pICS. However, these values obtained from both methods, although they are close, are not identical. The difference could be due to the fact that, when performing ICS, we consider all pixels, while particle counting disregards signals that are not considered as particles by applying spatial selection filters. So, it is possible that particle counting ignored some smooth structures which, on the contrary, influence the results we obtained with ICS.

In addition to this, using the binomial distribution to describe the evolution of the number of fluorescent labels during photobleaching, we could retrieve a theoretical histogram for every relative fluorescence based on the initial distribution of labels. The experimental distribution of fluorophore evolves with photobleaching accordingly to the theoretical model, confirming the whole framework is consistent.

# Chapter 4

# Assessment of the Surface Density of Ligands with Photobleaching Image Correlation Spectroscopy

Following the model that we described in the previous chapter, we employ this method for a biological application to estimate the number density of molecules. We start this chapter by presenting techniques to quantify the surface-bound molecules. Then we describe the pICS experiment carried out on ligands of extracellular matrix deposited on the glass substrate to deploy our proposed method. We discuss the additional information given by pICS in terms of the degree of labeling. We also describe our preliminary result for another application of pICS, which is performed on fixed cells to understand the state of oligomerization of photoactivable Src kinase. The goal of this chapter is to put into evidence that our method, a combination of Image Correlation Spectroscopy (ICS) and photobleaching, is applicable.

## 4.1 Techniques to Quantify the Molecules on Surface

Surface functionalization is carried out to control the behavior of living material when interacting with surfaces. At the cellular level, surface functionalization plays a role to improve adhesion and enhance the stability of the cell adhesion proteins on the surface. The protein-surface interactions are important to modulate cell adhesion, cell migration,

differentiation, *etc*. Regarding quantification of molecules bound on a surface; Quartz Micro Balance (QCM), ellipsometry, and quantitative fluorescence are well-known techniques.

Working as a mass sensor, QCM is based on the decrease of the frequency of a quartz crystal when biomolecules get adsorbed onto a solid surface [60]. Despite being quantitative and label-free, QCM is less sensitive compared to the fluorescence technique and requires a particular sample deposition technique. On the other hand, ellipsometry is based on the polarization state of a light beam reflected by a surface, which depends upon the thickness and refractive index of the material deposited above the interface [61,62]. Consequently, Ellipsometry makes it possible to assess the amount of deposited material but it requires specific set up.

Finally, quantitative fluorescence can be applied to determine the number of molecules or oligomers by comparing the fluorescent intensity of the molecules to a range of known fluorescence standards [63,64]. However, the main concern of this technique is the limited reliability of the reference used to convert fluorescence intensity directly into absolute molecule numbers when considering several orders of magnitude of protein densities [65]. Photobleaching ICS technique that we exploit, on the other hand, is advantageous because we can directly determine the number of molecules with non-unique brightness, such as the ligands that can bear multiple labels without prior knowledge of the reference brightness.

We are going to apply the approach we presented previously (see Sec. 3.2) to examine the surface density of ligands, trying to assume that the ligands are bearing a number of fluorophores that follow a Poisson distribution. Here, we will see that photobleaching ICS outputs can or cannot be compatible with the manufacturer specifications about the degree of labeling.

## 4.2 Material and Methods

We used ligands deposited on a glass surface. During the completion of this thesis, we performed an experiment on Fibronectin, which is an extracellular matrix ligand that plays a role in processes such as adhesion and migration because these proteins bind to cell surface receptors [6]. Apart from that, we took this opportunity to exploit experimental data on another protein, Fibrinogen, that were acquired prior to this thesis to have a comparable insight on the relation between the surface density and the initial concentration of ligands in solution. Fibrinogen plays an important role in hemostasis, which is the first stage of wound healing by improving clotting function and reducing blood loss [66]. A surface treated with either fibronectin or fibrinogen promotes cell adhesion and migration.

### 4.2.1 Sample preparation

Fibronectin labelled with Rhodamine (FNR01 from Cytoskeleton, with labelling specifications of 1 to 3 dyes per ligand) was reconstituted to obtain a stock solution of 1mg/mL in 20mM Tris-HCl pH 7.6, 20 mM NaCl, 0.1 mM EDTA, 15 mM BME, and 5% (w/v) sucrose. The concentrated ligands were then diluted in pure water solutions of four different concentrations: 0.09, 0.9, and 9 µg/mL. We used an 8-wells Nunc® Lab-Tek® II Chambered Coverglass with a bottom surface of 0.7 $cm^2$ (previously treated with plasma to favor the surface adsorption), into which we poured 300 µl of the ligand solution.

Concerning Alexa Fluor-labelled Fibrinogen (F-13192, Molecular Probes Invitrogen, with labelling specifications of 15 dyes per ligand), the stock solution (1 mg/mL in 0.1 M sodium bicarbonate at pH 8.3, supplemented with 0.1% of 2 M sodium azide) was diluted in HEPES (pH 7.4) into concentrations of 0.2, 0.8, 3.2, and 12.8 µg/mL. The experiments were

performed using 8-wells Nunc® Lab-Tek® I Chambered Coverglass with a bottom surface of 0.8 $cm^2$ and filled with 200 µL of Fibrinogen solution.

In this experiment, the surface treatment was done in the same steps as described in Sec 3.3.1 for beads. The surface adsorption process was set to be 4 hours. However, in this experiment, we did not wash the surface (we kept the ligand solutions throughout the experiments), but we eliminated the influence of the signal from the solution by subtracting it from the signal detected at the surface.

### 4.2.2 Experimental setup and procedure

***Image Acquisition***

The experiments were also performed on the Leica SP8 confocal microscope. We used the laser at 561 nm, a 63×-oil objective (NA 1.4) for the Fibronectin experiment and a 40×-oil objective (NA 1.3) for Fibrinogen ones.

Before acquiring images, the focus was adjusted using a maximum intensity criterion based on the reflection of 561nm-laser on the water-glass interface. The position where we detect maximum intensity indicates that the optical section is exactly at the glass surface. The steps of the experiment on ligands are similar to those done for beads (see Fig. 3.4) with some adjustments on image acquisition settings. Series of 20 images of beads of glass surface were recorded with a pixel size of 50 $nm^2$ and an image size 25 $\mu m^2$ (512×512 pixels), but here we used a pixel dwell time of 5 µs. The acquisitions on Fibronectin samples were carried out with low power of 561 nm-laser (~5 µW) to mitigate photobleaching for about 100 seconds. Images of Fibrinogen on the surface were also acquired with similar laser powers (0.5–5 µW). Between each series of image acquisition, photobleaching was performed by increasing the laser power to 50 µW for Fibronectin and 80 µW for Fibrinogen for 60 seconds until the

average intensity decreases to 10% of its initial value, which was attained after 6 photobleaching stages.

***Background Images***

To estimate the background signal due to molecules in solution, a series of 20 images was recorded at 50 µm above the surface (in the solution) with the same parameters as those of the acquisition sequence. However, during the experiments with Fibronectin, we found that the signal coming from the reflection of the glass was not negligible compared to the fluorescence signal of Fibronectin in solution. Hence, we collected the signal at a pure water-glass interface and added it to the signal in solution to have the total background signal.

### 4.2.3 Image analysis

The analysis of the fluorescence image of ligands on the surface was performed with the same method as described in Chapter 3 for pICS. However, in this analysis, we used a plugin with ImageJ that has been developed by A. Delon and A. Fertin (TIMC, Grenoble) to perform pICS. Here, the images are divided into 8 × 8 sub-regions of 3 µm$^2$ to provide, thanks to this sampling, a mean value, and a SEM (standard error of the mean) of the brightness. The SEM of the brightness is then used as vertical error bars for the $CRM(p)$ points, while the horizontal error bars (corresponding to the count rate) are negligible. In some cases, different image sets from the same sample preparation, with their respective output distributions and uncertainties were gathered before fitting. In the analysis, as we work with ligands assumed to have a Poissonian distribution of fluorophore, the data points $CRM(p)$ are fit with Eq. 3.16.

## 4.3 Background Signal and Non-uniformity Influence in Image Correlation Spectroscopy (ICS)

It is important in Image Correlation Spectroscopy (ICS) to correct the raw images from the background due to the presence of parasitic signals: the fluorescence of surrounding molecules in solution or the light scattered by the glass interface. Otherwise, it would bias the analysis since this signal will contribute to the detected intensity and not to the fluctuations (here, we assume that the parasitic fluctuations are either averaged out in case of parasitic molecules diffusing in solution or absent in case of light scattering). In other words, it makes the amplitude of the normalized autocorrelation function lower, thus overestimating the number of molecules. Figure 4.1(a) and (b) show an example of the effect of background subtraction on fluorescence images of Fibronectin on the surface where we can see the effect on the estimation of the number of molecules.

It is important in Image Correlation Spectroscopy (ICS) to correct the raw images from the background due to the presence of parasitic signals: the fluorescence of surrounding molecules in solution or the light scattered by the glass interface. Otherwise, it would bias the analysis since this signal will contribute to the detected intensity and not to the fluctuations (here, we assume that the parasitic fluctuations are either averaged out in case of parasitic molecules diffusing in solution or absent in case of light scattering). In other words, it makes the amplitude of the normalized autocorrelation function lower, thus overestimating the number of molecules. Figure 4.1(a) and (b) show an example of the effect of background subtraction on fluorescence images of Fibronectin on the surface where we can see the effect on the estimation of the number of molecules.

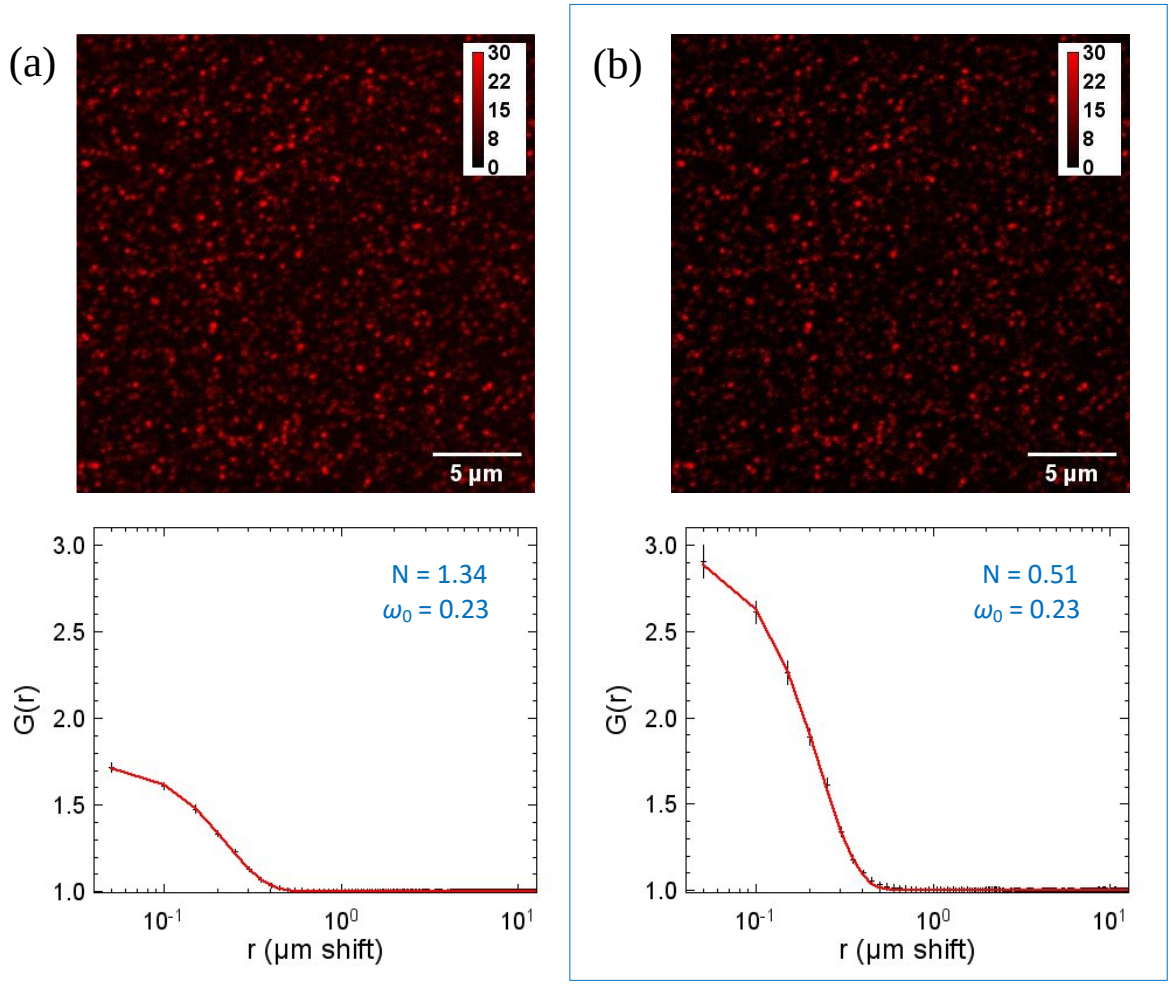


Figure 4.1: ***Effect of image correction on autocorrelation***. *The images are projected from the average intensity of 20 images with a 0.09* µg/mL *solution concentration: (a) raw images without background subtraction, (b) after background subtraction and the corresponding mean autocorrelation (black cross) and its fit (red line),*

Another issue that should be addressed with ICS is the non-uniformity of images mostly coming from the spatial variation of the surface density or of the brightness (plus, but unlikely to occur, from inhomogeneous laser illumination or fluorescence collection). As a result, the autocorrelation function cannot be fitted properly. This situation can be corrected by applying a flattening where each background-corrected image is divided by its own smoothed version [67]. The smoothed image is obtained by convoluting the raw images with a 2D Gaussian function. The width of this Gaussian must be much larger than the width of the PSF (the half-width at 1/e typically ranges from 0.2 to 0.3 µm) to maintain the statistical

fluctuations of interest, but small enough to be sensitive to the inhomogeneities that need to be removed. We used a tradeoff of 2 µm for the half-width at 1/e of the Gaussian function to smooth and flatten the images. As shown in Figure 4.2, the flattening procedure allows for correcting the shape of the autocorrelation function. The fitting of this corrected function gave the expected waist value, and therefore rectifies the estimation of the number of molecules.

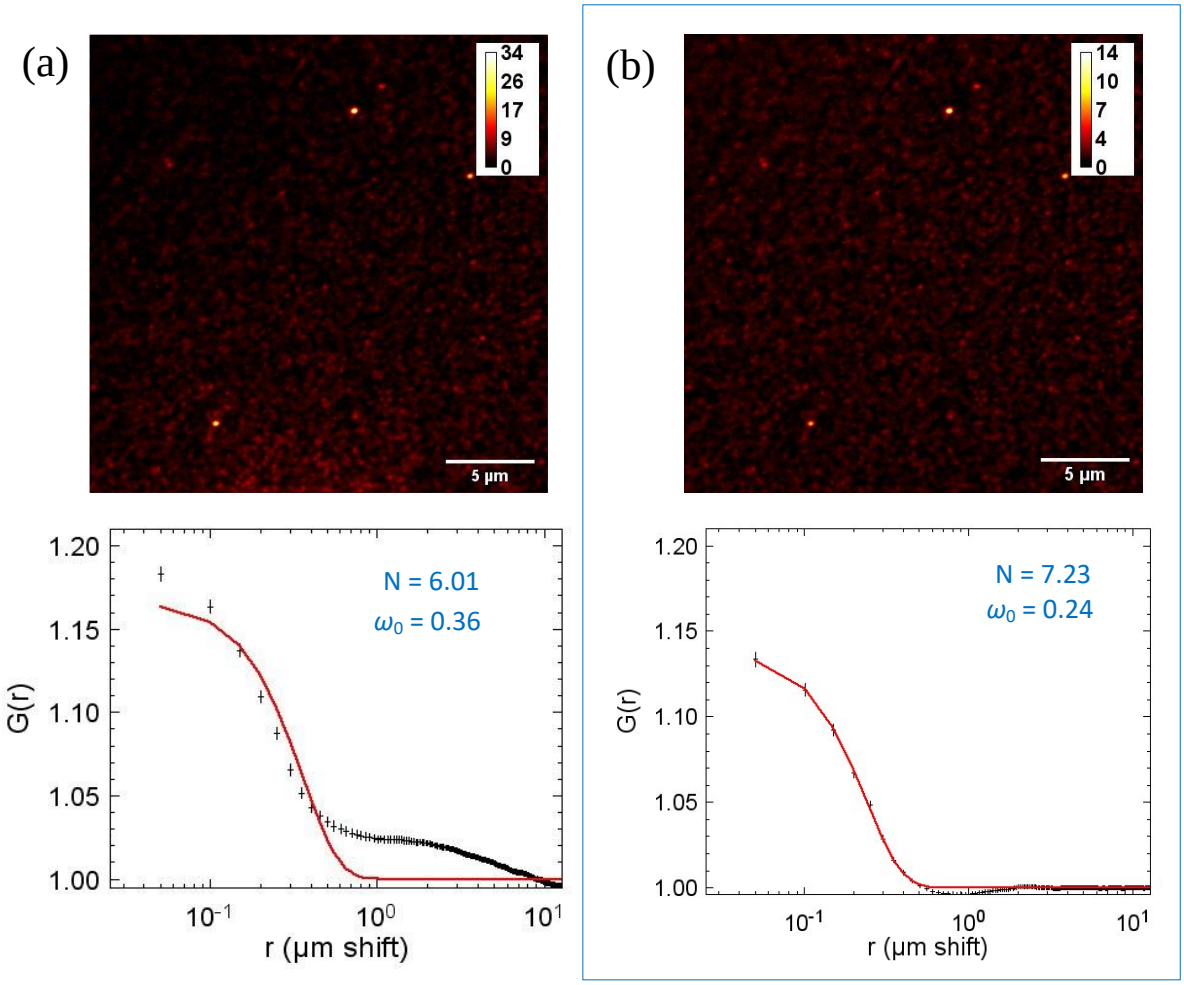


Figure 4.2: ***Effect of image flattening on autocorrelation***. *The images are projected from the average intensity of 20 images of Fibronectin with a 0.9* µg/mL *solution concentration: (a) raw images without background subtraction, (b) after image flattening, and the corresponding mean autocorrelation (black cross) and its fit (red line),*

However, we perceived that at a low concentration of protein in solution (as in the cases of Fibronectin under 0.9 µg/mL), it is not necessary to perform the flattening procedure on the image. At low concentration, there are few numbers of molecules in the image so that it is

difficult to smooth the intensity. For image analysis, we always first subtract the background, and the flattening procedure is only applied as necessary so as not to introduce another artifact to the images.

## 4.4 Results and Discussion

Varying the nominal concentration of the ligand solution would provide different ligand densities on the surface. To be noticed, the surface is not covered by the total number of ligands diluted in solution because not all ligand binds irreversibly to the glass.

### 4.4.1 Fibronectin samples

Figure 4.3(a) shows an example of the count rate per molecule $(CRM)$ versus the relative fluorescence, *p*, for a surface-deposited Fibronectin at a nominal concentration of 0.09 µg/mL. The brightness of molecules clearly decreases linearly with the count rate. Using Eq. 3.16 to fit the experimental data, we found the brightness of a single fluorophore to be $\varepsilon = 20.8 \pm 0.7\ (SD)$ kHz, a mean number of Rhodamine dyes per Fibronectin $\bar{n} = 1.47 \pm 0.10\ (SD)$, which is close to the labeling specification of the manufacturer $(\bar{n} = 2)$, from which we deduce a total number of molecules $N_{tot} = 0.95 \pm 0.09\ (SD)$. Note that the $p = 1$ point (corresponding to about $CR1 = 29$ kHz and $CRM1 = 52$ kHz/molecule) leads to 0.6 molecules.

Figure 4.3(b) shows the pICS data of the 0.09 µg/mL of Fibronectin concentration, which the outputs are very consistent with those of the 0.09 µg/mL case: $\varepsilon = 20.3 \pm 0.4\ (SD)$, $\bar{n} = 1.81 \pm 0.08\ (SD)$ leading to $N_{tot} = 11.6 \pm 0.8\ (SD)$. If we look at the point $p = 1$, of which the value of $CR1 = 431$ kHz and $CRM1 = 60$ kHz/molecule, it gives 7.2 molecules. In addition to this, the ratio of the estimated total number of molecules $(N_{tot})$ for

the 0.9 and 0.09 µg/mL (11.6/0.95) is close to the ratio of 10 between these nominal concentrations.

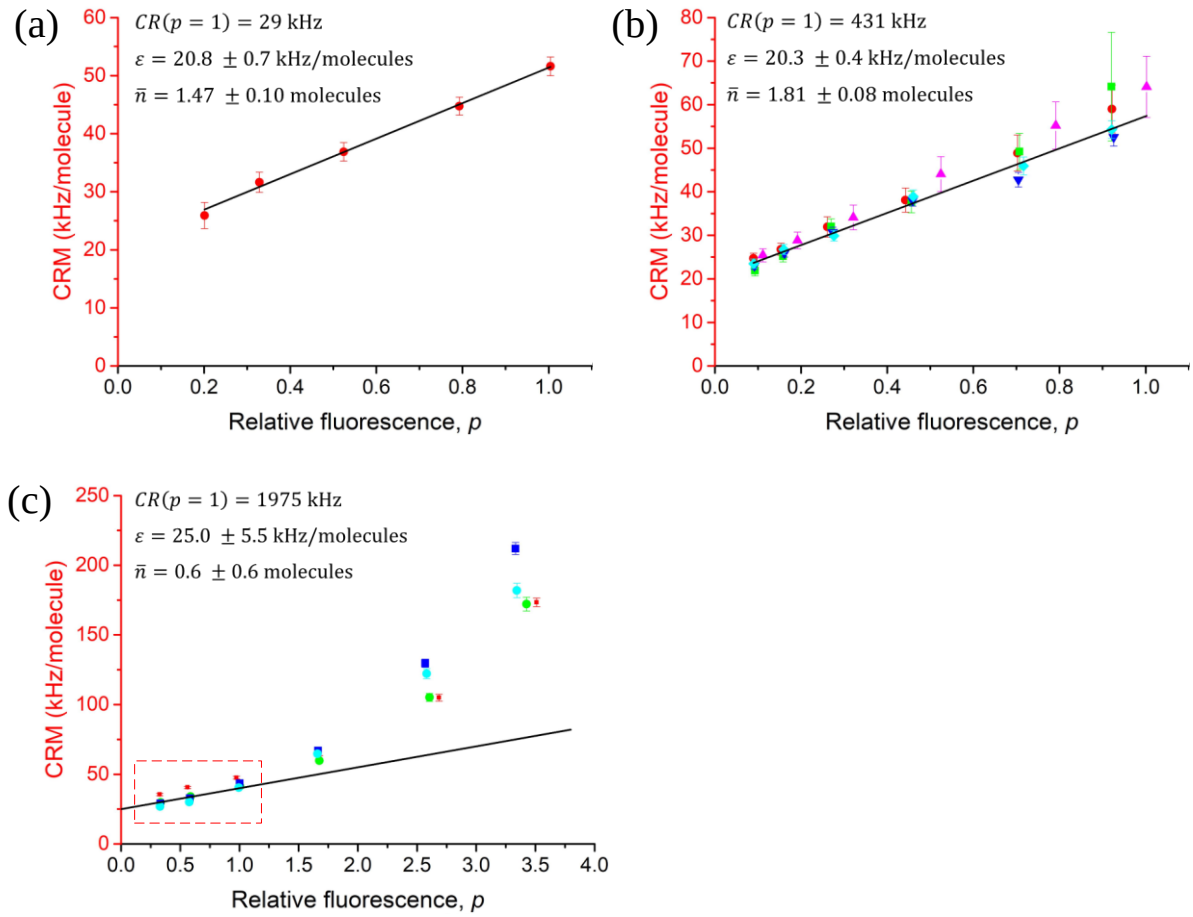


Figure 4.3: ***Count rate per molecule as a function of the relative fluorescence, p, of Fibronectin samples.*** *The measurement was performed with six series of acquisitions with sequential photobleaching with 50 µW irradiation. The count rates per molecule are fit with Eq 3.16. (a) Fibronectin sample with concentration of 0.09 µg/mL where the last point was not taken into account. (b) Fibronectin sample of 0.9 µg/mL with 5 zones of measurement indicated by different color of data points. (c) Fibronectin sample of 9 µg/mL with 4 zones of measurement where the fit was performed over the three lowest points (red dash-rectangle).*

We also performed pICS experiments on the 9 mg/mL case, but unfortunately, we could not make use of it, as the $CRM(p)$ data points show an unexpected non-linear decay as can be seen in Fig. 4.3(c). Since different zones of measurement shows the same behavior, we believe that there is no problem of defocusing during acquisitions. Although the last part of the decay curve can be fit (indicated by the red dashed rectangle), leading to a consistent value of the single fluorophore brightness (ε = 25.0 ± 5.5 kHz/molecule), we cannot infer any

value for the total number of molecules, since they have been bleached by an unknown amount. Nevertheless, we observe that the estimated mean number of fluorophores (≅ 0.6), smaller than the values found for the 0.9 and 0.09 µg/mL of Fibronectin concentrations, is not inconsistent with the fact that the molecules have lost dyes during the beginning of the photobleaching decay.

### 4.4.2 Fibrinogen samples

In the case of Fibrinogen, the data that we acquired raises more problems than the Fibronectin ones. Firstly, the measurements with 0.8 µg/mL concentration (data are not shown here) cannot be exploited due to data points of the photobleaching series that cannot be fit.

Secondly, although we observed consistencies of the single fluorophore brightness in the measurements of the 0.2, 3.2, and 12.8 µg/mL Fibrinogen concentrations, we obtained inconsistencies of the mean number of fluorophores with the manufacturer's specifications. Figure 4.4. shows the fit of the data with Eq. 3.16 and their outputs for the Fibrinogen samples. For these measurements, we used different laser power to acquire images, which are 5, 2.5, and 0.5 µW for the 0.2, 3.2, and 12.8 µg/mL concentrations, respectively. The single fluorophore brightness resulted from the fit, $CR(p = 1)$, are 69.3, 56.3, and 8.8 kHz for the Fibrinogen concentrations of 0.2, 3.2, and 12.8 µg/mL, respectively. If we normalize the single fluorophore brightness to mimic a laser power of 0.5 µW, we obtain a single fluorophore brightness of 6.9 and 11.3 kHz/molecules for the 0.2 and 3.2 µg/mL concentrations, respectively, which is more or less consistent with the value of 8.8 kHz/molecule obtained for the 12.8 µg/mL concentration.

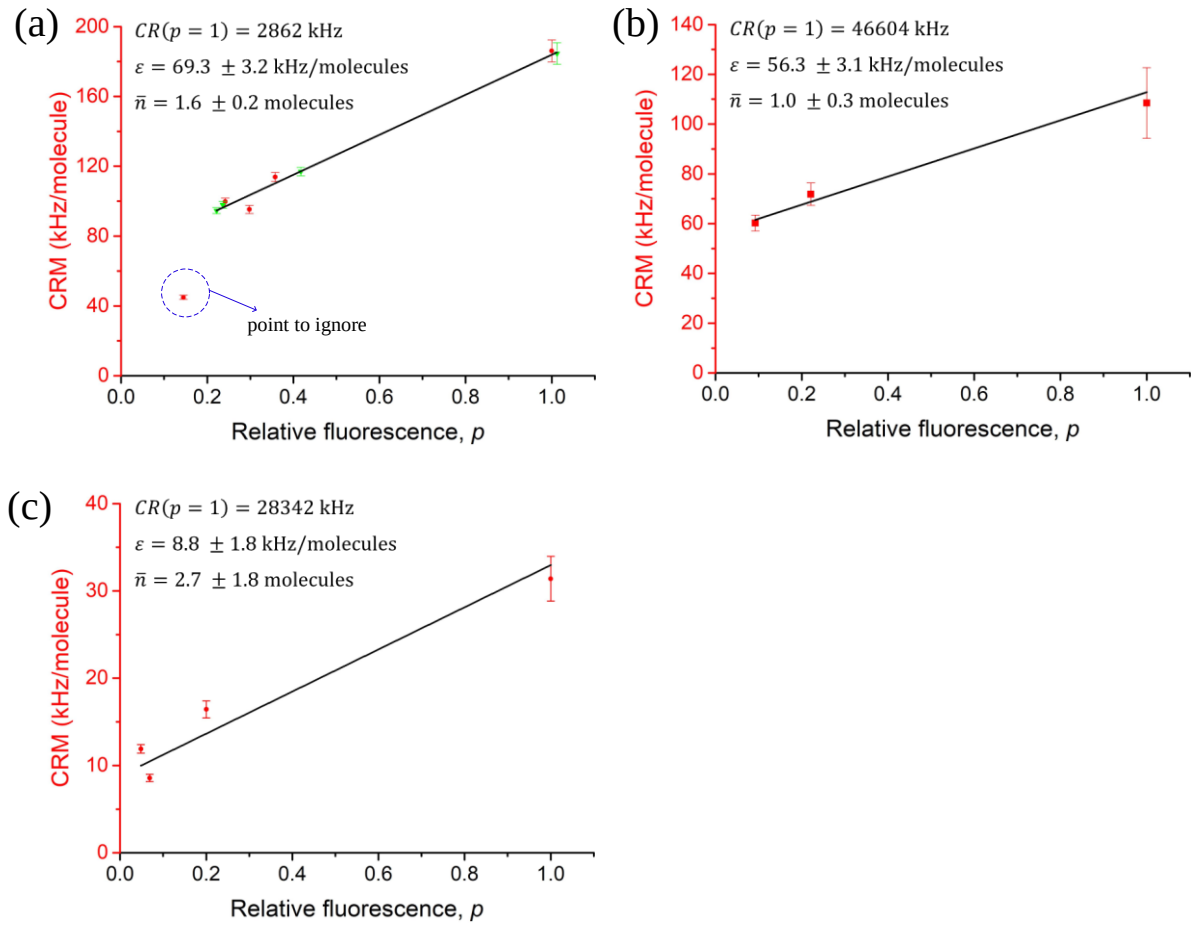


Figure 4.4: ***Count rate per molecule as a function of the relative fluorescence, p, of Fibrinogen samples.*** *(a) Fibrinogen samples at 0.2 µg/mL nominal concentration, where the last point was taken out (blue dash-circle). (b) Fibrinogen sample of 3.2 µg/mL. (c) Fibrinogen sample of 12.8 µg/mL. The count rates per molecule are fit with Eq 3.16.*

However, the range of the estimated mean number of dyes per Fibrinogen, $\bar{n} = 1{\sim}3$ is fully inconsistent with the manufacturer specification of 15 dyes per molecule [68] (we cared not to bleach the molecule before running the experiment). We then wondered if the Poissonian hypothesis could be lifted to interpret the data again. In the general case, the slope of the decay divided by $\varepsilon$ (see Eq. 3.15) equals $\frac{\overline{n^2}}{\bar{n}} - 1$ that can be written again as $\frac{\sigma^2}{\bar{n}} + \bar{n} - 1$. It immediately follows from the range of slope values (1~3) that $\bar{n}$ cannot be set to 15, as this would lead to a negative variance $\sigma^2$. To conclude, the Fibrinogen data show definitive inconsistencies that we could not interpret and exclude any reliable areal density measurements.

### 4.4.3 Perturbance of "fresh" molecules in the observations volume

In relation to aggregates, which are likely to be present in solutions of high concentration, one should be careful as it could affect the estimation of the number of molecules. We now consider the case of Laminin, another ligand of the extracellular matrix. The data were recorded before this thesis and was excluded from the discussion of the above-mentioned pICS analysis due to the exchange of molecules and aggregates on the glass surface during image acquisition. This perturbance only occurred at a high concentration of Laminin.

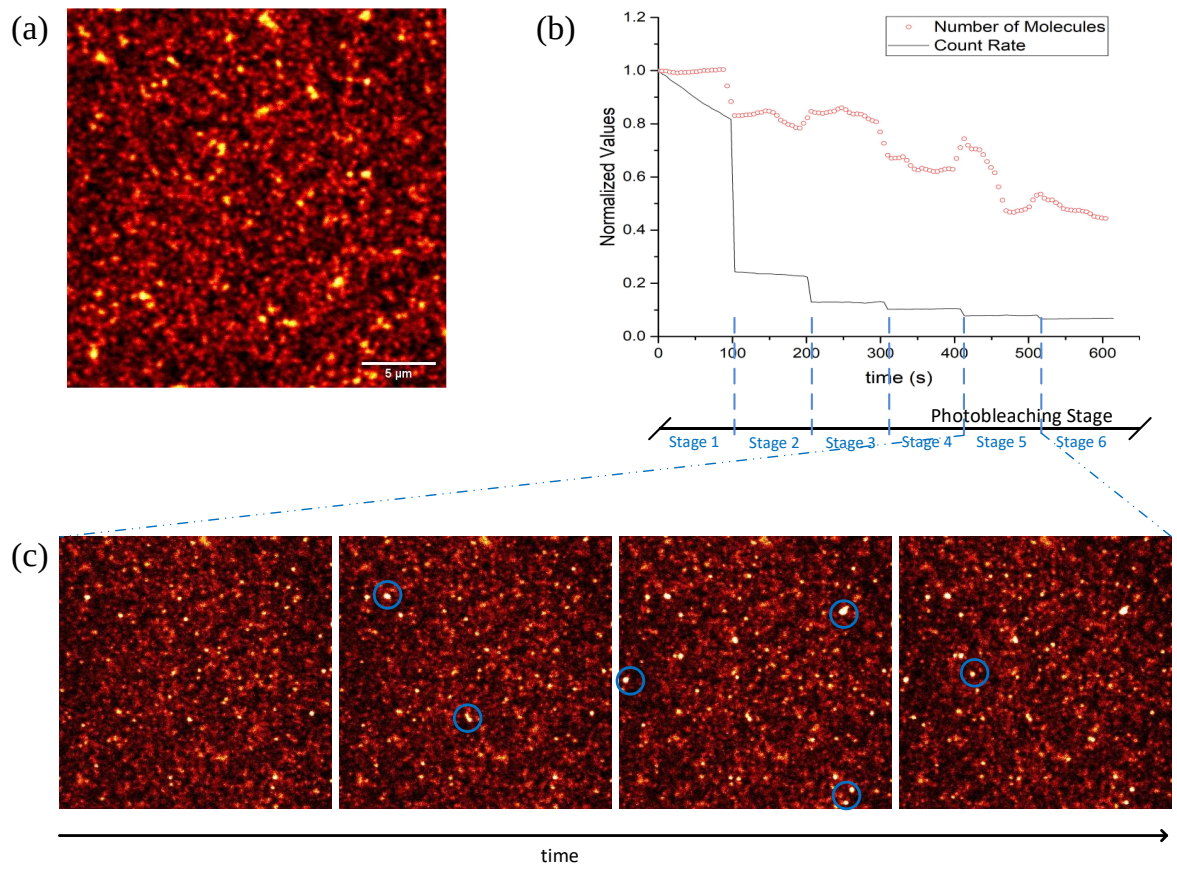


Figure 4.5: ***Surface-adsorbed molecules of Laminin.*** *(a) Fluorescence image of Laminin at initial stage. (b) A drift-time analysis of Laminin over six photobleaching stages. (c) Images of molecules on the surface at photobleaching stage 5, with blue circles showing some examples of the appearance of aggregates or fresh molecules.*

Figure 4.5 shows the effect of fresh molecules or aggregates perturbance on the estimation of the number of molecules of Laminin at a nominal concentration of 4 µg/mL. At the initial stage $(t = 0)$, the fluorescence image of Laminin shows bright structures over the glass surface (Fig. 4.5(a)). The incoming aggregates or fluorescent molecules from the solution cause the number of molecules to change. Depending on the rate of exchange of the aggregates (whether they were recorded or not (Fig. 4.5(c)), the calculation of the number of molecules determined could or could not include the signal from the aggregates, giving a fluctuating number of molecules over time (Fig. 4.5(b)). In this case, we cannot use this data to measure the surface density because there was a lot of exchange of molecules between solutions and the surface that dominate the signals.

## 4.5 Conclusion

In the case of ligands bearing multiple fluorophores as Fibronectin and Fibrinogen, combining the standard Image Correlation Spectroscopy with photobleaching (pICS) might be applicable.

We observed that the number of molecules of Fibronectin, $N_{tot}$, is roughly proportional to the nominal concentration for 0.9 and 0.09 µg/mL. In addition to that, we also obtained an estimation of the average initial number of Rhodamine dyes in Fibronectin, which is not inconsistent with the manufacturer specifications. On the contrary, the estimated mean initial number of Alexa dyes in Fibrinogen has been found to be highly questionable since it is dramatically inconsistent with the specified degree of labeling. We thus decided not to infer the total number of molecules for Fibrinogen.

## 4.6 Prospect: Quantifying Oligomerization in Cells

Oligomerization is a common question in biology. The photobleaching ICS (pICS) method that we have described has a potential to quantify oligomerization. We attempt to apply pICS into biological cells by using an optogenetic system. Throughout this manuscript, we worked with two types of optogenetics cells since the optogenetic tools are very promising in biology, but detailed characterization of these system is still lacking. Firstly, we performed photobleaching Image Correlation Spectroscopy (pICS) on system of optoSrc to observe the state of oligomerization of protein, which we will elaborate in this section. Secondly, we deployed another fluctuation method, which is Raster Image Correlation Spectroscopy (RICS), on optogenetics system of CRY2/CIBN to study the proteins localization, which will be discussed later in Chapter 5 of the manuscript.

Protein oligomeric states can drive different cellular functions. However, a quantitative characterization of the protein oligomeric states is quite difficult. Our technique of pICS can be employed to understand the state of oligomerization in cells. The advantage is that pICS does not need to refer to the calibration measurement to determine the size of an oligomer. To do so, we have begun a work using an optogenetics system called optoSrc. Src is a non-receptor protein tyrosine kinase that transduces signals that are involved in cellular processes such as adhesion [69]. The proto-oncogene c-Src is not only present in monomeric form in the cytosol, but it is also found inside the focal adhesion and the plasma membrane in the oligomeric form [70], which will be a good system to apply our model.

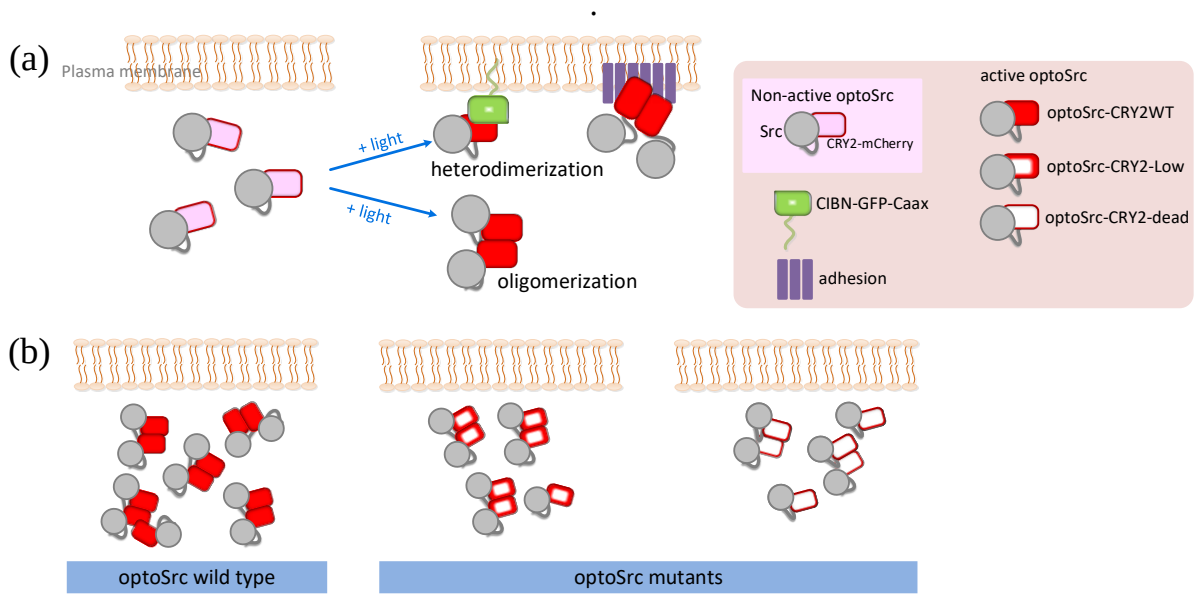


Figure 4.6: ***OptoSrc-CRY2.*** *(a) Optogenetics system of Src, optoSrc, is activable upon light activation, which then induces either CRY2 heterodimerization with a CIBN anchored at the plasma membrane or CRY2 homo-oligomerization that triggers its relocalization in adhesion sites. (b) Mutation of the optoSrc reduced CRY2 capacity to form oligomers under light stimulation. Adapted from* [70].

Optogenetics refers to the use of the combination of optics and genetics methods for controlling the activity of light-sensitive proteins by triggering, for example, relocalization, oligomerization, or interaction. Cellular specificity, spatiotemporal capabilities, and reversibility are distinctive aspects of optogenetics that trigger its development. However, it is necessary to quantitatively measure the activity occurring in optogenetics tools due to photoactivation, which can be done, among other techniques, with the fluctuations methods. The basic principle of optogenetics systems is the following: when exposed to light, the photosensitive proteins undergo a conformational change that promotes the association of the protein onto its effector [71].

The optogenetics system optoSrc is designed by fusing light sensitive CRY2 into Src structure. This system is capable of forming oligomers and/or relocalizing to the adhesive sites in dimeric form upon light activation (Fig. 4.6(a)). OptoSrc-CRY2 is initially cytoplasmic and labeled with mCherry that absorbs light between 540-590 nm and emits light

in the range of 550–650 nm. The cells, which were prepared by our collaborator O. Destaing (IAB, Institute for Advanced Biosciences), include a wild type optoSrc-CRY2WT and two mutants: optoSrc-CRY2-dead and optoSrc-Cry2-Low. The mutations that have been carried on optoSrc should decrease its propensity to oligomerize (Fig. 4.6(b)). We would like to see the size of oligomers of different mutants of cytosolic optoSrc. In this section, we will present the preliminary results of oligomerization quantification in activatedoptoSrc-CRY2 in MDCK fixed cells that we obtained from only a one-day experiment.

The experiments were performed on an SP8 Leica confocal system. Series of 10 images of the mutants were recorded with a pixel dwell time of 1.2 μs, a pixel size of 50 nm, and an image size of 512×512 pixels. The image acquisitions were carried out with 488nm-laser to locate the membrane and 561nm-laser to image mCherry, and the sequential photobleaching was done with 561nm-laser with high power.

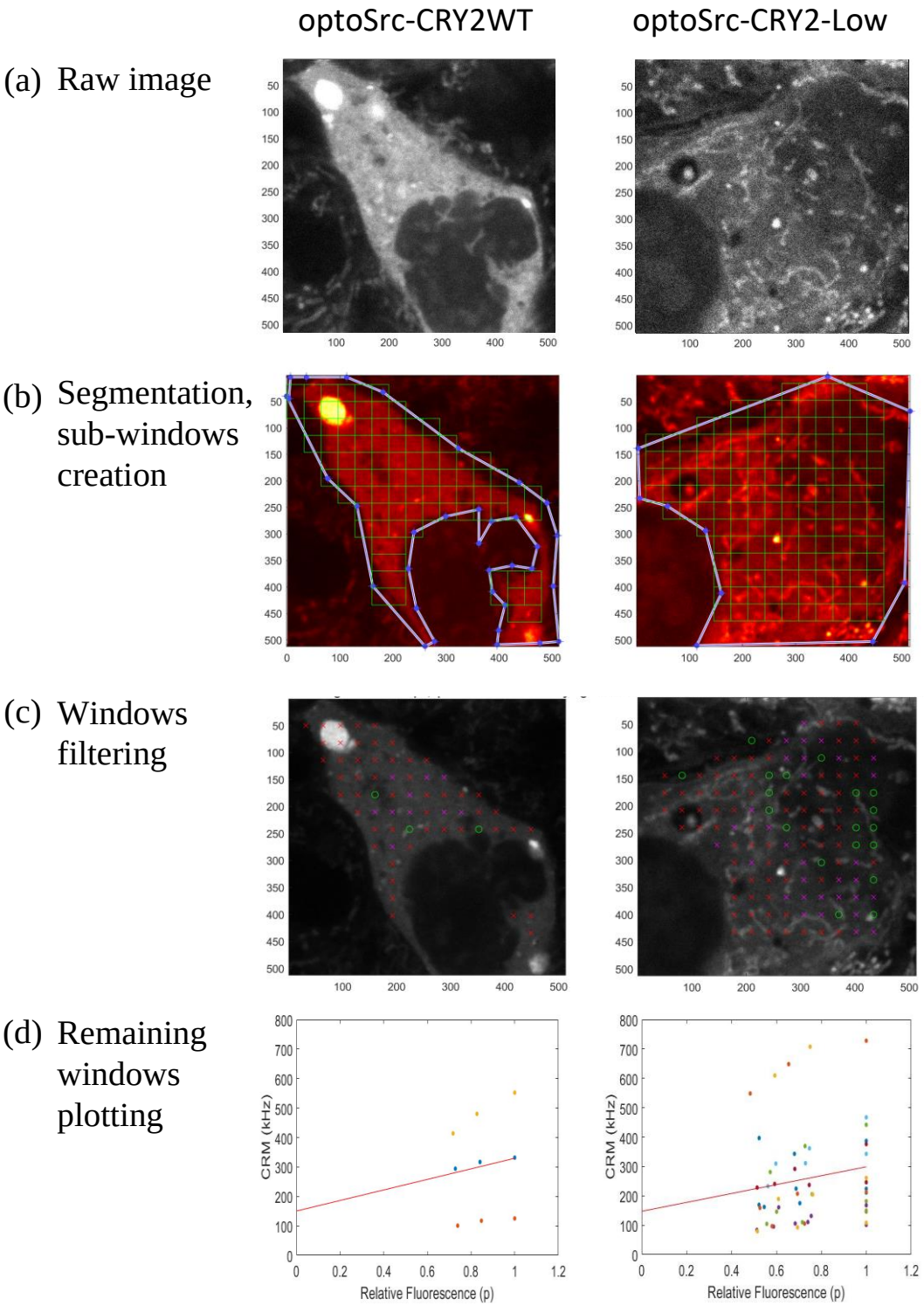


Figure 4.7: ***Photobleaching ICS analysis of oligomeric optoSrc-CRY2.*** *Representative image of optoSrc-CRY2WT and optoSrc-CRY2-Low. (a) Raw image of optoSrc in the cytosol. (b) Regions of interest (ROIs) are chosen to be where the proteins are located, i.e. outside of the nucleus. (c) Selected windows (green circles) based on autocorrelation fit and correctness of our pICS model fit. (d) Plotting of brightness of the selected windows as a function of relative fluorescence. The red line is an affine fit to the data, showing the global slope. Each series of colors represent one selected window that fit our criteria.*

We analyzed the oligomeric state of optoSrc mutants in the cytosol using the model that we have developed. Figure 4.7 shows how we proceeded with the analysis to determine the size of oligomers for each mutant. As an example, we represent the images of an optoSrc-CRY2WT cell, and an optoSrc-CRY2-Low mutant as a comparison (Fig 4.7(a)). The regions of interest (ROIs) that we selected (by drawing freely on an image of a cell) in the cytosol were divided into 64-pixel-size windows (3.2 $\mu m^2$) on which we performed local ICS (Fig. 4.7(b)). Our choice to use small windows rather than a global image analysis was due to the fact that our cells themselves were inhomogeneous. In every window, the CRM was calculated from the local autocorrelation after the flattening procedure, which was needed due to the inhomogeneity of the local intensity. The process was carried out for each relative fluorescence, *p*.

Due to the high inhomogeneity of the cell specimen that we studied; we used several filtering criteria to ensure that only data free from artifacts are retained at the end. First, there are always windows that are excluded because the autocorrelation analysis is polluted by structures in the sample that caused the waist to become incorrectly estimated. This is the first filtering process in our analysis. The dependence of the CRM upon photobleaching in the remaining windows are then fit with Eq. 3.16. In addition to the first filter, we perform the second one after the fitting process to filter windows that have a negative value of monomer brightness or slope. In Figure 4.7(c), we depict the windows that have an incorrectly estimated waist (red cross), a negative value of the brightness slope, or a negative monomer brightness (magenta cross), which we discarded. Thus, only the remaining windows (green circles) are included to obtain the graph of the measured CRM as a function of $p$ (Fig 4.7(d)). We assumed that all oligomers have the same size $n$, thus the brightness is $CRM = \varepsilon[(n-1)p + 1]$, where $\varepsilon$ is the brightness of a single monomer. In this case, the slope of the data is proportional to the size of the oligomers (minus 1). If there are only monomers $(n = 1)$, we

would see the slope is zero. If there are higher oligomers, the slope will be larger. In other words, the different slopes for the optoSrc-CRY2WT, optoSrc-CRY2-Low and optoSrc-Cry2-dead (data is not shown here) can be used as the parameter to characterize the oligomerization.

However, the quantification of the real size of oligomers is still an undergoing work. At this point, we cannot infer the real size of oligomers yet because our analysis is based only on a few windows per image, and the photobleaching is relatively weak. In order to have more reliable results, since this study is preliminary, more measurements on each cell type need to be performed in the future. Moreover, other experiments on cells before activation is indeed required to have a control system.

# Chapter 5

# Molecular Characterization in Optogenetic Cell with Fluorescence Fluctuation Method

Raster Image Correlation Spectroscopy (RICS) is one of the fluorescence fluctuation spectroscopy techniques that can resolve the dynamics of molecules on time scales ranging from microseconds to milliseconds with a spatial resolution around a few micrometers [72]. In addition, RICS requires nothing more than a standard laser scanning confocal microscope [73]. We applied RICS to one type of optogenetics cell, which is constructed with a light-gated module of CRY2 cytoplasmic protein and CIBN membrane-bound protein to determine their diffusion constant.

In this chapter, firstly, we will present the optogenetic cell model, specifically the CRY2/CIBN system, which is of interest to our research team. Then we present the RICS technique that we used to measure the diffusion constant of CIBN and CRY2. The micropatterning method as a strategy to control the variability of cell geometry during photoactivation is also described in this chapter. Additionally, we assess the dissociation kinetics of the CRY2/CIBN system.

## 5.1 Optogenetics System of CRY2/CIBN

In this optogenetics project, we are focusing on CRY2/CIBN optogenetics system that transfected on NIH 3T3 ARHGEF11 cells, which is currently exploited in our research team to control cell contractility of the stress fiber. Our initial goal was to model the whole optogenetics process from the protein photoactivation to the biochemical activity. To do so, we needed to measure the dynamics and concentration of CRY2 and CIBN, also of their heterodimerization states as a function of excitation power and duration. We were expecting that, by studying the properties of the system, we could optimize the spatial resolution of CRY2/CIBN tool.

However, during this thesis, we did not manage to complete this project. As a start, we were able to measure the dynamics of CRY2 and CIBN using Raster ICS method (we will present the method in the next section), also we could optimize the illumination conditions and observe CRY2/CIBN interaction due to the photoactivation. Afterward, to measure the recruitment of CRY2 molecules to the membrane, we had to activate the system continuously until having a stable pattern on the plasma membrane, then acquiring sufficient images for the statistics. During the continuous photoactivation, CRY2 would be instantly recruited to the membrane, and we should observe a steady state of CRY2 signal after some time. Instead, we observed the decay of the signal. The difficulty of obtaining a steady-state and a limited amount of time to look deeper into this phenomenon put us into a decision to stop the project up to the point where we could characterize the mobility of the CRY2 and CIBN protein.

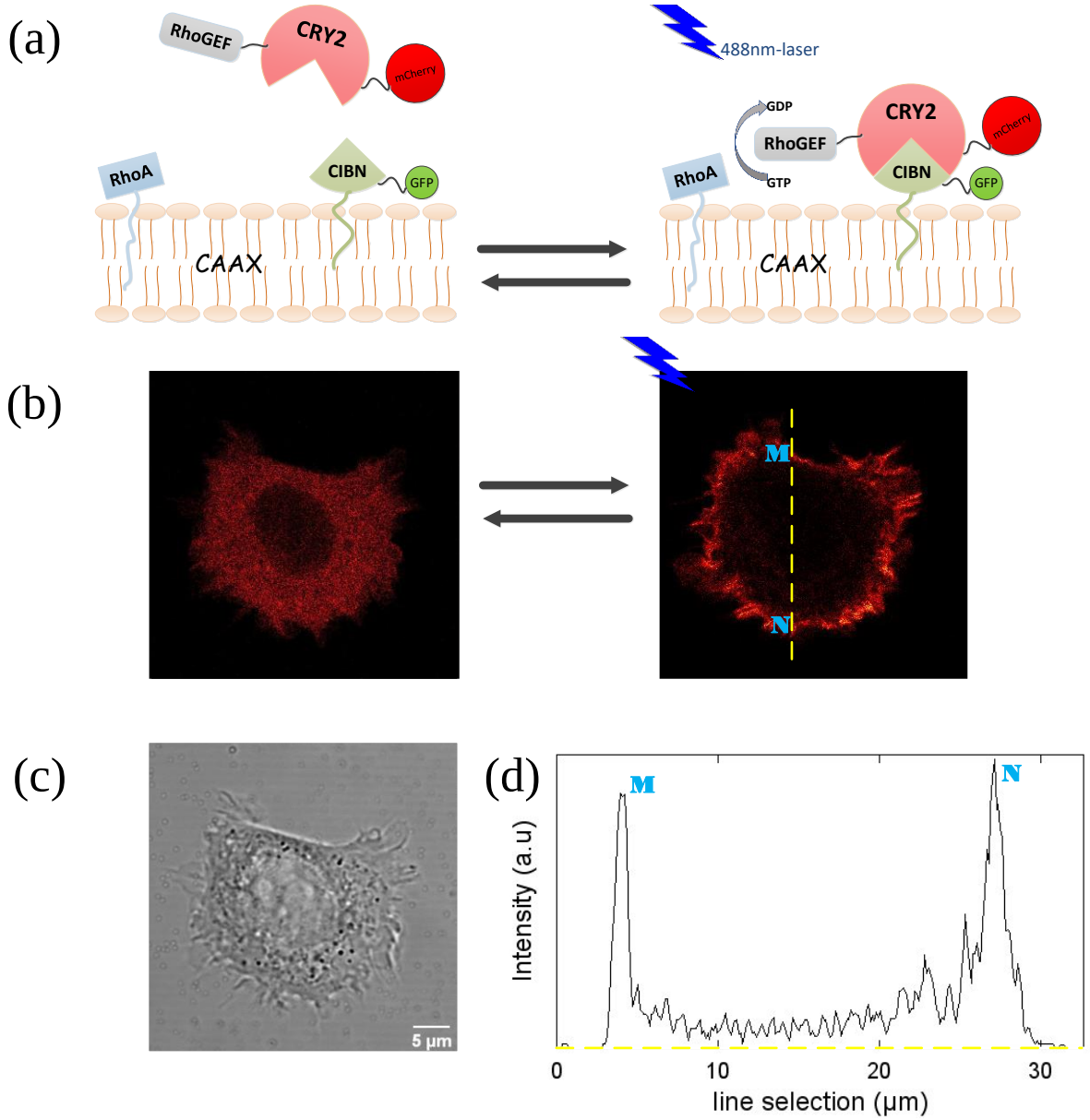


Figure 5.1: ***Optogenetics system of CRY2-mCherry/CIBN-EGFP***. *(a) Scheme of the CRY2/CIBN optogenetics probe. Sending 488nm-laser to the system triggers the affinity of CRY2-mCherry with CIBN, which is anchored in the cell membrane and is reversible in the dark. (b) Confocal fluorescence image of NIH 3T3 ARHGEF11 living cell showing the cell cytoplasm where CRY2 is located before activation (left sub-image), and during association of the pairing-proteins, CRY2 is observed at the cell membrane (right sub-image). (c) A brightfield image of the live cell with opto-construction. (d) Intensity profile of the activated cell (yellow dash line): when activated, the intensity at the membrane is higher than in the cytoplasm.*

The optogenetics system of CRY2/CIBN (Figure 5.1(a)) that we used was engineered by Valon (M. Coppey group, Institut Curie Paris) [74]. The CIBN-GFP-CAAX (CIBN) is

located at the membrane via a CAAX-motif and is tagged with GFP as a marker. CRY2PHR-mCherry-ARHGEF11 (CRY2) is a construct obtained by fusing CRY2-mCherry with the nucleotide exchange factor ARHGEF11 (RhoGEF), an activator of RhoA, in order to control cell mechanical response. When subjected to blue light, the blue-light-sensitive CRY2, which is found in *Arabidopsis thaliana*, is translocated from the cytoplasm to the cell membrane to bind to CIBN, a cryptochrome transcription factor [75]. The photoactivation also triggers the activation of RhoA, a small GTPase protein that participates in cytoskeleton regulation, which is naturally anchored to the cell membrane by its C-terminus by catalyzing the exchange of GDP for GTP [76]. When left in the dark, the CRY2/CIBN complex will dissociate [77].

The construction of CRY2/CIBN with RhoA (RhoGEF) domain was used to control the cellular migration of HeLa cells as the cell polarizes [74]. The system was later studied by measuring cellular traction force through either a single or repetitive activation of the RhoA pathways over a long period of time and proved to be reproducible. Thus, the system was confirmed to be a reliable optogenetic tool to control cell contractility [78]. However, in this thesis, we did not investigate the RhoA domain but rather to study the CRY2/CIBN system in general and measure the dynamics of each protein.

A brightfield image of the NIH 3T3 ARHGEF11 fibroblast cell constructed with CRY2/CIBN system is shown in Fig. 5.1(b). The image acquisition was focused on the cytoplasm. Under the confocal microscope, CRY2 is seen to occupy the cytoplasm before activation, and after photoactivation, CRY2 relocates to the cell membrane. Since the focal plane is focused above the ventral side of the cell, the cell apical membrane corresponds to the outer boundaries of the cell image (Fig. 5.1(b)). At this point, we see that the cell boundaries are brighter than the inside part, so that the plot profile of the intensity from a line crossing along the cell shows peaks of intensity at the boundaries (Fig. 5.1(c)).

## 5.2 Raster Image Correlation Spectroscopy (RICS)

We employed Raster Image Correlation Spectroscopy (RICS) to have a better understanding of the CRY2/CIBN system and to model the light-induced processes of the system. We chose RICS as a method of analysis because it is well suited for our cell system that consists not only of CRY2 protein that diffuses rapidly (typically 10 $\mu m^2/s$), but also CIBN protein with slower diffusion (about 0.1 $\mu m^2/s$) since it is bound to the membrane (Fig. 5.2(c)) [79,80]. On the contrary, temporal-ICS can only be applied to very slowly moving molecules because it operates on a stack of images with a temporal resolution that depends on the frame rate (usually on a timescale of seconds) [4].

The image acquisition is made in the raster scanning method (Fig. 5.2(b)): the laser linearly scans the pixels along each line with a given dwell time or time/ pixel, $\tau_{p,}$ of the order of a few microseconds, and starts again a new line every line time, $\tau_l$ (of the order of the millisecond). The whole image acquisition usually requires time in the order of a second. Because each pixel is collected at a different time, there is temporal information included in each individual image. Hence, correlating fluorescence fluctuations along a single line and across the lines in the image yields information about dynamic processes of the fast-moving molecules that occur through the corresponding time scales [72].

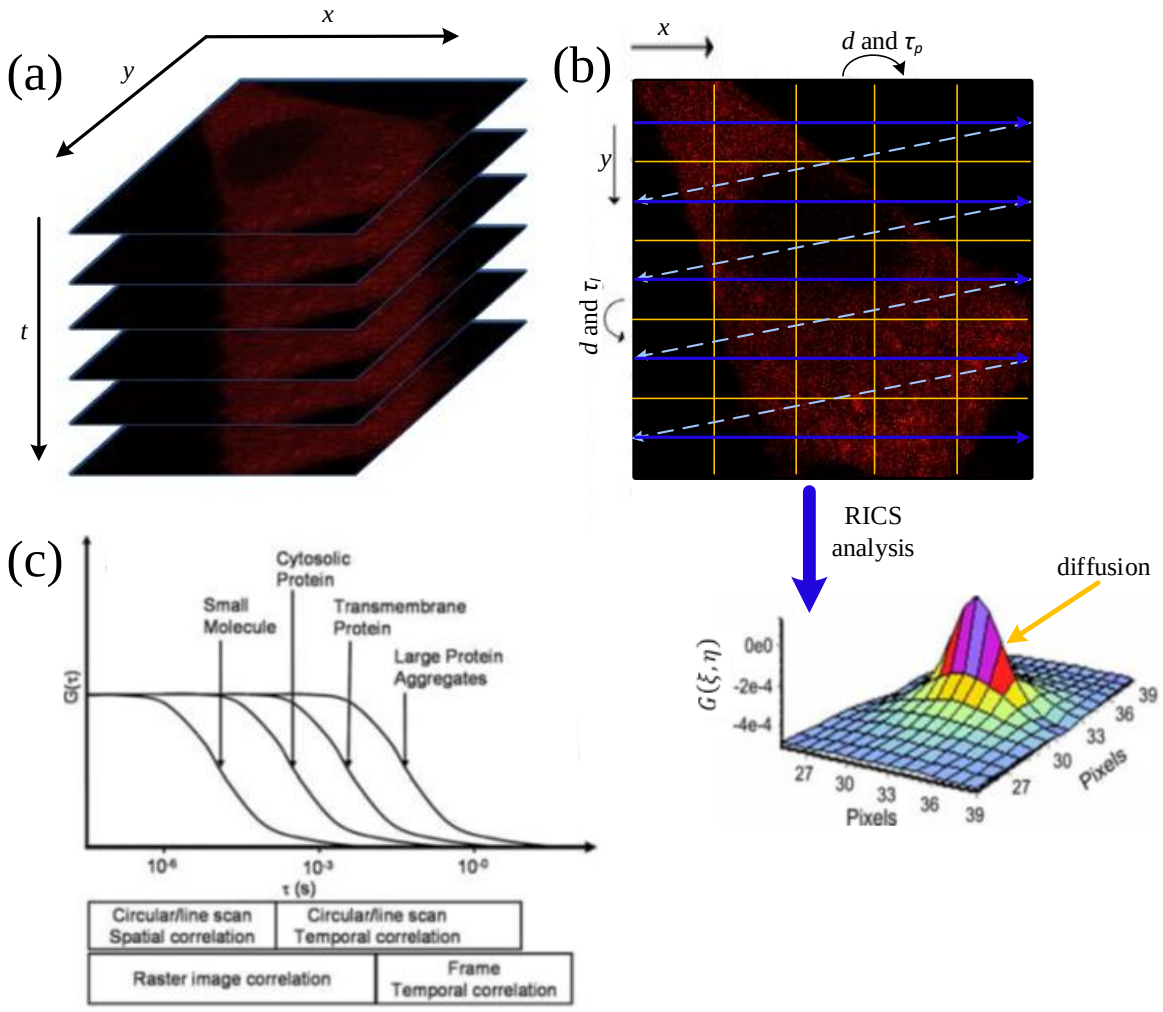


Figure 5.2: ***Raster Image Correlation Spectroscopy.*** *(a) A series of image acquired with a confocal scanning microscope. Spatial autocorrelation is done in a single image and averaged through the series of images. (b) RICS analyze the spatial autocorrelation of fluorescence signal to determine the diffusion of molecules depends on parameters of acquisition: pixel size (d), pixel dwell time ($\tau_p$), and line time ($\tau_l$). (c) Diagram of the range of diffusion times accessible by different scanning techniques. RICS is suitable for small molecules, and cytoplasmic and transmembrane proteins. Adapted from* [49].

The intensity of emitted fluorescence $F(x,y)$ among pixels bear the spatial information of the image, while the temporal information is encoded in the time lag between pixels (depending upon the pixel dwell time $\tau_p$ and the line time $\tau_l$). Consequently, it is possible to extract the molecular dynamics by autocorrelating the fluorescence signal at shifted points $(\xi,\eta)$ as given by [49]

$$G_{RICS}(\xi,\eta) = \frac{\langle \delta F(x,y)\delta F(x+\xi,y+\eta)\rangle}{\langle F(x,y)\rangle^2} \tag{5.1}$$

where $\langle F \rangle$ is the average intensity and the fluctuations is $\delta F(x,y) = F(x,y) - \langle F \rangle$. To be noticed, here the $(x,y)$ are pixel indexes.

The autocorrelation is fitted with Eq. (5.2), from which we extract the diffusion constant $D$ and the number of particles in the observation volume $N$. Equation (5.2) involves the standard temporal autocorrelation function for diffusion $G(\xi,\eta)$ and a function related to the molecular diffusion and the beam position $S(\xi,\eta)$

$$G_{RICS}(\xi,\eta) = S(\xi,\eta)G(\xi,\eta) + G_\infty \tag{5.2}$$

with $G_\infty$ an offset introduced to account for baseline variations, and

$$S(\xi,\eta) = \exp\left[-\frac{\left(\frac{\xi\delta_r}{\omega_0}\right)^2 + \left(\frac{\eta\delta_r}{\omega_0}\right)^2}{\left(1 + \frac{4D\left|\tau_p\xi + \tau_l\eta\right|}{\omega_0^2}\right)}\right] \tag{5.3}$$

where $\delta_r$ is the pixel size, smaller than the size of point spread function (PSF), $\omega_0$ is the radial beam waist. For measurements of CRY2 in the cytoplasm, a 3D free diffusion model is used to fit the dynamics part of autocorrelation and $G(\xi,\eta)$ becomes:

$$G_{3D}(\xi,\eta) = \frac{1}{N}\left(1 + \frac{4D\left|\tau_p\xi + \tau_l\eta\right|}{\omega_0^2}\right)^{-1}\left(1 + \frac{4D\left|\tau_p\xi + \tau_l\eta\right|}{\omega_z^2}\right)^{-1/2} \tag{5.4}$$

where $\omega_z$ is the axial beam waist. In the case of membranous molecules, like CIBN, the equation is simplified by fixing the axial waist to infinite, $\omega_z = \infty$, which is equivalent to assuming that the molecules diffuse only on the observation plane. Therefore, $G(\xi,\eta)$ is given by:

$$G_{2D}(\xi,\eta) = \frac{1}{N}\left(1 + \frac{4D\left|\tau_p\xi + \tau_l\eta\right|}{\omega_0^2}\right)^{-1} \tag{5.5}$$

Designing experiments of RICS needs some considerations on its acquisition parameters because its accuracy greatly depends on them. The pixel size is usually set to be four to five times smaller than the beam waist to oversample the point spread function. The scanning

times must be adapted to the mobility of molecules being measured, and the best accuracy is obtained when the diffusion time is between the pixel dwell time and the line time to have correlations in both horizontal and vertical directions. To improve the signal-to-noise ratio, RICS needs to be applied to a series of images (typically tens to one hundred) [73,80].

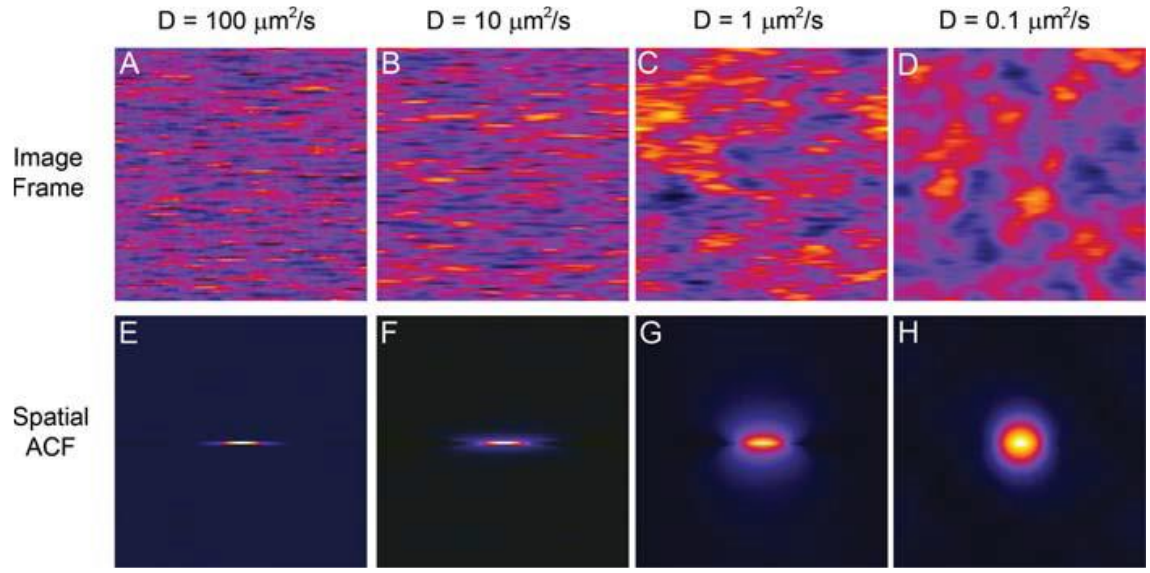


Figure 5.3: ***Simulation of Raster Image Correlation Spectroscopy.*** *When a constant scanning speed is applied to solution of variable diffusion constant, the shape of the spatial autocorrelation will reflect the particle motion. When the scanning speed is low compared to the diffusion constant, the autocorrelation shape is circular. As the speed becomes comparable (right to left), the shape of autocorrelation is elongated in the horizontal direction (the scanning direction). Taken from* [73].

Figure 5.3 shows different shapes of image autocorrelation one can obtain for a given scanning speed and various diffusion rates. If the molecules leave the laser spot in a time shorter than the line time, the autocorrelation appears as horizontal streaks because the laser spot scans the apparently immobile molecules on a line but does not hit the same mobile molecules anymore on the line after since they are gone. As the molecules move slower, the laser spot may scan the same molecules, and then the correlation broadens along the vertical axis. If the molecules are even slower or immobile, the laser beam always scans the same molecules at the same pixel. In this case, the spatial autocorrelation approaches the shape of the laser beam PSF, as seen in spatial ICS.

## 5.3 Material and Methods

Experiments with optogenetics cells were performed on a Leica SP8 confocal microscope with a 63x-water objective (NA 1.2) with Hybrid detector. We let the cells adhere to micropatterns and maintained the temperature of the cells environment at 37°C. There are two types of experiments that have been conducted with optogenetics cells during this thesis: measuring the dynamics of CRY2 and CIBN proteins, and also observing their dissociation after photoactivation.

### 5.3.1 Micropatterning

Obtaining reproducible results with live cells sample is not easy because cells are highly sensitive to geometrical and mechanical constraints from their microenvironment. Microfabrication provides an approach to restrict the location and shape of the regions where the cells can adhere, such as with micropatterns, as well as mimic the physiological environment of the cells [81]. Constraining cells on hydrogel micropatterns, in general, gives some advantages such as reducing the inter-cellular response variability and making the illumination optimization easier. In our case, the choice of plating cells in micropatterns is due to our original goal to compare experimentally the number of molecules activated with fluctuation methods to the force exerted with traction force microscopy on the same photostimulation. Hence, we used the same optogenetics module and the same substrate of hydrogel to have similar conditions.

In our experiment, the micropatterning procedure makes use of a mask method. This consists of transferring micropatterns directly produced on the quartz photomask [82]. Figure 5.4 shows the procedure of the micropatterning, described in the following: first, the mask and a glass coverslip were cleaned and then activated with plasma. A drop of poly(l-lysine)-PEG (P 8920, Sigma-Aldrich) is sandwiched between the quartz photomask and the glass coverslip

for 30 minutes of incubation. After that, the photomask was exposed to UV with UV printer machine, while the passivated glass surface was kept for the next step. Then, a drop of fibronectin solution (ECM protein) is sandwiched between the activated poly(l-lysine)-PEG and passivated glass surface, allowing the fibronectin to fill the pattern. After incubation, the micropatterns on the photomask was transferred to hydrogel polyacrylamide (PAA) by depositing a drop of PAA onto the photomask, which is then sandwiched with a silanized glass coverslip. Finally, after the PAA gel is detached from the photomask, we obtain micropatterns on hydrogel PAA.

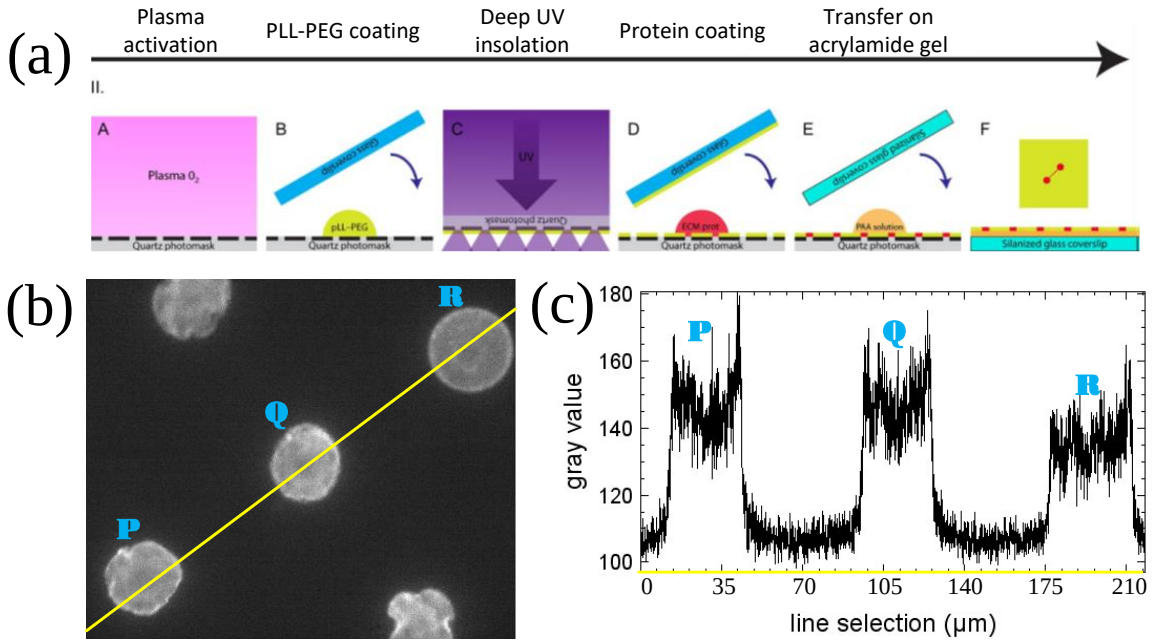


Figure 5.4: ***Micropattern of hydrogel polyacrylamide.*** *(a) Schematic of the photo mask procedure to produce micropatterns on hydrogel polyacrylamide. (b) Circular shape micropatterns, with area of 1000µm$^2$, are imaged with far-red wavelength on the widefield microscope. To obtain this image, we added Alexa546-conjugated fibrinogen on fibronectin solution during the microfabrication. (c) Plot profile of ECM protein fluorescence where* ***P*** *and* ***Q*** *are containing cells while* ***R*** *is an empty pattern, which explained higher gray values on* ***P*** *and* ***Q*** *because the proteins in cells might have been excited a little due to crosstalk. Adapted from* [82].

### 5.3.2 Sample Preparation

NIH 3T3 ARHGEF11 fibroblast cells that have been transfected with CIBN-GFP-CAAX and CRY2PHR-mCherry-ARHGEF11 (gift from M. Coppey) were cultured in DMEM (Dulbecco's modified Eagle's medium) and maintained at 37°C with a humidity of 5% CO2. For the experiment, we plated the optogenetic cells on circular-shaped hydrogel micropatterns with an area of 1000 $\mu m^2$. This was done four hours prior to the experiment to make sure the cells do not move during the activation.

### 5.3.3 Experimental Procedures

***Experiment 1: RICS to measure the dynamics of CRY2-mCherry and CIBN-GFP proteins, independently of photoactivation***

In this experiment, we imaged separately CRY2-mCherry and CIBN-GFP proteins of our optogenetic system. The acquisitions for those proteins were performed in different cells. To image CRY2-mCherry, we excited mCherry with the 561nm-laser line, and the observation was performed in the cytoplasm. The imaging was performed with an interline time of 1.43 ms (scanning speed of 700 kHz), a pixel dwell time of 1.38 μs, a pixel size of 50 nm, and an image size of 256×256 pixels with 100 frames. On the other hand, for the CIBN protein, we focused the laser at the ventral side of the cell and excited EGFP with a 488nm-laser line. The parameters for cell imaging were set at a line speed of 50 Hz (i.e., line time of 20 ms), pixel dwell time of 9.75 μs, and pixel size of 40 nm. The acquired images were in 512×512-pixel format with 70 frames.

***Experiment 2: Measuring characteristic time of dissociation of CRY2-mCherry proteins from the CIBN-GFP after photoactivation***

In this experiment we performed three sets of sequences (Fig. 5.5). Firstly, a 561nm-laser line was used to image CRY2-mCherry in the cytoplasm for 3 minutes of which signal was going to be used as the base level of intensity. Secondly, we activated the cell with 488nm-laser line for 630 ms, so that CRY2 binds to CIBN at the membrane. Lastly, we left the cell in the dark for 13 minutes using the 561nm-laser, during which we recorded the relaxation of the cell (CRY2/CIBN dissociation) by observing the changes of CRY2 intensity as we will detail later. The acquired images have a 1024×1024-pixel format, with a pixel size of 40 nm and a dwell time of 600 ns. The observations were performed in the cytoplasm, about 1 µm above the ventral side of the cell.

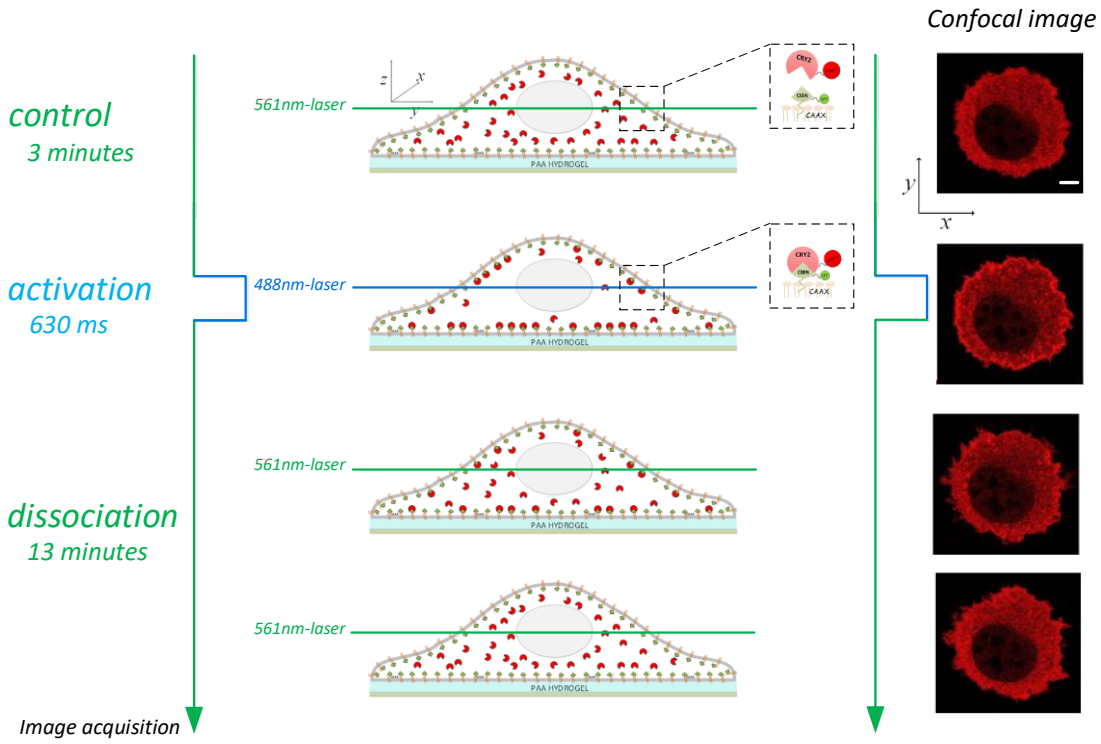


Figure 5.5: ***Experimental procedure to observe dissociation of CRY2/CIBN.*** *The image acquisition starts by recording the fluorescence signal of CRY2-mCherry at cytoplasm with 561nm-laser on a living cell plated on circular patterns of 1000 µm$^2$. The cell is then activated with 488nm-laser before left in the dark while recorded with 561nm-laser. The right-hand side images are the confocal images of the cell as the acquisition is performed. The scale bar is 5 µm.*

### 5.3.4 Image Analysis

***Analysis with RICS with defined whole region***

Analysis of a stack of fluorescence images with RICS used a custom-made script (I. Wang, LIPhy) in MATLAB. The script allows us to choose a rectangular region to analyze, making the assumption that the behavior of molecules in the region is homogeneous. Before calculating the autocorrelation (Eq. 5.1), the background removal of immobile structures is done via subtraction of a moving average: after the user has chosen the *n* number of images to average (typically around 10), the script would subtract from each frame the average of the *n* frames that surround it. After calculating the autocorrelation of each individual image, all autocorrelations were averaged over the series of images. The autocorrelation function is fit using Eq. 5.2. where the fitting parameters ($G(0)$, $\omega_0$, and $G_\infty$) were left free, which in turn was determined with a non-linear least-squares solver. The fitting allows extracting information on the dynamics of the fluorescent molecules that was hidden in the spatial autocorrelation signal. We fit with 3D diffusion model (Eq. 5.4) for the case of cytoplasmic protein, or 2D diffusion model (Eq. 5.5) for the membranous protein.

***Analysis with scanning RICS for mobility mapping***

To map the mobility of CIBN on the membrane, we used another version of the RICS script where we use intensity thresholding to define the region of interest so that the zone outside the cell was excluded on the autocorrelation calculation. On this region, we created a scanning window that has the size of 64-pixels (2.5×2.5 μm) on which we perform an individual RICS. The sampling step is chosen to be half of the width of the window (i.e., 32 pixels for 64x64 pixel windows), so there is some overlap between the windows; for example, when the first window is located at pixel 1, then the second window starts at pixel 32. So, when we chose a window size of 64×64 pixels, the fluorescence image resulted in a map with

15×15 windows (we did not take into account the last half-windows). The autocorrelation and background subtraction were done in the same way as what we did with the RICS of the whole region.

***Analysis of characteristic time of dissociation of CRY2/CIBN***

The characteristic time of CRY2/CIBN dissociation is measured by monitoring the change of intensity of mCherry at the edge of the cell by creating a band at the region with ImageJ. The edge of the cell represents the cell membrane where the CRY2 molecules bind to CIBN during photoactivation. Observing the intensity on the cell edge allows us to follow the activation and the decay of intensity after cell activation over time. The characteristic time is determined from the half-time of the decay.

## 5.4 Measuring the dynamics of CRY2 and CIBN with RICS

We perform RICS on CRY2 and CIBN proteins individually to calculate their diffusion constant. For that, we did not activate the optogenetics system and excited each protein separately with laser lines at low power: 488nm-laser for CIBN activation and 561nm-laser for CRY2 activation. Figure 5.7(a) shows a brightfield image of the same cell with CIBN/CRY2 opto-construct, and fluorescence image of each protein. We used a region as wide as possible on the membrane to analyze CIBN, while for CRY2, we took an area in the cytoplasm outside the nucleus.

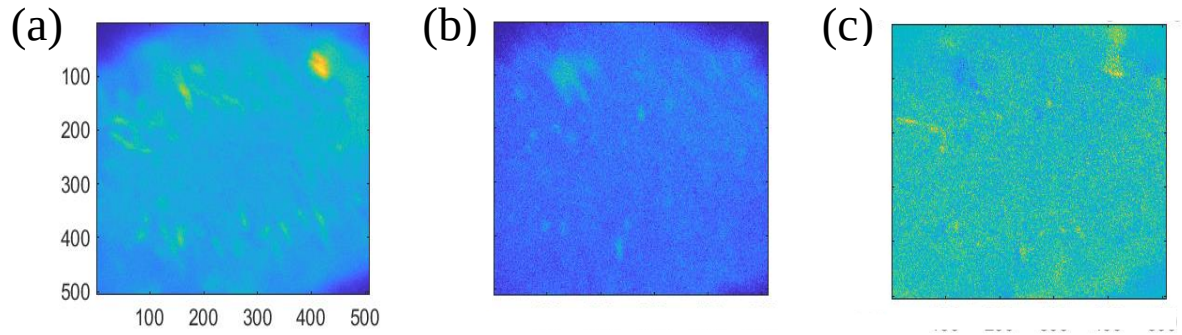


Figure 5.6: ***Background removal process with the moving average.*** *(a) Fluorescence image (512×512 pixels, 20 μm$^2$) of CIBN at the cell membrane. (b) Average image of 10 frames. (c) Subtracted image after background removal with 10 moving average image.*

Cells display immobile or slow-moving features such as microtubules and organelles that provide background, which may dominate the spatial autocorrelation. Hence, background subtraction is an important step before performing RICS [83,84]. One common method to subtract the background prior to image correlation analysis is the moving average method [49]. In this method, a range of consecutive images is averaged and then used as the image of the immobile structure and subtracted to the raw data (Fig. 5.6). After subtracting the average image, the pixel intensities fluctuate around zero, so a constant level equal to the mean of the average image should be added. After removing the immobile structure, the autocorrelation on each image is calculated. Then, the autocorrelation of all images is averaged and fit to extract the diffusion coefficient and the number of molecules in the observation volume [72]. This method works well to measure the dynamics of the molecules because it preserves the shape of the autocorrelation function. However, it does not accurately determine the number of molecules which comes from the amplitude of the autocorrelation function. The constant, which is added to the individual image, contains mobile and immobile components. Thus, RICS will calculate the number of mobile molecules which is biased by the presence of the immobile structure. In short, the number of molecules provided by the autocorrelation is overestimated [73,84].

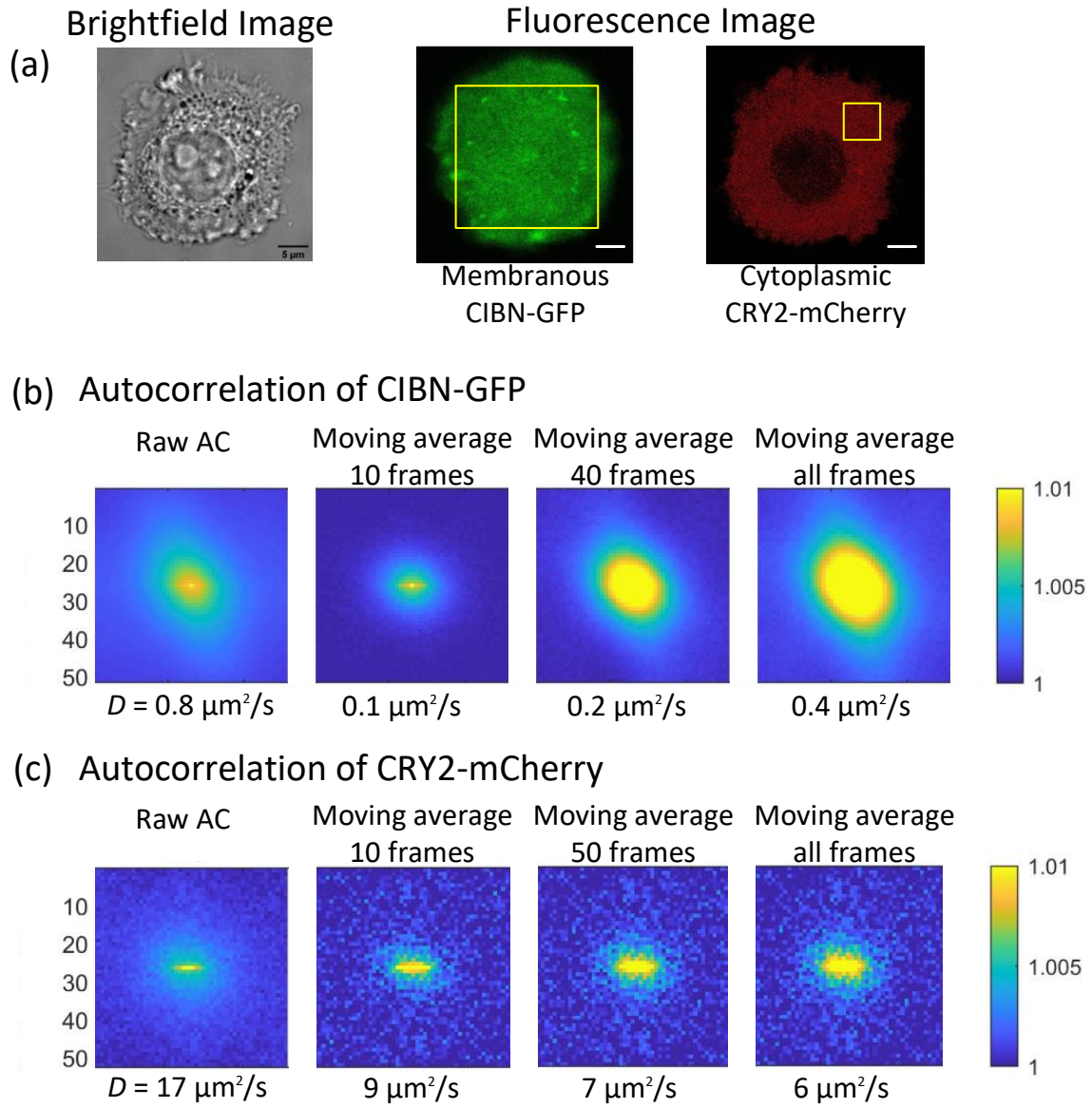


Figure 5.7: ***Effect of background removal to autocorrelation in RICS.*** *(a) Representative image of optogenetics cells adhered on a circle-shaped micropattern. The confocal image of CIBN-EGFP is taken at the membrane (in green) and CRY2-mCherry is taken in the cytoplasm (in red). A typical region of interest (ROI) chosen during the image analysis indicated by yellow rectangle. The scale bar is 5 µm. (b and c) Autocorrelation before and after background removal for CIBN and CRY2.*

The effect of the subtraction of immobile or slow-moving structures on autocorrelation is shown in Fig. 5.7(b) and (c) for CIBN and CRY2, respectively, where we used the moving average background removal with different number of frames. The time interval of ten frames (100 seconds for CIBN, 4 seconds for CRY2) is considered short enough compared to the

typical motion of the structures we want to remove. Therefore, a moving average subtraction with ten frames is efficient to remove the background structures, and only the fluctuations of interest due to the mobile proteins would be analyzed. As a result, the autocorrelation shape is not as broad as the raw autocorrelation, where we include the contribution from the structures. On the other hand, since the structures may have slowly moved during image acquisition, taking too many frames (with 40, 50, and 100 frames) for background removal caused the broadening of the autocorrelation. The broadening is a result of the incomplete removal of the slow-moving components because the structures have moved during the time interval used for averaging, leading to an erroneous autocorrelation. The broadening is particularly apparent when there are bright structures present in the images, which is the case of the membranous images, whereas it is more homogenous at the cytoplasm (see also Fig 5.8(a)). Hence, we see that background removal has less effect on the autocorrelation shape for CRY2 images.

Nevertheless, we would like to point out that in RICS, it is important to remove the background using a small number of frames in the moving average method, especially for the proteins at the membrane, of which the image is poorly homogenous. In the case of CIBN, when using all frames to average, i.e., the structures are considered immobile the whole time, we observed that the shape of the autocorrelation function is incorrect and cannot be fitted with a RICS model; thus, the diffusion constant is biased to about four times larger than that calculated from the moving average with ten frames.

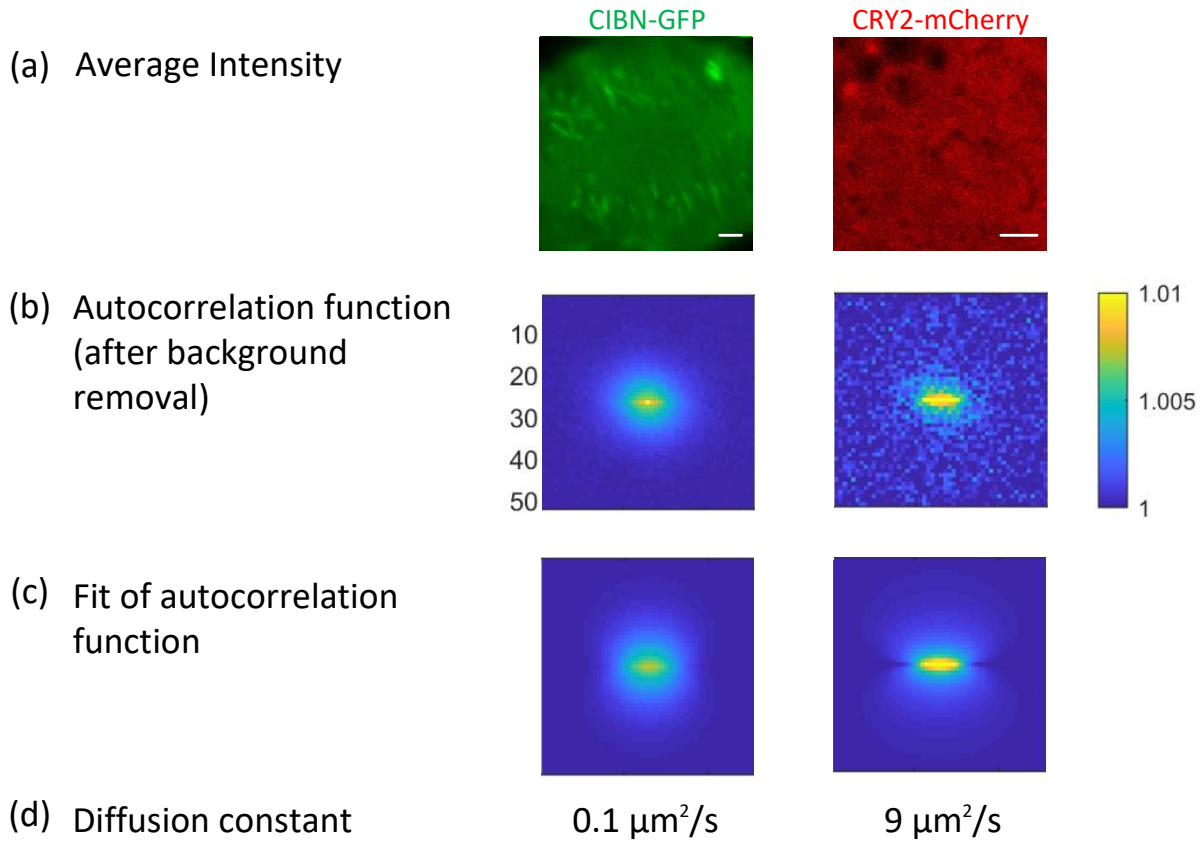


Figure 5.8: ***Autocorrelation function and fit of autocorrelation function with RICS performed on proteins in optogenetics cells.*** *(a) The average intensity of CIBN and CRY2 in the region of interest. The scale bar is 2 µm². (b) Spatial autocorrelation function after background removal using a ten-frame moving average. (c) Fit of the autocorrelation after background removal. (d) Diffusion constant of CIBN and CRY2 from the fit of the autocorrelation with RICS on the whole image.*

Once the background subtraction is done, the autocorrelation allows us to extract the diffusion constant of proteins. The RICS analysis is shown in Fig. 5.8 which is obtained by analyzing the whole fluorescence image. The diffusion constant for CRY2 is 9 $\mu m^2/s$, which is comparable to the value reported for the cytoplasmic protein construct of pEYFP-N3 in NLFK cells (about 15 $\mu m^2/s$) [85]. In the case of CIBN-GFP, we found that it diffuses slower with an average diffusion constant of 0.1 $\mu m^2/s$, which is similar to that obtained with the FRAP technique (about 0.1 $\mu m^2/s$) [79] where a small membrane region is photobleached and the diffusion constant is calculated from the rate of fluorescent molecules repopulated the region.

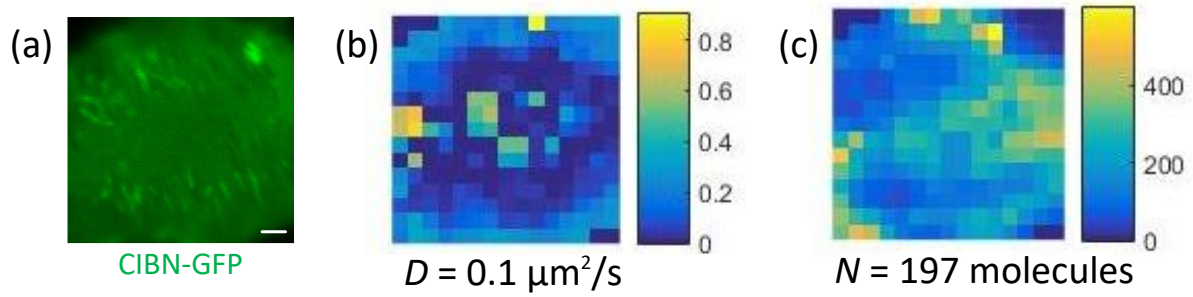


Figure 5.9: ***Mobility and concentration map of CIBN*** *(a) The fluorescence image of CIBN-GFP on which a scanning sub-image (64x64 pixels, 2.5 μm$^2$) is created to perform spatially resolved RICS. (c) The corresponding number of molecules.*

In the cell membrane that we represented in Fig. 5.9(a), we want to see the variability of the diffusion constant and the number of molecules over the image. To generate the maps for CIBN, we perform RICS locally on 64-pixels windows over the whole fluorescence image, where each window is assumed to be homogenous. The mobility and concentration maps of CIBN are shown in Fig. 5.9(b) and (c). We found that CIBN-GFP diffuses with an average diffusion constant of 0.1 μm$^2$/s, which is consistent with the value when we analyze the whole image. We could also see the variability of the number of molecules over the membrane; however, the average number of molecules determined by RICS is likely biased by the background removal, as we explained earlier. Performing RICS locally also allows us to see the variability of the values over the image. The mobility map of CIBN of the ventral membrane shows that the dynamics are faster at the edge of the cell compared to the center. We suspect two possibilities that drive this difference, which we cannot distinguish at this point. First, it could be the fact that there was a non-flatness between the center and the edge of the cell, which was caused by the pulling effect of the cell that plated on the hydrogel when we sent light to it. Another reason is that there could be some difference in membrane dynamics between the cell center and the edge, but we did not look further into these possibilities.

## 5.5 Dissociation Kinetics of CRY2/CIBN

The dissociation is an important parameter in the kinetics of the optogenetics system because, together with the illumination geometry and the diffusion constants of the involved proteins, it determines the temporal and spatial resolution of the activation process. There have been studies about the properties of CRY2/CIBN system, which mention that CRY2 was recruited to CIBN with a spatial resolution of 5 µm, a characteristic time of five seconds to create the perturbation and a dissociation time of 185 ± 40 s. It means that the dissociation reaches 63% in three minutes and 95% in nine minutes [77,79].

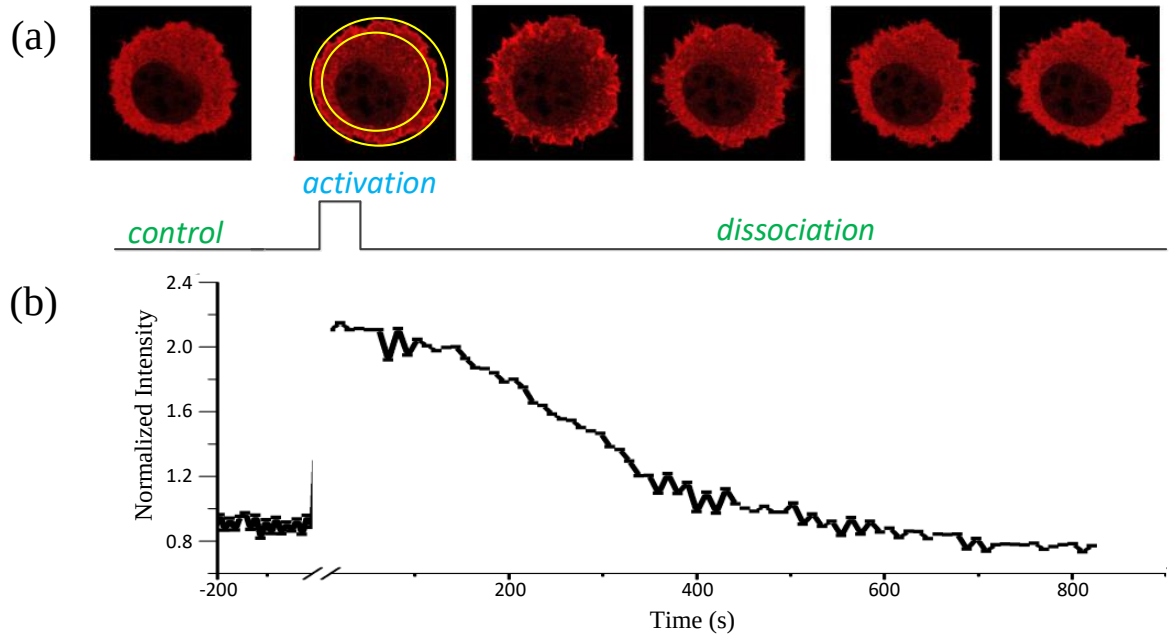


Figure 5.10: ***CRY2 recruitment to the membrane***. *(a) Confocal images showing the increase of intensity of mCherry at the membrane (along the cell edges) as CRY2 associated with CIBN. (b) A decay of mCherry intensity at the membrane after photoactivation. The intensity of the activated CRY2-mCherry signal is read from the ROI in between the two yellow circles. The average characteristic time of dissociation of CRY2-mCherry is 208 ± 14 s, calculated from 6 samples.*

Figure 5.10(a) shows changes in image intensity as CRY2 bind to CIBN and then unbind. On this cell, we see that when we shine 488nm-laser onto the whole cell, some parts of the cytoplasmic CRY2-mCherry are spontaneously recruited to the membrane which is

indicated by a depletion of the fluorescence intensity in the cytoplasm (around the dark zone due to the nucleus) and an increase of fluorescence at the periphery of the cell. It is also worth to notice that the central part of the cell is always darker because the focal plane cut through the nucleus where CRY2 cannot access. After a pulse of activation, the system is placed in the dark. Under this condition, the intensity at the membrane decreases because the CRY2/CIBN complex dissociates and returns to the cytoplasm.

To determine the characteristic time of dissociation of the CRY2/CIBN system, we use the changes of intensity at the membrane, *i.e.,* the periphery of the cell that is chosen as the region of interest (ROI) indicated by the area in between the two yellow circles. This ROI indicates the membrane of the cells where CRY2 binds to CIBN so that the fluorescence signal in the area changes. Figure 5.10(b) shows changes in the fluorescence signal from this ROI. To measure the time constant, we measured the half-time of the decay of the signal after photoactivation. Finally, the complex of CRY2-CIBN dissociates with a characteristic half-time of 208 ± 14 seconds. The characteristic half-time of dissociation is consistent with previous reports ($\sim$250 seconds) that measure the dissociation kinetics using the decay of the total amount of CRY2 in the plasma membrane over time [79].

## 5.6 Conclusion

We have been able to perform Raster Image Correlation Spectroscopy (RICS) on optogenetics cells. We chose RICS as it can cover the diffusion of cytoplasmic protein as well as the membranous protein. Cells represent a heterogeneous environment where immobile or slow-moving structures can dominate the autocorrelation function, which will obscure the correlations due to the faster moving molecules. We observe that for our measurements, using a 10-frames to average in the background removal algorithm is a good compromise to get rid

of the contribution of the structures. After that, a proper autocorrelation of the whole image can be performed and fit to calculate the diffusion constant of CRY2 and CIBN.

Performing autocorrelation of RICS on the whole image of CIBN gives a consistent value of the average diffusion constant as when it is done locally on sub-images. On the other hand, doing a local RICS allows us to see the variability of the dynamics of protein over the cell membrane, although the number of the molecules is inevitably biased by the background from immobile structures.

The diffusion that we calculated with RICS shows consistent values with those that were obtained from other techniques such as FRAP. However, in respect to FRAP, RICS has a better temporal resolution, which makes it usable for studying faster dynamics like cytoplasmic diffusion. In addition to this, RICS can easily allow us to see the variability of the dynamics over the field of view, whilst FRAP only gives a single estimation of the parameter.

We could also characterize the kinetics of the dissociation of CRY2 at the cell membrane by analyzing the temporal variations of the intensity in various segmented regions of the optogenetics cell. The characteristic time of dissociation of CRY2 that we measured is 3 minutes.

Concerning RICS performance on optogenetics cells, we believe that measuring the mobility and concentration of recruited CRY2 dimers at the ventral membrane to study the interaction of CRY2 and CIBN is still to be potentially carried out in the future. However, this technique certainly requires images of stationary conditions of the fluorescence signal during photoactivation that we have not yet managed to observe so far as well as a good signal to noise ratio.

# General Conclusions

Advances in microscopy techniques have been remarkable in respect to their early development, notably with the discovery of fluorophores that led to extensive use of fluorescence microscopy. However, the standard fluorescence microscopy is not quantitative. Nowadays, imaging is not the only important matter, but the quantitative tools are also indispensable to provide more reliable results in understanding the biological systems. One of the quantitative techniques devoted to concentration, interactions, and transport is Fluorescence Fluctuation Microscopy (FFM). This manuscript has covered some of the FFM techniques, mostly Image Correlation Spectroscopy (ICS) and Raster Image Correlation Spectroscopy (RICS), with some applications in biology. These tools make use of image scanning, which is, on the other hand, not the case for the standard Fluorescence Correlation Spectroscopy technique (FCS), that is a single point measurement, and are accessible with a commercial laser scanning confocal microscope.

Image Correlation Spectroscopy is intended to analyze immobile molecules but, even though the standard ICS can be used to determine the molecular density, it can be biased when performed on a system of oligomers having a distribution of brightness. A smart ICS modality making use of photobleaching between consecutive frames has been introduced for

such system of oligomers. We have developed a general formalism of photobleaching ICS (pICS) that relates the measured brightness to the initial distribution of fluorophores. This model is applicable for a system with an arbitrary distribution of brightness, contrary to its precedent application on specific cases of Poissonian labeling and homogenous oligomers system. We applied the model to fluorescent nano-beads deposited on a surface that have a wide distribution of brightness and managed to retrieve the brightness of a single fluorophore (that labels the beads) despite the different concentrations of beads. Performing measurement on beads, we could conclude that our pICS model is consistent with the experimental study. In another application of pICS, we performed measurements on ligands bearing a various number of fluorophores, assumed to obey Poisson distribution. We observed that pICS might be applicable to measure the number density.

Raster Image Correlation Spectroscopy (RICS) is a fluctuation technique that we employed to optogenetics cells of the CRY2/CIBN system, where the heterodimerization of CRY2/CIBN is stimulated by 488nm-laser. The RICS analysis relies on the shape of the autocorrelation function to measure the dynamics of moving molecules within a wide range of diffusion constant. Therefore, RICS allows us not only to measure the diffusion of slow processes such as diffusion at the plasma membrane but also to access faster molecules such as the cytoplasmic protein. We performed measurements on optogenetics cells of the CRY2/CIBN system. CRY2 is cytoplasmic, while CIBN is a membranous protein. RICS analysis of both proteins gives the value of diffusion constants, which are similar to those obtained with the FRAP technique. In addition, RICS provides a mapping of protein's mobility across the whole-cell membrane, which cannot be obtained with FRAP. Finally, we also characterized the characteristic time of dissociation of this pair by analyzing the temporal variations of the intensity at the cell membrane after the activation.

Meanwhile, however, we also encountered some issues regarding the analysis of the image correlation techniques. The most prominent problem is the background, which should be removed so as not to bias the analysis. When performing pICS on species deposited on a surface, the background can be subtracted with background images recorded in the solution or using a fixed value of the background obtained as an average value of background of all photobleaching stages. On the other hand, while doing RICS on optogenetics cells, the background coming from immobile structures are not so easy to handle. Indeed, the moving average method has managed to remove the immobile structures to estimate the diffusion constant correctly, but in the absence of additional information about the relative concentrations of the mobile and immobile structures, RICS cannot estimate the number of molecules reliably.

Despite the limitations, it is possible to improve the techniques. Concerning pICS, we have seen so far that in the general case of an unknown fluorophore distribution, the information that one can obtain from the analysis of the autocorrelation as a function of relative fluorescence is the single monomer brightness and the statistical parameters of a combination of mean and variance of oligomers distribution. Our model also works for a system that consists of two known size of oligomers, for example, monomers and dimers, to measure the fraction for each oligomer. But if we assume that there are also other oligomers with different unknown sizes, say trimers, and so on, then our method fails. To exploit the fluorophore distribution even further, one possibility would be to measure the dependence of higher-order moments of the fluorescence signal as a function of photobleaching, for example, by using cumulant analysis [86]. The cumulants are directly related to the moments of the distribution of the number of fluorophores. Indeed, our method has successfully exploited the first- and the second-order moments, but the cumulant analysis of higher-order would be useful to extract more information on the fluorophore distribution. However, the

experimental estimation of cumulants is all the more uncertain and noisier at the order of the cumulant increases. Therefore, such methods would only be possible for very bright fluorophores.

Concerning RICS measurements, although we could observe the association of CRY/CIBN pairing in optogenetics cells, we have not yet managed to apply RICS to calculate the mobility of the photo-dimerized complex. The optogenetic cell tends to evolve during image acquisition due to photoactivation, while to perform RICS, it requires tens of images that should be acquired under the same condition. If the stationary state of the photoactivation is manageable, we could deploy RICS to estimate the mobility of CRY2/CIBN complex, which further may be useful to characterize the temporal and spatial resolution of the CRY2/CIBN systems.

In a nutshell, we believe that the quantitative fluctuation techniques that we have discussed and developed in this manuscript will be useful for future applications in biology.

# Bibliographies


[1] S. W. Thomson, in *Pract. Appl. Electr.* (The Institution of Civil Engineers, London, 1884), pp. 149–176.

[2] N. J. Marianayagam, M. Sunde, and J. M. Matthews, Trends Biochem. Sci. **29**, 618 (2004).

[3] E. L. Elson and D. Magde, Biopolymers **13**, 1 (1974).

[4] D. L. Kolin and P. W. Wiseman, Cell Biochem. Biophys. **49**, 141 (2007).

[5] N. O. Petersen, P. L. Höddelius, P. W. Wiseman, O. Seger, and K. E. Magnusson, Biophys. J. **65**, 1135 (1993).

[6] C. Frantz, K. M. Stewart, and V. M. Weaver, J. Cell Sci. **123**, 4195 (2010).

[7] A. Lajevardipour, J. W. M. Chon, and A. H. A. Clayton, AIMS Biophys. **2**, 1 (2015).

[8] B. R. Masters, *Confocal Microscopy and Multiphoton Excitation Microscopy : The Genesis of Live Cell Imaging* (SPIE - The International Society for Optical Engineering, Washington, 2005).

[9] M. S. Sushmasusik and M. S. Hayath, Indian J. Mednodent Allied Sci. **3**, 170 (2015).

[10] A. J. M. Wollman, R. Nudd, E. G. Hedlund, M. C. Leake, and M. C. Leake, Open Biol. **5**, (2015).

[11] B. Herman, *Fluorescence Microscopy and Fluorescent Probes*, 1st ed. (Springer Science+Business Media, New York, 1996).

[12] J. R. Lakowicz, *Principles of Fluoresecnce Spectroscopy*, 9th ed. (Springer, Singapore, 2006).

[13] P. P. Mondal and A. Diaspro, *Fundamentals of Fluorescence Microscopy*, 1st ed. (Springer, New York, 2014).

[14] N. Rusk, Milestones 58 (2009).

[15] C. P. Toseland, J. Chem. Biol. **6**, 85 (2013).

[16] G. J. Kremers, S. G. Gilbert, P. J. Cranfill, M. W. Davidson, and D. W. Piston, J. Cell Sci. **124**, 157 (2011).

[17] R. Rizzuto, M. Brini, P. Pizzo, M. Murgia, and T. Pozzan, Curr. Biol. **5**, 635 (1995).

[18] K. Thorn, Mol. Biol. Cell **28**, 848 (2017).

[19] M. M. Barroso, J. Histochem. Cytochem. **59**, 237 (2011).

[20] U. Resch-Genger, M. Grabolle, S. Cavaliere-Jaricot, R. Nitschke, and T. Nann, Nat. Methods **5**, 763 (2008).

[21] K. D. Wegner and N. Hildebrandt, Chem. Soc. Rev. **44**, 4792 (2015).

[22] C. Eggeling, J. Widengren, R. Rigler, and C. A. M. Seidel, Anal. Chem. **70**, 2651 (1998).

[23] J. W. Dobrucki, *Fluorescence Microscopy From Principles to Biological Applications*, 2nd ed. (Wiley-Blackwell, Weinheim, 2017).

[24] O. Shimomura, J. Microsc. **217**, 3 (2005).

[25] O. Shimomura, Angew. Chem. Int. Ed. Engl. **48**, 5590 (2009).

[26] M. Chalfie, Y. Tu, G. Euskirchen, W. Ward William, and C. Prasher Douglas, Science (80-. ). **263**, 802 (1994).

[27] S. J. Remington, Protein Sci. **20**, 1509 (2011).

[28] R. Y. Tsien, FEBS Lett. **579**, 927 (2005).

[29] E. C. Jensen, Anat. Rec. **295**, 2031 (2012).

[30] A. Ettinger and T. Wittmann, *Fluorescence Live Cell Imaging*, 1st ed. (Elsevier Inc., California, 2014).

[31] W. Gray (Jay) Jerome, in *Basic Confocal Microsc.*, edited by R. L. Price and W. Gray (Jay) Jerome, 2nd ed. (Springer, Switzerland, 2018).

[32] S. Veettil, N. Budisa, and G. Jung, Biophys. Chem. **136**, 38 (2008).

[33] D. Satsoura, B. Leber, D. W. Andrews, and C. Fradin, ChemPhysChem **8**, 834 (2007).

[34] D. E. Koppel, D. Axelrod, J. Schlessinger, E. L. Elson, and W. W. Webb, Biophys. J. **16**, 1315 (1976).

[35] B. L. Sprague, R. L. Pego, D. A. Stavreva, and J. G. McNally, Biophys. J. **86**, 3473 (2004).

[36] M. Minsky, 3013467 (Patent) (1961).

[37] R. Heintzmann and G. Ficz, Briefings Funct. Genomics Proteomics **5**, 289 (2006).

[38] P. C. Goodwin, *Quantitative Deconvolution Microscopy*, 1st ed. (Elsevier Inc., 2014).

[39] T. Weidemann, J. Mücksch, and P. Schwille, Curr. Opin. Struct. Biol. **28**, 69 (2014).

[40] P. W. Wiseman, C. M. Brown, D. J. Webb, B. Hebert, N. L. Johnson, J. A. Squier, M. H. Ellisman, and A. F. Horwitz, J. Cell Sci. **117**, 5521 (2004).

[41] N. O. Petersen, Biophys. J. **49**, 809 (1986).

[42] D. Magde, E. L. Elson, and W. W. Webb, Phys. Rev. Lett. **29**, 705 (1972).

[43] D. Magde, E. L. Elson, and W. W. Webb, Biopolymers **13**, 29 (1974).

[44] Z. Földes-Papp, U. Demel, and G. P. Tilz, Proc. Natl. Acad. Sci. U. S. A. **98**, 11509 (2001).

[45] R. Rigler and P. Kask, Eur. Biophys. J. **22**, 169 (1993).

[46] J. Ries and P. Schwille, BioEssays **34**, 361 (2012).

[47] E. Haustein and P. Schwille, Annu. Rev. Biophys. Biomol. Struct. **36**, 151 (2007).

[48] N. González Bardeci, J. F. Angiolini, M. C. De Rossi, L. Bruno, and V. Levi, IUBMB Life **69**, 8 (2017).

[49] M. A. Digman, C. M. Brown, P. Sengupta, P. W. Wiseman, A. R. Horwitz, and E. Gratton, Biophys. J. **89**, 1317 (2005).

[50] M. Srivastava and N. O. Petersen, Methods Cell Sci. **18**, 47 (1996).

[51] D. L. Kolin, D. Ronis, and P. W. Wiseman, Biophys. J. **91**, 3061 (2006).

[52] B. Hebert, S. Costantino, and P. W. Wiseman, Biophys. J. **88**, 3601 (2005).

[53] M. A. Digman and E. Gratton, Annu. Rev. Phys. Chem. **62**, 645 (2011).

[54] P. W. Wiseman, Cold Spring Harb. Protoc. **2015**, 336 (2015).

[55] A. Delon, I. Wang, E. Lambert, S. Mache, R. Mache, J. Derouard, V. Motto-Ros, and R. Galland, J. Phys. Chem. B **114**, 2988 (2010).

[56] G. D. Ciccotosto, N. Kozer, T. T. Y. Chow, J. W. M. Chon, and A. H. A. Clayton, Biophys. J. **104**, 1056 (2013).

[57] FluoSpheres Fluorescent Microspheres F8786, Invitrogen https://www.thermofisher.com/document (2005).

[58] Y. Gao and M. L. Kilfoil, Opt. Express **17**, 4685 (2009).

[59] J. C. Crocker and D. G. Grier, *Methods of Digital Video Microscopy for Colloidal Studies* (1996).

[60] T. Hagiwara, P. Nattawut, M. Shibata, and T. Sakiyama, Biosci. Biotechnol. Biochem. **81**, 783 (2017).

[61] H. Fujiwara, *Spectroscopic Ellipsometry*, 1st ed. (John Wiley & Sons, Ltd, West Sussex, 2007).

[62] D. Yokoyama and C. Adachi, J. Appl. Phys. **107**, (2010).

[63] J. S. Verdaasdonk, J. Lawrimore, and K. Bloom, *Determining Absolute Protein Numbers by Quantitative Fluorescence Microscopy*, 1st ed. (Elsevier Inc., 2014).

[64] V. C. Coffman and J. Q. Wu, Trends Biochem. Sci. **37**, 499 (2012).

[65] V. C. Coffman and J. Q. Wu, Mol. Biol. Cell **25**, 1545 (2014).

[66] B. Sørensen, M. Tang, O. H. Larsen, P. N. Laursen, C. Fenger-Eriksen, and C. J. Rea, Thromb. Res. **128**, (2011).

[67] R. De Mets, I. Wang, J. Gallagher, O. Destaing, M. Balland, and A. Delon, in *Proc.*

*SPIE Single Mol. Spectrosc. Superresolution Imaging VII*, edited by J. Enderlein (SPIE - The International Society for Optics and Photonics, California, 2014).

[68] Fibrinogen Conjugates F13192, Invitrogen https://www.thermofisher.com/document (2003).

[69] J. D. Bjorge, A. Jakymiw, and D. J. Fujita, Oncogene **19**, 5620 (2000).

[70] A. Kerjouan, Décodage Des Fonctions Spatio-Temporelles de La Signalisation Src Impliqué Dans La Migration et l'invasion Par Une Approche Optogénétique, Thesis, Universite Grenoble Alpes, 2018.

[71] D. Tischer and O. D. Weiner, Nat. Rev. Mol. Cell Biol. **15**, 551 (2014).

[72] M. A. Digman, P. Sengupta, P. W. Wiseman, C. M. Brown, A. R. Horwitz, and E. Gratton, Biophys. J. **88**, L33 (2005).

[73] C. M. Brown, R. B. Dalal, B. Hebert, M. A. Digman, A. R. Horwitz, and E. Gratton, J. Microsc. **229**, 78 (2008).

[74] L. Valon, Contrôle Optogénétique de La Polarité Cellulaire, Thesis, Insitut Curie Paris, 2014.

[75] P. Mas, P. F. Devlin, S. Panda, and S. A. Kay, Nature **408**, 207 (2000).

[76] H. Alan, Biochem. Soc. Trans. **40**, 1378 (2012).

[77] M. J. Kennedy, R. M. Hughes, L. A. Peteya, J. W. Schwartz, M. D. Ehlers, and C. L. Tucker, Nat. Methods **7**, 973 (2010).

[78] L. Valon, A. Marín-Llauradó, T. Wyatt, G. Charras, and X. Trepat, Nat. Commun. **8**, (2017).

[79] L. Valon, F. Etoc, A. Remorino, F. Di Pietro, X. Morin, M. Dahan, and M. Coppey, Biophys. J. **109**, 1785 (2015).

[80] M. Longfils, N. Smisdom, M. Ameloot, M. Rudemo, V. Lemmens, G. S. Fernández, M. Röding, N. Lorén, J. Hendrix, and A. Särkkä, Biophys. J. **117**, 1900 (2019).

[81] M. Théry, J. Cell Sci. **123**, 4201 (2010).

[82] T. Vignaud, H. Ennomani, and M. Théry, Methods Cell Biol. **120**, 93 (2014).

[83] M. J. Rossow, J. M. Sasaki, M. A. Digman, and E. Gratton, Nat. Protoc. **5**, 1761 (2010).

[84] R. De Mets, A. Delon, M. Balland, O. Destaing, and I. Wang, J. Microsc. 1 (2020).

[85] T. Kühn, T. O. Ihalainen, J. Hyväluoma, N. Dross, S. F. Willman, J. Langowski, M. Vihinen-Ranta, and J. Timonen, PLoS One **6**, (2011).

[86] J. D. Müller, Biophys. J. **86**, 3981 (2004).

# RÉSUMÉ DE THÈSE

## Développements de méthodes de microscopie de fluctuations de fluorescence : application aux mesures de densité de protéines sur substrats et à la caractérisation de processus d'optogénétique

# 1. Introduction

En sciences du vivant, où l'imagerie microscopique est une technique incontournable pour observer et analyser les processus biologiques, obtenir des données quantitatives a toujours été un défi. Un ensemble de techniques possibles pour quantifier les processus biologiques, comme la diffusion et les interactions entre molécules, sont les méthodes de microscopie à fluctuations de fluorescence (**FFM** pour *Fluorescence Fluctuation Microscopy*) qui partagent un point commun : considérer les fluctuations comme une source d'informations, plutôt que du bruit. Les fluctuations de fluorescence, qui peuvent résulter de processus tels que les réactions intra ou intermoléculaires, la diffusion et le transport, permettent d'évaluer le nombre des molécules, la diffusion, la vitesse et la fraction d'interaction des molécules fluorescentes présents dans le volume d'observation du microscope et leur mobilité [4].

Dans cette thèse, nous allons exploiter certains outils d'analyse FFM, en nous focalisant sur deux techniques de corrélation spatiale : la technique de la spectroscopie de corrélation spatiale d'images (**ICS** pour *Image Correlation Spectroscopy*) combinée au photoblanchiment pour déterminer quantitativement la concentration moléculaire sur une surface et la méthode **RICS** (pour *Raster Image Correlation Spectroscopy*) pour mesurer la dynamique moléculaire sur des échantillons biologiques.

# 2. Theory

La technique ICS [5] est réalisée sur un système de molécules immobiles afin de déterminer la densité des molécules en utilisant l'autocorrélation spatiale des fluctuations de l'image. Le signal de fluorescence, $F(x,y)$, ayant une intensité moyenne $\langle F \rangle$, les fluctuations sont données par $\delta F(x,y) = F(x,y) - \langle F \rangle$. Le calcul consiste à corréler les fluctuations d'intensité de chaque pixel d'une image unique avec celles d'un point décalé dans la même image, avec une normalisation :

$$G(\xi,\eta) = \frac{\langle \delta F(x,y)\delta F(x+\xi, y+\eta)\rangle}{\langle F(x,y)\rangle^2} \quad (1)$$

où $\xi$ and $\eta$ sont des variables de décalage dans l'espace-*xy*. Ensuite, la fonction d'autocorrélation spatiale est ajusté avec une Gaussienne [5]

$$G(\xi,\eta) = G(0)\exp\left(-\frac{(\xi^2+\eta^2)}{\omega_0^2}\right) + G_\infty \quad (2)$$

où $G_\infty$ est un décalage introduit pour tenir compte des variations de la ligne de base, et *G*(0) représente l'amplitude de la fonction de corrélation, qui est liée au nombre moyen de particules, *N*, dans le volume d'observation de rayon $\omega_0$, donné par

$$G(0) = \frac{1}{N} \quad (3)$$

A la différence de l'ICS, la technique RICS [49] est bien adaptée à des molécules diffusant rapidement. Les images acquises par balayage laser contiennent des informations spatiales et temporelles qui permettent de mesurer les paramètres de transport. La fonction d'autocorrélation est ajustée en utilisant l'équation (4), dont on extrait la constante de diffusion *D* et le nombre de particules dans le volume d'observation, *N*. L'équation (4) comprend la fonction d'autocorrélation temporelle pour la diffusion $G(\xi,\eta)$ et une fonction liée à la diffusion moléculaire et la position du faisceau laser $S(\xi,\eta)$

$$G_{RICS}(\xi,\eta) = S(\xi,\eta)G(\xi,\eta) + G_\infty \quad (4)$$

$$S(\xi,\eta) = \exp\left[-\frac{\left(\frac{\xi\delta_r}{\omega_0}\right)^2 + \left(\frac{\eta\delta_r}{\omega_0}\right)^2}{\left(1+\frac{4D\left|\tau_p\xi+\tau_l\eta\right|}{\omega_0^2}\right)}\right] \quad (5)$$

où $\delta_r$ est la taille des pixels, plus petite que la taille de la fonction d'étalement du point (ou PSF), $\omega_0$ est la taille du faisceau radial. Pour les mesures de CRY2 dans le cytoplasme, un modèle de diffusion libre 3D est utilisé pour ajuster la partie dynamique de l'autocorrélation et $G(\xi,\eta)$ devient alors

$$G_{3D}(\xi,\eta) = \frac{1}{N}\left(1+\frac{4D\left|\tau_p\xi+\tau_l\eta\right|}{\omega_0^2}\right)^{-1}\left(1+\frac{4D\left|\tau_p\xi+\tau_l\eta\right|}{\omega_z^2}\right)^{-1/2} \quad (6)$$

où $\omega_z$ est la taille du faisceau axiale. Dans le cas de molécules membranaires, l'équation se simplifie en fixant la taille axiale à l'infini, $\omega_0 = \infty$, ce qui revient à supposer que les molécules ne diffusent que sur le plan d'observation. Par conséquent, $G(\xi, \eta)$ est donné par:

$$G_{2D}(\xi, \eta) = \frac{1}{N}\left(1 + \frac{4D\left|\tau_p \xi + \tau_l \eta\right|}{\omega_0^2}\right)^{-1} \quad (7)$$

Une distinction importante entre ces deux techniques réside dans la manière d'exploiter la fonction d'autocorrélation pour obtenir les informations correspondantes. La technique ICS est basée sur l'amplitude de la fonction d'autocorrélation qui est liée à la densité de molécules et/ou à leur état d'agrégation, tandis que le RICS s'appuie sur la forme de la fonction d'autocorrélation, pour en extraire la diffusion.

## 3. Résultats et Discussion

Dans la première partie de notre travail, nous décrivons donc le développement d'une technique quantitative où nous combinons ICS et photoblanchiment (photoblanchiment-ICS, **pICS**) pour améliorer la quantification de la densité de surface des molécules. L'application de l'ICS standard sur des molécules immobilisées sur une surface donne déjà des informations sur leur densité [5], mais peut contenir un biais lorsqu'elle est appliquée à des molécules multi-marquées ou agrégées. Plus précisément, il peut s'agir de biomolécules portant de multiples fluorophores (par exemple, la Fibronectine ayant 1 à 3 fluorophores/ligands, le Fibrinogène qui a environ 15 fluorophores/ligands), une bille contenant de multiples labels, ou des agrégats de molécules ou de billes. Par conséquent, au lieu d'avoir une brillance unique, ces entités ont une distribution de brillance, ce qui contribue aux fluctuations globales d'intensité qui doivent être prises en compte dans l'analyse.

Le photoblanchiment a déjà été proposé comme un moyen de contrôle de l'expérience, dans le cas de marquage Poissonian [55,67] et d'oligomères homogènes [7,56]. Dans le dernier cas, la conclusion des auteurs peut donner l'impression que l'on peut déterminer

directement l'état d'oligomérisation à partir du régime de décroissance du photoblanchiment alors qu'en fait, la seule information qu'on peut extraire en analysant les décroissances de la fluorescence est une combinaison de la moyenne et de la variance de la distribution des oligomères, comme nous le décrivons par la suite.

Nous proposons un formalisme général en faisant intervenir la fluorescence relative, *p*. Ce qui est intéressant dans notre modèle est que qu'il peut être appliquée à des systèmes ayant une distribution arbitraire de fluorophores. Les paramètres pertinents sont le nombre de molécules, *N*, dans le volume d'observation et la brillance moléculaire (le taux de comptage de photons par molécule), *CRM*. Les équations reliant ses quantités à la fluorescence relative sont les suivantes

$$N(p) = N_{tot}\frac{\bar{n}p}{\left(\frac{\overline{n^2}}{\bar{n}} - 1\right)p + 1} \tag{8}$$

$$CRM(p) = \varepsilon\left[\left(\frac{\overline{n^2}}{\bar{n}} - 1\right)p + 1\right] \tag{9}$$

où $N_{tot}$ est le nombre de molécules réel, $\bar{n}$ le nombre moyen initial de fluorophores par entité (moment de premier ordre), et $\overline{n^2}$ est le moment de second ordre de la distribution initiale de fluorophores. Dans l'équation (9), quelle que soit la distribution initiale du fluorophore, la brillance est une fonction affine de la fluorescence relative, *p*, dont l'extrapolation à *p = 0* est égale à la brillance d'un seul fluorophore, $\varepsilon$. À la vue de ces équations, on voit que le photoblanchiment fournit des informations sur la distribution des fluorophores. Ces informations se limitent, sans autres hypothèses, à la brillance des fluorophores uniques $(\varepsilon)$ et aux paramètres statistiques $\overline{n^2}/\bar{n}$ and $N_{tot} \times \bar{n}$.

Pour valider le modèle, nous avons effectué des mesures sur des billes qui présentent une large distribution de brillance. Ce système est intéressant pour tester notre modèle pICS, sachant qu'en parallèle, nous pouvons utiliser une méthode classique de comptage des particules. En appliquant la méthode pICS, nous avons obtenu une valeur cohérente de la brillance des fluorophores uniques $(\varepsilon)$ dans deux situations différentes de concentration

élevée et faible de la solution initiale de billes (Fig. 1). Nous avons également pu calculer la valeur des paramètres statistiques $\overline{n^2}/\bar{n}$ and $N_{tot} \times \bar{n}$. En utilisant le comptage des particules, nous avons pu déterminer le nombre de particules dans le volume confocal volume $N_{tot}$ et le nombre de marqueurs $\bar{n}$, ainsi que le deuxième moment $\overline{n^2}$. Ensuite, nous pouvons calculer la valeur des paramètres statistiques $\overline{n^2}/\bar{n}$ and $N_{tot} \times \bar{n}$ et les comparer avec celles obtenues avec pICS. Cependant, les valeurs obtenues à partir des deux méthodes, bien qu'elles soient proches, ne sont pas identiques. La différence peut être due au fait que dans le cas de l'ICS, nous considérons tous les pixels, tandis que le comptage de particules ne tient pas compte des signaux qui ne sont pas considérés comme des particules. Il est donc possible que le comptage de particules ignore certaines structures lisses qui, au contraire, influencent les résultats que nous avons obtenus avec ICS.

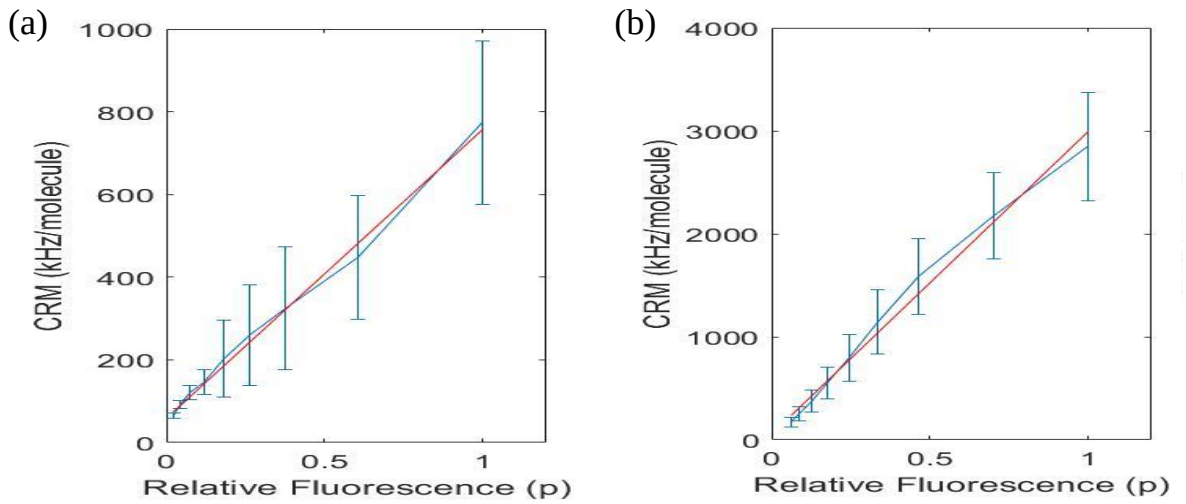


Figure 1 : ***Taux de comptage par molécule en fonction de la fluorescence relative, p, mesurées sur une surface déposée avec des nano-billes fluorescentes.*** *Tracé pour : (a) faible concentrations (calculée à partir de 11 zones) et (b) forte concentrations (calculée à partir de 9 zones) Le taux de comptage par billes diminuent en fonction de la fluorescence relative. Les barres d'erreur sont obtenues à partir de l'erreur standard de la moyenne de toutes les zones pour chaque fluorescence relative.*

En utilisant le modèle proposé, nous avons aussi étudié des ligands portant différents nombres de fluorophores. Nous avons observé, uniquement pour les concentrations de 0.9 and 0.09 µg/mL de fibronectine que le nombre de ligands semble proportionnel à la concentration nominale de la solution déposée sur la surface. Nous avons pu obtenir des

informations supplémentaires sur le nombre initial moyen de rhodamines dans la fibronectine et d'Alexa dans le fibrinogène. Le nombre initial moyen de rhodamines par Fibronectine est $\bar{n} = 1.57$, ce qui raisonnable, compte tenu des spécifications du fabricant ($\bar{n} = 2$). Cependant, le nombre d'Alexa est estimé autour de $\bar{n} = 2.5$, ce qui est très inférieur à la spécification du fabricant de 15 Alexa/Fibrinogène. Cette incohérence, trop forte pour être exclusivement due à la perte de fluorophores par les molécules de fibrinogènes en solution [67] nous a conduit à renoncer à exploiter les estimations du nombre de molécules de fibrinogène.

Dans la deuxième partie du travail, nous appliquons la technique RICS pour étudier la diffusion des protéines dans les cellules. La connaissance de la mobilité des protéines est importante pour comprendre les mécanismes cellulaires. Ici, nous avons utilisé un système optogénétique, CRY2/CIBN, qui intéresse par ailleurs notre équipe du laboratoire. Le CRY2 est une protéine cytoplasmique, tandis que le CIBN est une protéine attachée à la membrane via CAAX. Le système CRY2/CIBN peut être activé lors de l'illumination, de sorte que lorsque CRY2 arrive par diffusion à la membrane il se lie à CIBN. Nous avons choisi la méthode RICS car elle couvre la gamme de diffusion des protéines cytoplasmiques ainsi que des protéines membranaires.

Les cellules constituent un environnement hétérogène où des structures immobiles ou à mouvement lent peuvent dominer la fonction d'autocorrélation, ce qui peut rendre inaccessibles les corrélations dues aux molécules se déplaçant plus rapidement. Nous observons que pour nos mesures, la suppression des structures immobiles par moyennage sur 10 images est un bon compromis. Après cela, une autocorrélation adaptée de l'image entière peut être effectuée et ajustée pour calculer la constante de diffusion de CRY2 et CIBN.

La diffusion que nous avons calculée avec la technique RICS montre des valeurs cohérentes avec celles obtenues à partir d'autres techniques telles que la redistribution de fluorescence après photoblanchiment (FRAP pour *Fluorescence Recovery After*

*Photobleaching*). Cependant le RICS a une meilleure résolution temporelle qui rend cette technique utilisable pour étudier des dynamiques plus rapides comme la diffusion cytoplasmique. En plus, le RICS peut facilement nous permettre de voir la variabilité de la dynamique sur le champ de vision, tandis que FRAP ne donne qu'une seule estimation du paramètre.

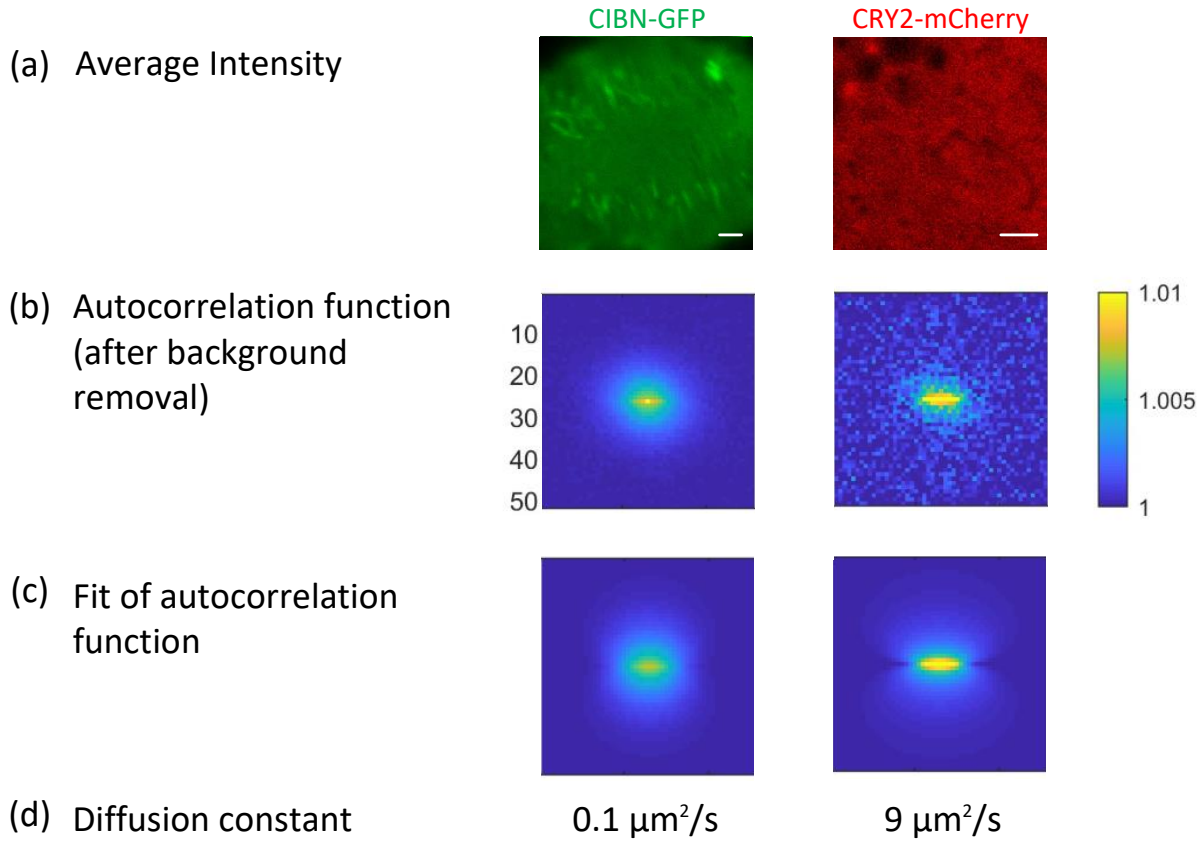


Figure 2: ***Fonction d'autocorrélation et ajustement de la fonction d'autocorrélation avec RICS réalisée sur des protéines dans des cellules optogénétiques.*** *(a) L'intensité moyenne de CIBN et CRY2 dans la région d'intérêt. (b) Fonction d'autocorrélation spatiale après suppression de l'arrière-plan en utilisant une moyenne mobile de dix images. (c) Ajustement de l'autocorrélation après suppression de l'arrière-plan. (d) Constante de diffusion de CIBN et CRY2 à partir de l'ajustement de l'autocorrélation avec RICS sur l'image entière.*

Nous avons également caractérisé le temps caractéristique de dissociation de CRY2 de la membrane cellulaire en analysant les variations temporelles de l'intensité dans différentes régions segmentées de la cellule optogénétique. Le temps caractéristique de dissociation moyen de CRY2 que nous avons mesuré est 208 ± 14 seconds.

## 4. Conclusions

Nous avons exploré et amélioré certaines des techniques de fluctuations de fluorescence, principalement les technique "Spatial Image Correlation Spectroscopy" (ICS) et "Raster Image Correlation Spectroscopy" (RICS), avec quelques applications en biologie. Dans une 1ère partie, nous avons développé un formalisme général de photoblanchiment-ICS (pICS) qui relie le nombre de molécules dans le volume d'observation (et la brillance moléculaire) à la fluorescence relative après photoblanchiment. Ce modèle est a été testé avec succès sur des billes fluorescentes déposées sur une surface ayant une distribution arbitraire de brillance. Dans le cas des ligands portant plusieurs fluorophores, le pICS modèle pourrait être applicable. Dans une 2ème partie, nous avons effectué des mesures sur des cellules optogénétiques (CRY2/CIBN). L'analyse RICS des deux protéines donne la valeur de leurs constantes de diffusion. Nous avons également caractérisé le temps caractéristique de dissociation de cette paire de molécules.